

DISS. ETH NO. 18462

**ADVANCED CREEP DAMAGE AND DEFORMATION ASSESSMENT
OF MATERIALS SUBJECT TO STEADY AND CYCLIC LOADING CONDITIONS
AT HIGH TEMPERATURES**

**A dissertation submitted to
ETH ZURICH**

**for the degree of
Doctor of Sciences**

Presented by

LUCA BINDA

**Dottore in Ingegneria Meccanica, Politecnico di Milano
born November 14, 1980
citizen of Italy**

accepted on the recommendation of

**Prof. Dr. E.Mazza, examiner
Prof. Dr. K.Nikbin, coexaminer
Dr. S.R.Holdsworth, coexaminer**

2010

Sommario

L'obiettivo del presente progetto di ricerca è consolidare una completa caratterizzazione dei meccanismi di danneggiamento dovuti a scorrimento viscoso in materiali di interesse ingegneristico sottoposti a condizioni di carico statico o dinamico e ad alta temperatura e di sviluppare un metodo avanzato di calcolo del danno dovuto a scorrimento viscoso in materiali impiegati dall'ingegneria in ambito impiantistico.

Due acciai di notevole importanza (il bainitico basso legato 1CrMoV dedicato a rotori di turbine a vapore e l'austenitico 316 SS) sono stati studiati al fine di valutarne il comportamento in condizioni di scorrimento viscoso in termini di deformazione e danno. L'indagine scopre in particolare come una eventuale precedente storia di carico ciclico possa influenzare la risposta di questi due acciai in termini di deformazione e danno.

Un modello analitico per il calcolo della duttilità in condizioni di scorrimento viscoso è stato implementato sulla base del modello proposto da M. Spindler e modificato in modo tale da comprendere l'influenza del "material pedigree" (composizione chimica e trattamento termico), così da incrementare l'affidabilità e la precisione del calcolo della duttilità a frattura dell'acciaio 1CrMoV.

La versione modificata del modello di duttilità, grazie alla caratterizzazione dell'influenza del material pedigree, è stata esaminata su una serie di dati provenienti da diversi laboratori di prova e 10 differenti forgiati per un totale di 88 campioni e ha prodotto una varianza inferiore del 54% rispetto al modello di duttilità standard.

Un'interessante ambito di applicazione del modello di duttilità evoluto è rappresentato da una qualitativa caratterizzazione del meccanismo di danneggiamento dovuto a scorrimento viscoso. Viene sottolineata l'importanza di caratterizzare quantitativamente il danno dovuto a scorrimento viscoso e interpretare l'eventuale relazione esistente tra la duttilità a frattura prevista in seguito a scorrimento viscoso e il meccanismo di danneggiamento.

Prove di fatica a basso numero di cicli sono state effettuate sugli stessi acciai al fine di caratterizzarne il comportamento ciclico e soprattutto l'influenza di una deformazione ciclica ad alta temperatura sul successivo comportamento viscoso.

Il bainitico 1CrMoV e l'austenitico 316 SS rispondono rispettivamente con addolcimento e incrudimento ciclico e questa sostanziale differenza si riflette anche sulle successive prove di valutazione di proprietà viscosi.

L'1CrMoV, in seguito a deformazione ciclica, mostra maggiori velocità di deformazione e ridotti tempi di frattura. Tali proprietà variano proporzionalmente nel rispetto della relazione di Monkman-Grant valida per lo stesso acciaio non sottoposto a deformazione ciclica. Tale elemento di novità rende la relazione di Monkman-Grant uno strumento importante per la determinazione della vita del materiale anche in seguito a deformazione ciclica.

La riduzione di resistenza allo scorrimento viscoso è accompagnata dall'incremento di duttilità a rottura, la quale si ripresenta concorde con il modello di duttilità definito per l'1CrMoV non deformato ciclicamente.

La presente dissertazione offre un confronto tra l'approccio basato su "time fraction" e quello basato su "ductility exhaustion" attraverso l'utilizzo di diagrammi per la combinazione del

danno dovuto a fatica e scorrimento viscoso. In particolare viene sottolineata l'importanza di considerare l'influenza di i) una precedente deformazione viscosa sulla successiva resistenza al danneggiamento per fatica e ii) una precedente deformazione ciclica sulla successiva resistenza (secondo "time fraction") e duttilità (secondo "ductility exhaustion") a scorrimento viscoso. Infine viene evidenziata l'importanza di considerare incrementi negativi di deformazione viscosa nel calcolo della frazione di danno nell'eventuale approccio secondo "ductility exhaustion".

L'acciaio austenitico 316 SS sottoposto a deformazione ciclica mostra maggiore resistenza a scorrimento viscoso, come atteso in virtù dell'incrudimento ciclico accumulato. Di nuovo la relazione di Monkman-Grant rappresentativa della resistenza a scorrimento e tempo di frattura dell'acciaio 316 SS rimane valida anche per l'acciaio 316 SS sottoposto a deformazione ciclica ad alta temperatura.

Differentemente dall'acciaio 1CrMoV, i risultati sperimentali indicano che la duttilità a rottura dell'acciaio austenitico 316 SS aumenta. Tali risultati evidenziano l'importanza di indagare ulteriormente l'influenza della deformazione ciclica in quanto responsabile di notevoli aumenti di performance meccaniche, in termini di resistenza a scorrimento viscoso e duttilità.

Abstract

The aim of the project is to establish a fundamental understanding of the mechanics and mechanisms of creep damage development in steady and cyclic loading situations at high temperatures and to develop an advanced methodology for the more effective assessment of creep damage in various engineering materials.

Two steels of fundamental engineering importance, namely the 1CrMoV low alloy bainitic steam turbine rotor steel and the Type 316 stainless steel, were investigated in order to assess their creep properties in terms of deformation and damage. The investigation specifically addressed how prior cyclic deformation influences the creep deformation and damage response of these two steels.

A creep rupture ductility model was implemented on the basis of the stress-modified ductility exhaustion (SMDE) approach modified to include the effect of material pedigree (chemical composition and heat treatment process) in order to more accurately predict the deformation at rupture of the 1CrMoV steel.

The material pedigree enhanced stress-modified ductility exhaustion model improves the accuracy of rupture ductility predictions by reducing the variance by 54% with respect to the standard SMDE model.

Standard low cycle fatigue testing has been performed also on the same two steels with the aim of characterising their cyclic deformation response and mostly to assess the influence of high temperature prior cyclic deformation on subsequent creep properties.

The contrasting softening and hardening responses to cyclic deformation exhibited by the 1CrMoV steel and the Type 316 stainless steel respectively lead to opposite influences on creep properties.

The prior cyclic deformed 1CrMoV steel shows higher creep strain rates and lower rupture times in a way which is respectful of the Monkman-Grant relationship applying for the as-received 1CrMoV steel. This makes the Monkman-Grant relationship an even more important tool for life assessment when prior loading is present.

Reduced creep strengths are accompanied by enhanced creep rupture ductilities, which still obey the ductility model defined for the as-received 1CrMoV.

A detailed comparison between the time fraction approach and the ductility exhaustion approach is offered and represented through the aid of creep-fatigue damage summation diagrams. In particular the importance is highlighted of accounting for the reciprocal influences of *i*) prior creep deformation on fatigue crack initiation resistance and *ii*) prior cyclic deformation on subsequent creep strength (for the time fraction rule) and ductility (ductility exhaustion). Furthermore, the importance of accounting for negative increments of creep strain when calculating the creep damage fraction on a ductility exhaustion base is also highlighted.

The prior cyclic deformed Type 316 stainless steel shows enhanced creep strength, in accordance with the cyclic hardening accumulated during prior cyclic deformation. There again the Monkman-Grant relationship representative of as-received Type 316 stainless steel still remains valid for the prior cyclic deformed material.

In contrast to the 1CrMoV steel, experimental results indicate that the creep rupture ductility of the Type 316 stainless steel increases with increase of creep strength. Such results emphasize the importance of investigating the effect of prior cyclic deformation since it may lead cyclic hardening materials to enhance both their creep strength and their creep ductility.

TABLE OF CONTENTS

LIST OF SYMBOLS	11
1 INTRODUCTION	13
2 CREEP-FATIGUE STATE-OF-THE-ART ASSESSMENT	17
2.1 Creep	17
2.1.1 Creep deformation	17
2.1.1.1 Deformation mechanism maps	20
2.1.2 Creep damage	22
2.1.2.1 Time fraction rule	23
2.1.2.2 Ductility exhaustion rule:	23
2.1.2.3 Damage mechanism maps	25
2.1.3 Creep Ductility	29
2.2 Fatigue	31
2.2.1 Fatigue deformation	31
2.2.2 Fatigue damage	32
2.2.2.1 Fatigue damage mechanisms	33
2.3 Creep-fatigue damage characterisation	34
3 CREEP	36
3.1 Creep tests on 1CrMoV	36
3.1.1 Post Test Inspections	37
3.1.1.1 Hardness	37
3.1.1.2 Grain size	37
3.1.1.3 Creep damage	38
3.1.2 Creep rupture properties	40
3.1.2.1 Creep strain	40
3.1.2.2 The Monkman-Grant temperature independency	41
3.1.2.3 Creep ductility	44
3.2 The Exhaustion of Creep Ductility in 1CrMoV Steel	47
3.2.1 Introduction	47
3.2.2 Creep Rupture Ductility Model	47
3.2.3 Material Pedigree Functions	50
3.2.3.1 Chemical Composition	51
3.2.3.2 Heat Treatment	56
3.2.4 Model Effectiveness	57
3.2.5 Discussion	60

3.2.6	The Creep Ductility model and the creep damage mechanisms	60
3.3	Type 316 Stainless Steel	64
3.3.1	Creep deformation	64
3.4	Concluding Remarks	66
4	CYCLIC DEFORMATION	67
4.1	Fatigue Tests on 1CrMoV	67
4.2	Post Test Inspection of cyclic deformed 1CrMoV	69
4.2.1	Hardness	69
4.2.2	Grain size measurements	70
4.2.3	Dislocation density	71
4.2.4	The Microstructure of 1CrMoV	71
4.2.4.1	Dislocation annihilation and rearrangement	72
4.2.4.2	Sub-grain (or sub-cell) structure formation	74
4.3	Miner's rule: verification of effectiveness	75
4.4	Type 316 Stainless Steel	79
4.4.1	PTI	80
4.4.1.1	Hardness	80
4.4.1.2	Grain size measurements	81
4.5	Concluding Remarks	82
5	CREEP-FATIGUE DAMAGE CHARACTERISATION	83
5.1	TMF tests on 1CrMoV	83
5.1.1	Test results	84
5.1.2	Post Test Inspection	85
5.2	Finite Element analyses	86
5.2.1	Time fraction rule based damage assessment	88
5.2.2	Ductility exhaustion rule based damage assessment	89
5.3	Need for further research	90
5.4	Influence of prior creep deformation on fatigue endurance	90
5.5	Influence of prior cyclic deformation on creep properties	92
5.5.1	Creep tests of PCD 1CrMoV	92
5.5.2	Post Test Inspection	93
5.5.2.1	Vickers Hardness measurements	93
5.5.2.2	Grain size measurements	94
5.5.2.3	Creep damage mechanisms modification	94

5.5.3	Influence of PCD on creep strength	96
5.5.3.1	The Monkman-Grant PCD independency	99
5.5.3.2	Time fraction approach	100
5.5.4	Influence of PCD on creep ductility	101
5.5.4.1	Ductility exhaustion approach	103
5.5.4.2	Effective accumulation of creep strain in compression	104
5.6	Evolutionary creep-fatigue damage assessment	105
5.7	Discussion	106
5.8	Type 316 Stainless Steel	107
5.8.1	Creep tests of PCD material	107
5.8.2	Post Test Inspections	108
5.8.2.1	Vickers Hardness measurements	108
5.8.2.2	Grain size measurements	108
5.8.3	Influence of PCD on creep strength	109
5.8.3.1	The Monkman-Grant PCD independency	110
5.8.4	Influence of PCD on creep ductility	111
5.8.5	Creep-fatigue damage characterisation	112
5.9	Concluding Remarks	112
6	CONCLUSIONS	113
7	REFERENCES	116
8	ACKNOWLEDGMENTS	119
I.	APPENDIX : 1CRMV ROTOR STEEL	120
a.	Material pedigree	123
i.	Hardness	123
ii.	Grain size	123
b.	Mechanical properties	124
i.	Tensile properties	124
ii.	LCF properties	124
iii.	Creep properties	125
II.	APPENDIX : TYPE 316 STAINLESS STEEL	126
a.	Material pedigree	126
i.	Hardness	126
ii.	Grain size	126

b.	Mechanical properties	127
i.	Tensile properties	127
ii.	Fatigue properties	128
iii.	Creep properties	129

LIST OF SYMBOLS

A_{cl}	Austenite transformation starting temperature
A_u	Elongation at rupture
CSA	Constant strain amplitude
D_C	Creep damage fraction
D_F	Fatigue damage fraction
$f(mp)$	Individual parameter material pedigree function
$f(MP)$	Overall material pedigree function
HCF	High cycle fatigue
HT	High thermal transient
IT	Intermediate thermal transient
LCF	Low cycle fatigue
LT	Low thermal transient
m	Strain rate exponent
MG	Monkman-Grant
n	Stress exponent
N	Number of cycles
N_i	Number of cycles to fatigue crack initiation (coinciding with the beginning of load drop/deviation from stable stress-cycle response)
N_i^d	Number of cycles to fatigue crack initiation in creep deformed material
$N_{2\%}$	Number of cycles to fatigue crack initiation (coinciding with the 2% load drop/deviation from stable stress-cycle response)
N_{PH}	Number of cycles at peak hardening
PCD	Prior cyclic deformation
P_{HJ}	Holloman Jaffe parameter
P_{MG}	Monkman-Grant parameter
PTI	Post test inspection
Q	Activation energy for diffusion creep
R	Gas constant
$SMDE$	Stress modified ductility exhaustion
t_h	Hold Time
t_u	Time to creep rupture
t_u^s	Time to creep rupture in cyclic-softened material
T	Temperature

T_m	Melting temperature
TMF	Thermo-mechanical fatigue
VSA	Variable strain amplitude
Z_u	Area reduction at rupture
$Z_{u,L}$	Lower shelf area reduction at rupture
$Z_{u,U}$	Upper shelf area reduction at rupture
$\Delta\varepsilon$	Strain range
ε	Strain
$\dot{\varepsilon}$	Creep strain rate
ε_a	Strain amplitude
$\dot{\varepsilon}_c$	Instantaneous creep strain rate
ε_f	Local fracture strain
$\dot{\varepsilon}_{min}$	Minimum creep strain rate
σ	Stress
σ_{ig}	Highest Stress responsible for 100% intergranular rupture
σ_{tg}	Lowest Stress responsible for 100% transgranular rupture
$\sigma_{N=N_{PH}}$	Tensile peak stress at peak hardening
$\sigma_{N=1}$	Tensile peak stress at first cycle
$<$	Cyclic deformation with increasing ε_a in block cycling test
$>$	Cyclic deformation with decreasing ε_a in block cycling test

1 INTRODUCTION

Materials employed in power plants or in the aerospace industry are subjected to static or cyclic loading at high temperature which can lead to the formation of damage. The type of damage occurring in power plants materials is generally generated by a combination of creep and fatigue loading, but other sources of damage may often occur.

The art of characterizing and predicting the material damage is of fundamental importance for different reasons (economy, environment and reliability are common issues for which industries are further enhancing their targets) and is in this dissertation referred to as design or remaining life assessment or, since creep and fatigue are the damage mechanisms of most interest in the following dissertation, as creep-fatigue damage assessment.

Many of the classical models representative of the creep and rupture behaviour of metals were developed prior to and during the 1950s and 1960s (see [29] for more details concerning the creep research historical developments). Nevertheless their subsequent exploitation, in particular for the assessment of large creep property datasets, was initially limited by the capability of the analytical tools available at the time. An apparent decline in activity followed during the 1970s and 1980s, during which a more intense research took place for creep properties optimization by control of the heat treatment and the chemical composition.

A true resurgence during the last two decades characterizes the creep behaviour representative models, driven by the need of improving reliability, economical and environmental efficiency of engineering systems (e.g. aerospace or power plants). Such economical and environmental thrust and the continuous improvement of finite element analysis software packages has also led to the development of creep and fatigue damage assessment procedures to be used for design and remaining life assessment.

As a generality, the current design and remaining life assessment procedures for fatigue and creep damage calculation neglect the importance of the material heat treatment condition and chemical composition (i.e.: the material pedigree).

The current design and remaining life assessment procedures for static and cyclic loading conditions at high temperature (thermal-mechanical fatigue - TMF) do not systematically consider the influence of the material microstructure, which evolves as a consequence of the applied loads, affecting the mechanical response (indeed these procedures attempt to acknowledge the influence of a material pedigree variability by adopting conservative lower bound properties as reference values).

Ultimately, such procedures do offer an interpretation which is comprehensive of creep-fatigue damage reciprocal interactions, but only a-posteriori, on the basis of observed thermo-mechanical fatigue lifetimes. This leads in fact to non linear creep fatigue damage summation diagrams, with locus representative of usually negative creep-fatigue damage interactions.

The research activity discussed in this dissertation moves its steps starting from the above mentioned structural analyses of the design and remaining life assessment procedures and is carried on by the need to close the observed weaknesses and enhance the accuracy and reliability of assessment procedures by focussing on more systematic and comprehensive concepts.

In accordance with industrial needs, the accuracy of engineering structures design or remaining life assessment must be hence ideally maximized. This requires to develop a good sound knowledge of all features characterizing the damage assessment procedures and to concentrate efforts for improvement of those which are likely to mostly affect reliability and accuracy of assessment.

So it was done for this research activity, which identified i) the eventual material pedigree (chemical composition and heat treatment procedure) as an important independent variable for predicting creep rupture properties and ductility in particular and ii) the influences of eventual prior loading (prior creep deformation or prior cyclic deformation) on the mechanical properties (creep strength and ductility and low cycle fatigue endurance) of engineering materials.

This research project has attempted to improve the creep rupture ductility assessment techniques in order to give further emphasis to the creep life predictions based on the ductility exhaustion rule and to develop a fundamental understanding with respect to those concepts (i.e. the creep fatigue reciprocal influences) which are considered to play a major role in damage assessment.

Improvements can be indeed achieved by understanding and analytically implementing what the real occurring mechanisms are: in particular the influence of the material microstructure on the response to static or cyclic loading conditions, but also the influence of the loading conditions on the microstructure itself needs to be investigated. The material microstructure characterization is hence considered as an integral part of damage assessment procedures and the discussions in this Dissertation rely in many parts on post test inspection activities, like optical microscopy and transmission electron microscopy, performed to obtain a complete scenario for the more effective design of damage assessment procedures.

It became logical in this Dissertation to structure the discussion in a way which introduces first the most accepted concepts and methods for creep and fatigue damage assessment and then to move to the performed research activity: this consists of the characterization of physical and mechanical responses of materials subject to creep.

The research is mainly based on experimental activity but is also supported by an extensive literature review. This is particularly true with respect to the third chapter (Creep), where a creep rupture ductility model is presented as a result of the development of the stress modified ductility exhaustion concept, on the basis of evidence found in the literature concerning the influence of the material pedigree on the creep rupture properties.

The fourth chapter (Cyclic deformation) aims to characterize the physical and mechanical response of materials subject to cyclic deformation at high temperatures. Being the materials' response to cyclic deformation an author's fundamental input to investigate the materials' creep-fatigue damage interaction, the analysis of this chapter involves literature review, experimental tests and post test inspection activities which were comprehensive of transmission electron microscopy.

The fifth chapter (Creep-fatigue damage characterization) is then arranged in a way to complete the discussion of the previous chapters 3 and 4. It shows the way to implement the new concepts in a creep-fatigue damage assessment procedure and compares its results with those of physical observations from post test inspection of testpieces subject to thermo-mechanical fatigue cycles as well as, of course, to results of standard creep-fatigue damage assessment procedures.

The basis for this research activity is the consideration of the low alloy bainitic 1CrMoV steam turbine rotor steel and the austenitic Type 316 stainless steel. These materials were chosen because they best represent two opposite mechanical responses to cyclic plastic deformation, and so they were the best choice to characterize the influence of prior loading on subsequent creep properties, as described in chapter 5.

The results obtained by implementing the standard design and remaining life assessment procedures with the new concepts investigated throughout this research activity are encouraging. The creep rupture ductility model presented in chapter 3 is able to reduce the variance by 54% with respect to the standard stress-modified ductility exhaustion approach when tested on a large creep database of 1CrMoV steam turbine rotor steels. Such an improvement justifies then the effort made to build up the creep rupture ductility model for the investigated material.

The creep-fatigue damage assessment procedure presented in chapter 5, comprehensive of the accounting for creep-fatigue reciprocal influences and for the accumulation of creep strain during compression stress states, leads to creep-fatigue damage fractions more consistent with the results of post test inspections. Furthermore, the adopted research approach has highlighted what the real effect of prior loading is on subsequent fatigue endurance and creep properties: the fatigue endurance may be in fact enhanced after prior creep deformation of cyclic softening materials like the 1CrMoV steel. Prior cyclic deformation of cyclic softening materials may lead to reduced creep strength (lower rupture times) and higher creep rupture ductilities.

Prior cyclic deformation has also an interesting effect on the creep properties of cyclic hardening materials like the austenitic Type 316 stainless steel, because it leads to enhanced creep strength (due to accumulated cyclic hardening) but also to higher creep rupture ductility, which makes the cyclic deformation a potential technique to modify the creep properties of cyclic hardening materials in a way which is more attractive for engineering purposes.

But these major achievements are not the only two which emphasize the importance of this research activity: outstanding results were obtained and are presented to set the basis for an extensive use of the Monkman-Grant relationship as a remaining life assessment tool. Experimental results and data in the literature have proven that the Monkman-Grant relationship representative of the creep properties of the 1CrMoV steel is independent of prior cyclic deformation between 450°C and 650°C and that representative of the Austenitic Type 316 stainless steel is independent of prior cyclic deformation at 550°C.

Finally, this Dissertation is a presentation of results of scientific research which has a potential impact on common and fundamental industrial procedures for the design and remaining life assessment of materials subject to steady or cyclic loading conditions at high temperature.

The choice of testing the 1CrMoV and the Austenitic Type 316 Stainless steels for their opposite responses to high temperature loading conditions was due to the intention to explore the widest possible range of situations. The focus on the impact of the materials' microstructure and the creep-fatigue damage reciprocal influences were on the other hand due to the perception about their prominent importance for the cause of establishing more reliable design and remaining life assessment procedures, as well as for the novelty of the content of such research.

It goes however without saying that the results shown here represent only part of a necessary extensive research process aimed to develop a very complete knowledge of deformation and damage mechanisms occurring in engineering materials subject to static and cyclic loading conditions at high temperature.

2 CREEP-FATIGUE STATE-OF-THE-ART ASSESSMENT

This chapter introduces the main concepts which form the basis for the following dissertation.

2.1 Creep

2.1.1 Creep deformation

Creep deformation occurs in three main stages:

- primary creep, during which the strain rate decreases due to strain hardening,
- secondary creep, spent at constant strain rate and which may last for a considerable portion of lifetime,
- tertiary creep, where the creep strain rate increases exponentially as the material microstructure recovers and softens, enabling the creep deformation to be mostly accumulated during this stage. This regime may occupy a considerable fraction of the overall lifetime.

A classical creep curve representation is shown in Fig.2.1.

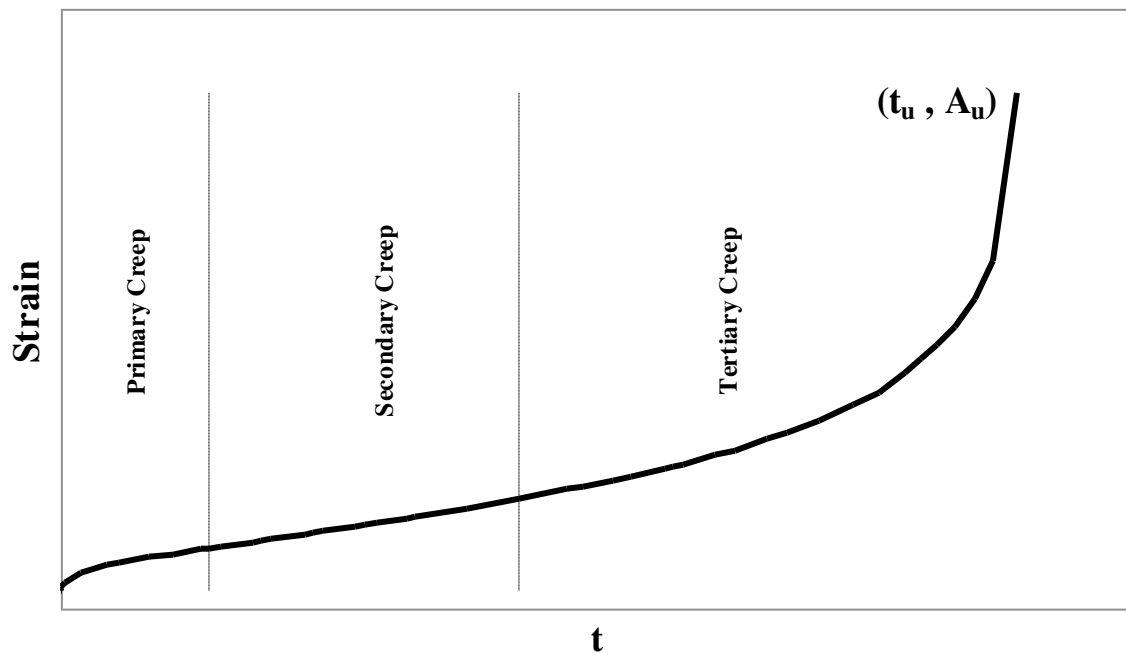


Fig.2.1: Accumulated creep deformation at constant stress and temperature, until rupture occurs after t_u

The instantaneous creep strain rate varies according to the different creep stages as reported in Fig.2.2.

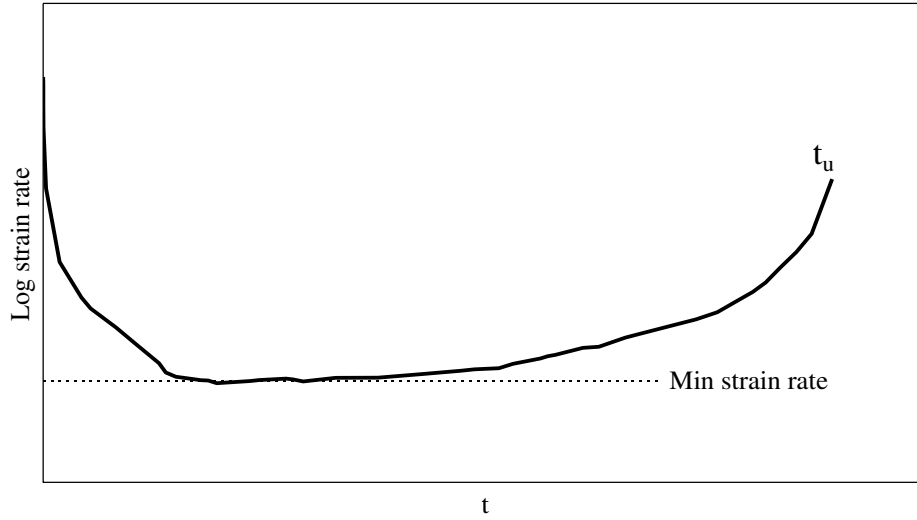


Fig.2.2: Instantaneous creep strain rate during lifetime, under constant stress and temperature

The Norton law is widely used to describe the stress dependency of the minimum creep strain rate:

eqn.2.1

$$\frac{d\varepsilon}{dt} = A \cdot \sigma^n$$

The Norton law, modified by the Arrhenius term for thermally activated processes, may be generally expressed as follows:

eqn.2.2

$$\dot{\varepsilon} = A \cdot e^{\left(\frac{K \cdot Q}{R \cdot T}\right)} \cdot \sigma^n$$

in order to predict creep strain rates on the basis of stress, temperature and a series of material dependent constants. Q is the activation energy for the activated creep mechanism and R is the gas constant, whereas A, K, n are material pedigree dependent constants.

During the course of the project, TMF numerical analyses were performed on the basis of a constitutive model, representative of the material behaviour, which was characterized by a non-unified model approach. The creep deformation was determined by a time dependent plastic strain calculated on the basis of the Norton-Bailey creep law corrected with a temperature dependent factor and applied with the strain hardening rule. For such applications the creep deformation equation was expressed according to Colombo (See [17] and [18]) as

$$\varepsilon_{cr} = \beta \cdot e^{\left(\frac{q_1}{T}\right)} \cdot A \cdot \sigma^n \cdot t^m$$

where β and q_1 are material constants and A , n and m were determined from the best fitting of the 1CrMoV relaxation curves taken from the first cycle of an isothermal 550°C LCF test including 16 hours hold time. A strain hardening law and a primary creep persistency law were also involved. A factor 0.8 was applied to the stress term in the creep law to simulate the observed cyclic softening behaviour on the attainment of stabilised cyclic conditions.

2.1.1.1 Deformation mechanism maps

Creep is a time dependent deformation process occurring at temperature higher than $0.4 \cdot T_m$ eventually leading to failure.

Fig.2.3 shows the deformation mechanism map for pure Iron.

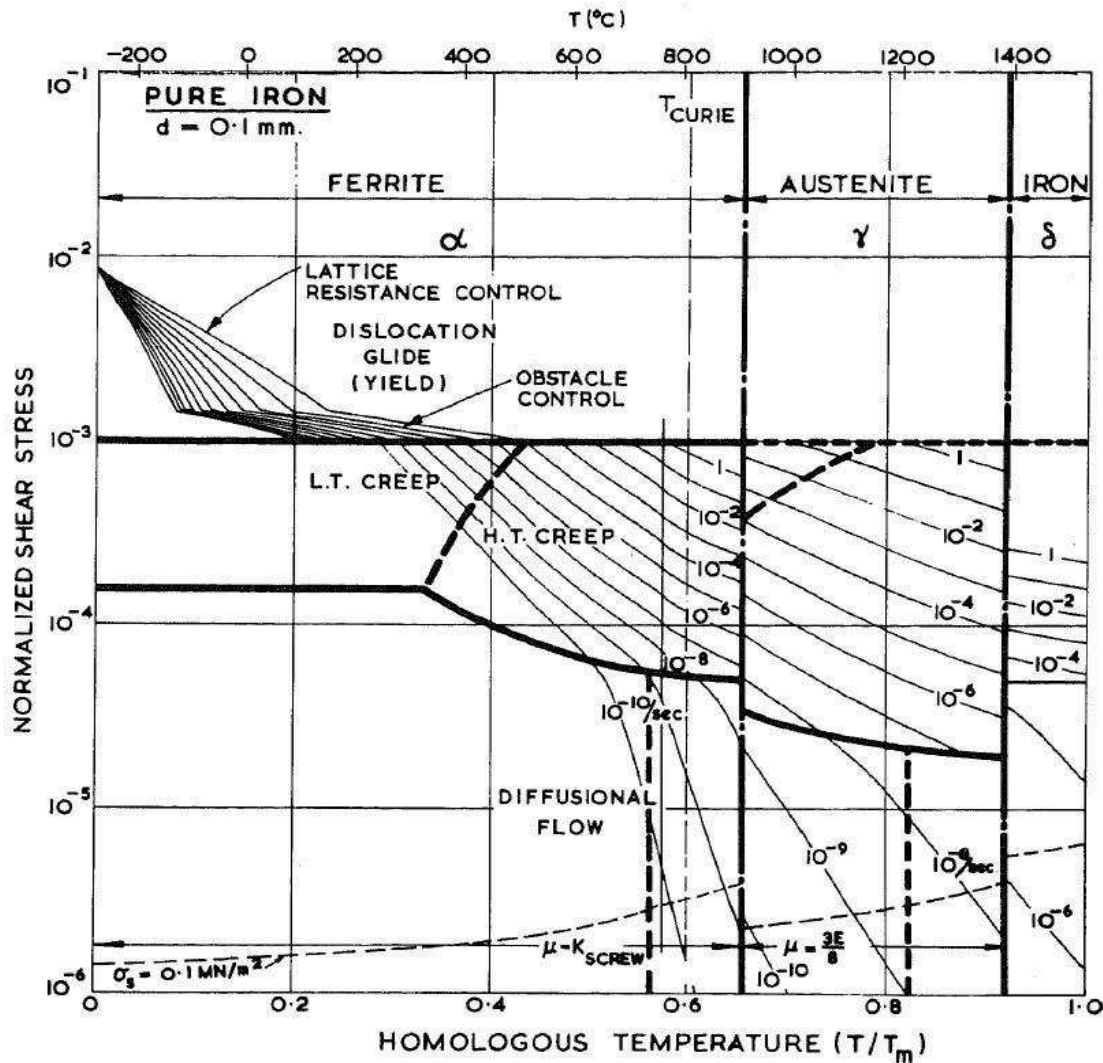


Fig.2.3: Deformation mechanism map for pure iron, [23]

The strain rate discontinuity is present at every phase change (i.e. from α -ferrite to γ -austenite to δ -iron), because all the physical properties (lattice parameters, burgers vectors and diffusion coefficients) change. Within the ferrite regime, the creep deformation mechanism is different at different stress levels. In particular:

- At high stresses, deformation occurs through dislocations glide on crystal planes and the strain rate is controlled by the lattice resistance.

- At intermediate stresses, deformation occurs by dislocation climb and lattice diffusion (Nabarro-Herring creep).
- At low stresses, creep occurs by deformation along grain boundary through diffusion of vacancies and atom (Coble creep).

It is important to observe that the activation energy (Q , see eqn.2.2) changes for different creep mechanism: in particular $Q_{\text{dislocation glide}} > Q_{\text{lattice diffusion}} > Q_{\text{grain boundary diffusion}}$, that is the reason for which, given the same applied stress, Coble creep tends to occur at lower temperatures than Nabarro-Herring creep.

The low alloy ferritic steel 1CrMoV derives its strength and creep resistance from a fine dispersion of carbide particles, obtained after a heat treatment designed to give a fine grain tempered bainite. The deformation mechanism map in Fig.2.4 emphasizes the high flow stress and creep resistance of the dispersion-strengthened ferrite for a 100 μm grain size 1CrMoV (above 760°C, A_{c1} , austenite phase starts to form).

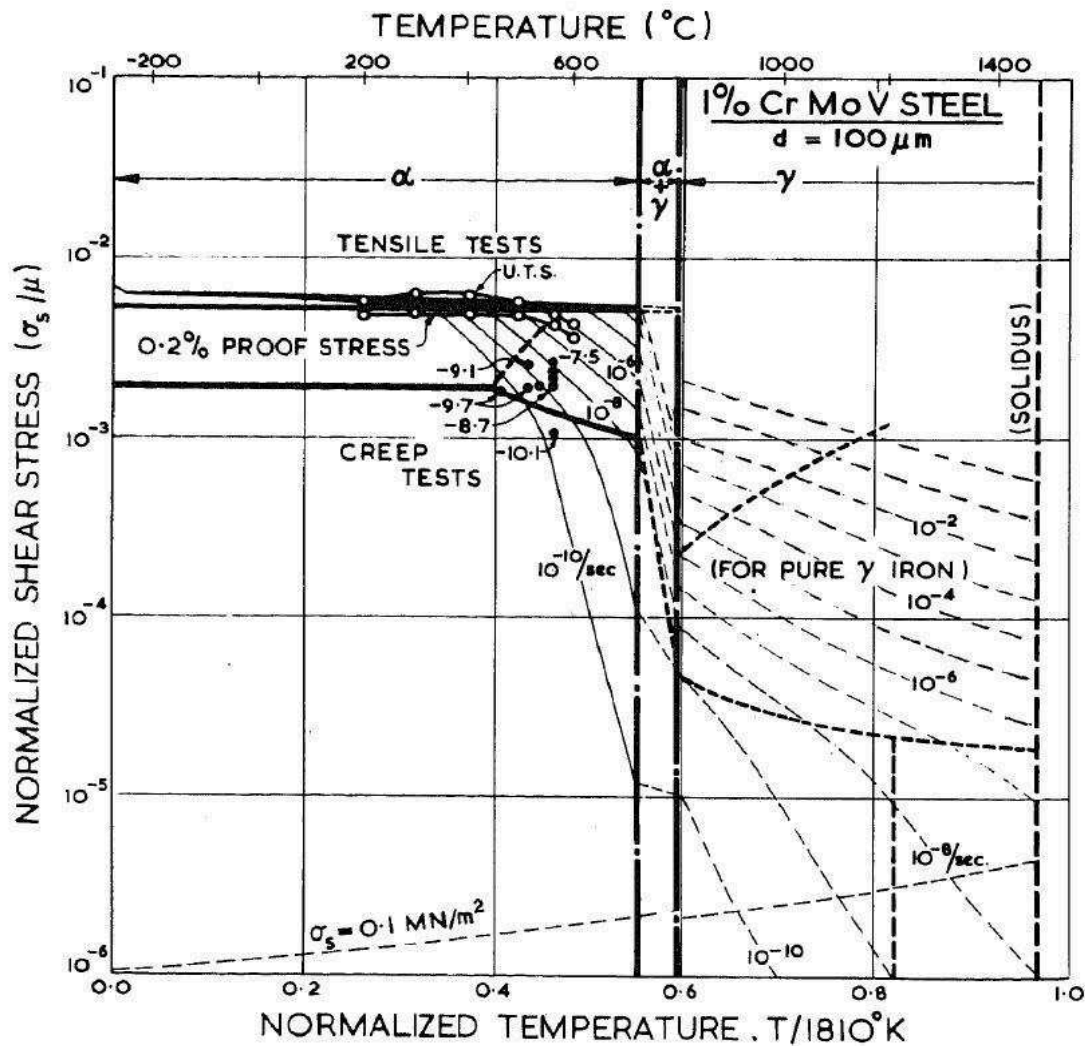


Fig.2.4: Deformation mechanism map for 1CrMoV, [23]

Fig.2.5 shows the deformation mechanism map for a 200 μm grain size austenitic stainless steel (316SS).

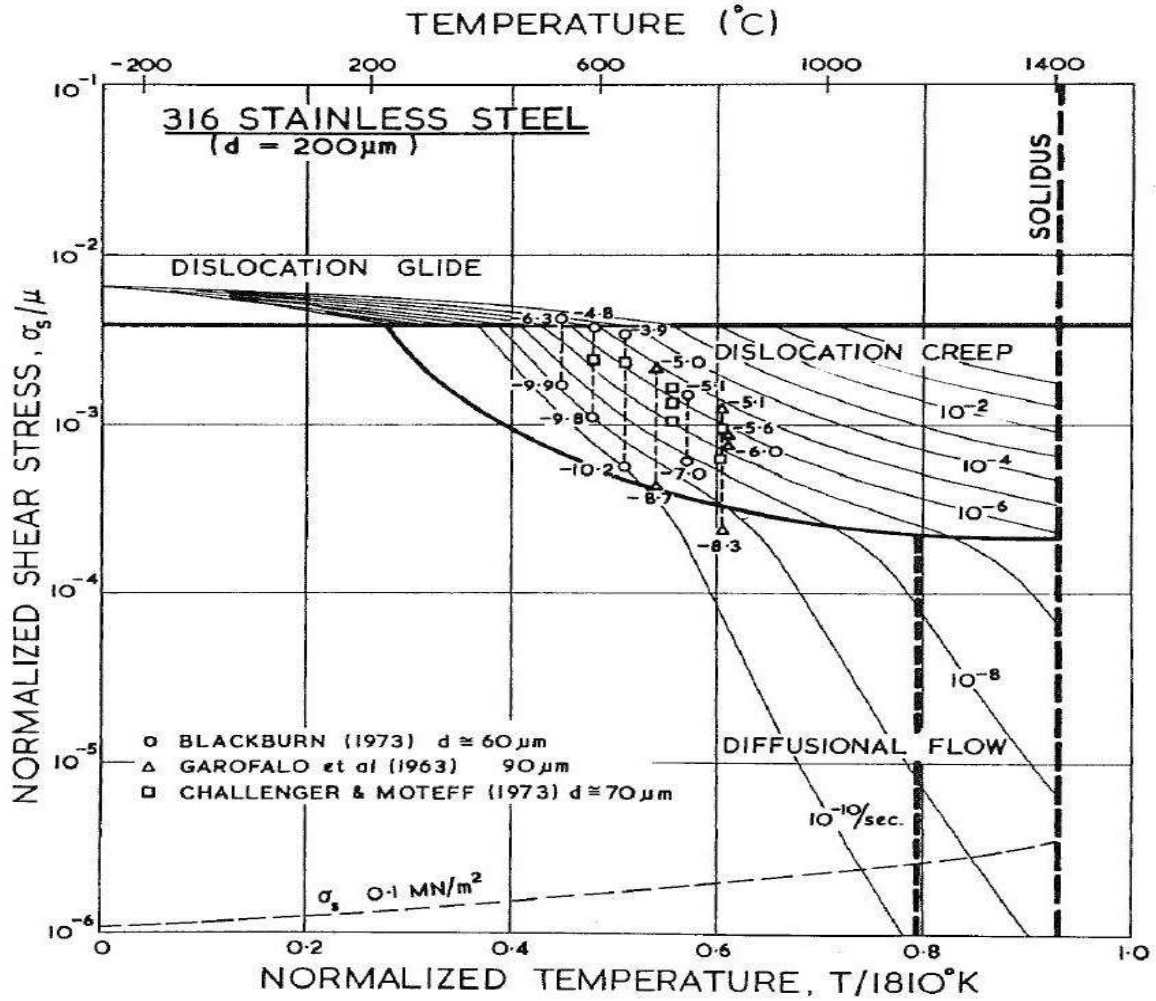


Fig.2.5: Deformation mechanism map for SS316, [23]

2.1.2 Creep damage

The Orr-Sherby-Dorn model equation [46] predicts creep rupture times on the basis of stress, temperature and a series of material dependent constants. It can be generally expressed as follows:

eqn.2.4

$$t_u = B \cdot e^{\left(\frac{I-Q}{RT}\right)} \cdot \sigma^w$$

In eqn.2.4 (like in eqn.2.2), Q is the activation energy for the activated creep mechanism and R is the gas constant, whereas B , I , W are material pedigree dependent constants.

The Monkman-Grant (MG) equation relates the creep rupture time to the minimum creep strain rate and, as it will be shown in the following chapters, can be used to predict long term creep lives. The relation is linear on a bi-logarithmic base.

eqn.2.5

$$\dot{\epsilon}_{\min} = P_{MG} \cdot t_u^{-1}$$

Paragraphs 3.1.2.2 and 5.5.3.1 will show some experimental results concerning the MG equation which suggest some new application scope for creep life assessment involving this model.

2.1.2.1 Time fraction rule

The most widely adopted method of representing creep damage fraction due to primary - directly applied - loading conditions is in terms of time, such that the damage is given by the sum of hold times (t_h) normalized to their respective rupture time,

eqn.2.6

$$D_C = \sum N \cdot \int_0^{t_h} dt / t_u(T, \sigma_t)$$

where σ_t is the stress acting during the time increment, dt , at temperature, T , and $t_u(T, \sigma_t)$ is the rupture time associated with this level of temperature and stress.

2.1.2.2 Ductility exhaustion rule:

As an alternative to the time fraction rule, the ductility exhaustion rule was proposed in 1966 by Edmunds and White [20] and is being increasingly adopted as the basis for quantifying the creep damage fraction accumulated under secondary -self equilibrating- loading conditions [51],

eqn.2.7

$$D_C = \sum N \cdot \int_0^{t_h} \frac{\dot{\epsilon}_c}{\epsilon_f(\epsilon_c)} dt$$

where $\dot{\varepsilon}_c$ is the instantaneous equivalent creep strain rate during the time increment and $\varepsilon_f(\dot{\varepsilon}_c)$ is the creep rupture ductility as a function of the instantaneous equivalent creep strain rate, as proposed by [51]. As a generality, since cavity growth occurs in the presence of local tensile stress states, creep strain is only accumulated during such conditions.

A stress-modified ductility exhaustion model was proposed by Spindler [59], according to which the creep rupture ductility should be expressed as a function of creep strain rate, stress and temperature, i.e.:

eqn.2.8

$$\varepsilon_f = \min \left[A_1 \exp \left(\frac{\Delta G_{AC}}{RT} \right) \cdot \dot{\varepsilon}_c^{n_1} \cdot \sigma_I^{-m_1}, \varepsilon_U \right]$$

2.1.2.3 Damage mechanism maps

Creep fracture may be intergranular, transgranular or a combination of these, depending on creep testing conditions (σ , T) as it is shown in Fig.2.6.

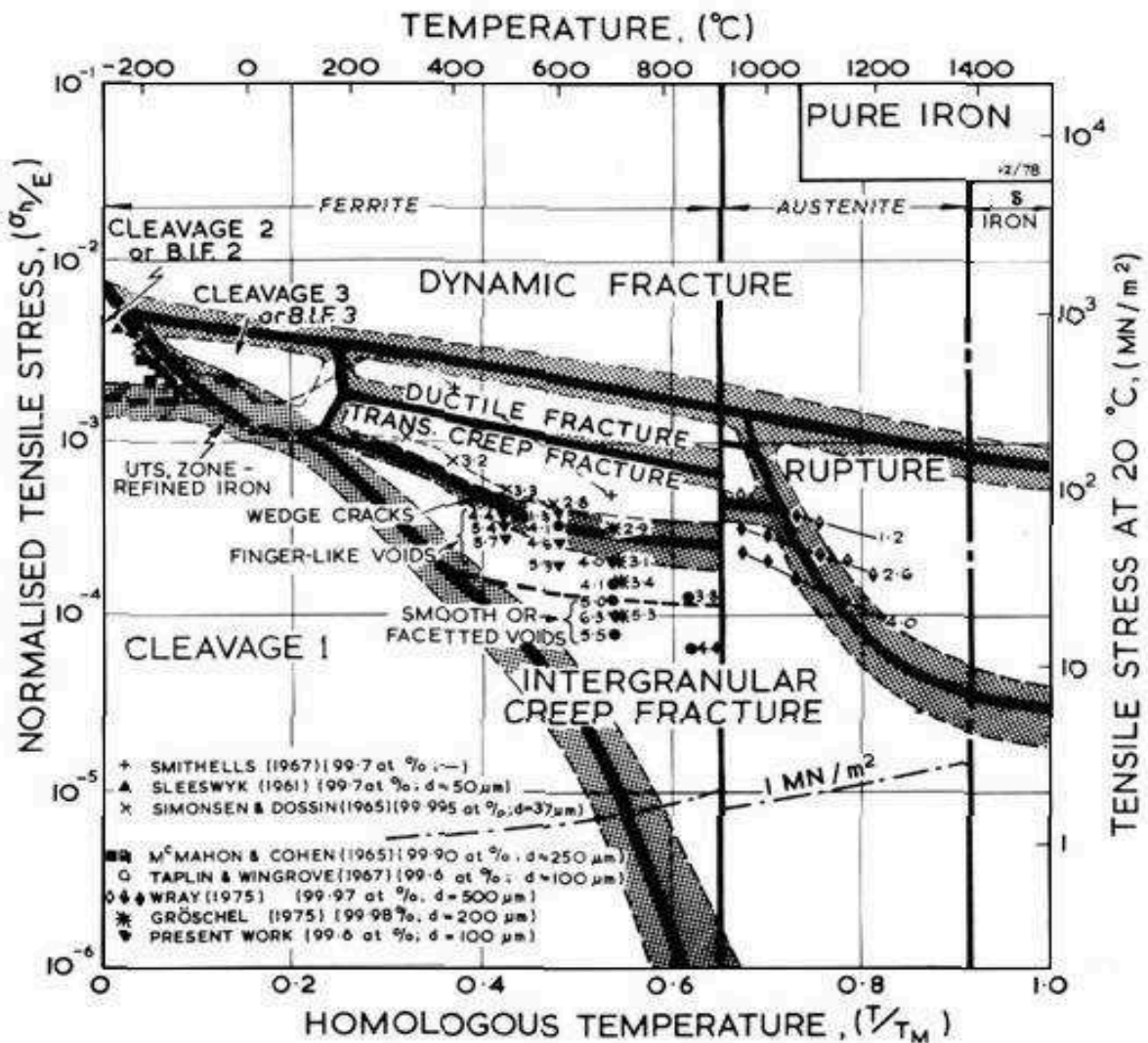


Fig.2.6: Pure Iron fracture mechanism map, [1]

The transition is progressive and is accompanied by a rupture ductility increase moving from intergranular to transgranular damage mechanisms.

Fig.2.7 shows the occurring fracture mechanisms in a 1CrMoV steel for different stress-rupture time coordinates.

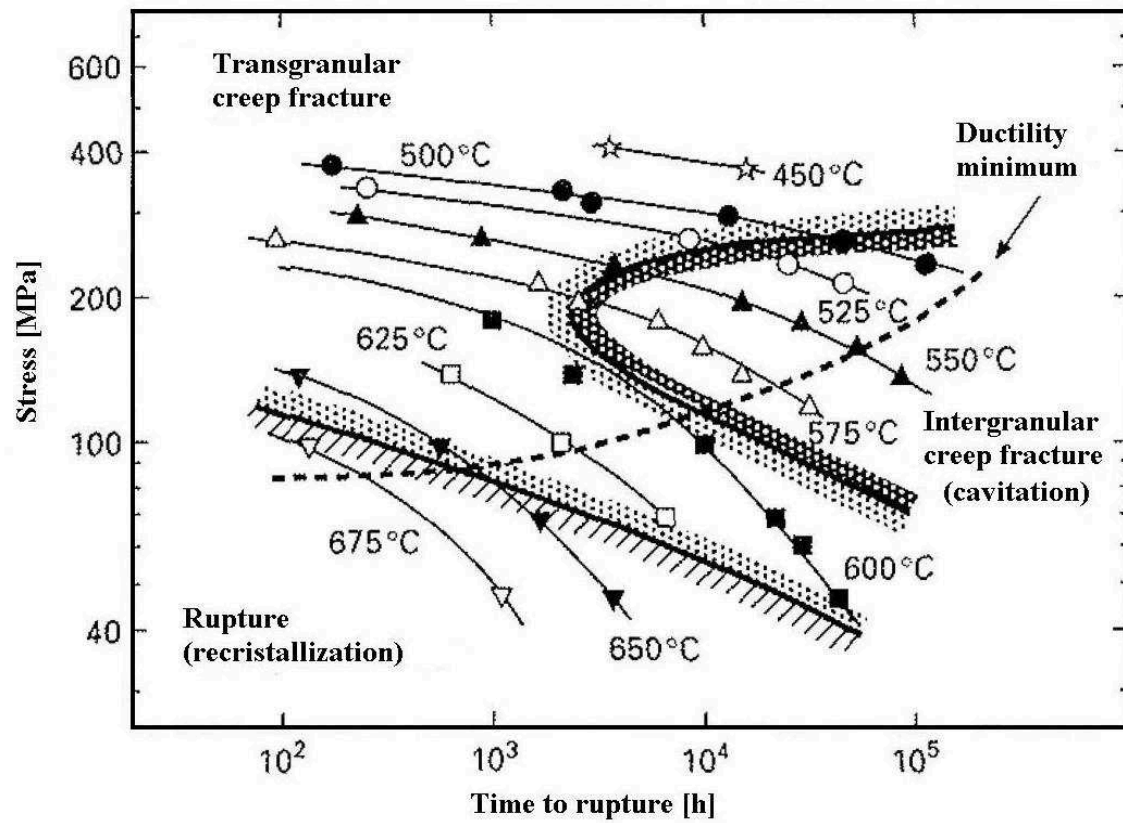


Fig.2.7: 1CrMoV fracture mechanism map, [1]

Intergranular fracture arises either by coalescence of cavities on grain boundaries aligned perpendicular to the direction of applied stress (C in Fig.2.8), or by wedge cracking formed at triple grain boundary junctions by stress concentration due to grain boundary sliding (W in Fig.2.8), or by a combination of them.

Transgranular fracture occurs due to void nucleation at inclusions coalesced by deformation (T in Fig.2.8).

The non-linear relation between stress and rupture time in Fig.2.8 is a consequence of different creep mechanism regimes, in which the activation energy is different for different stress levels.

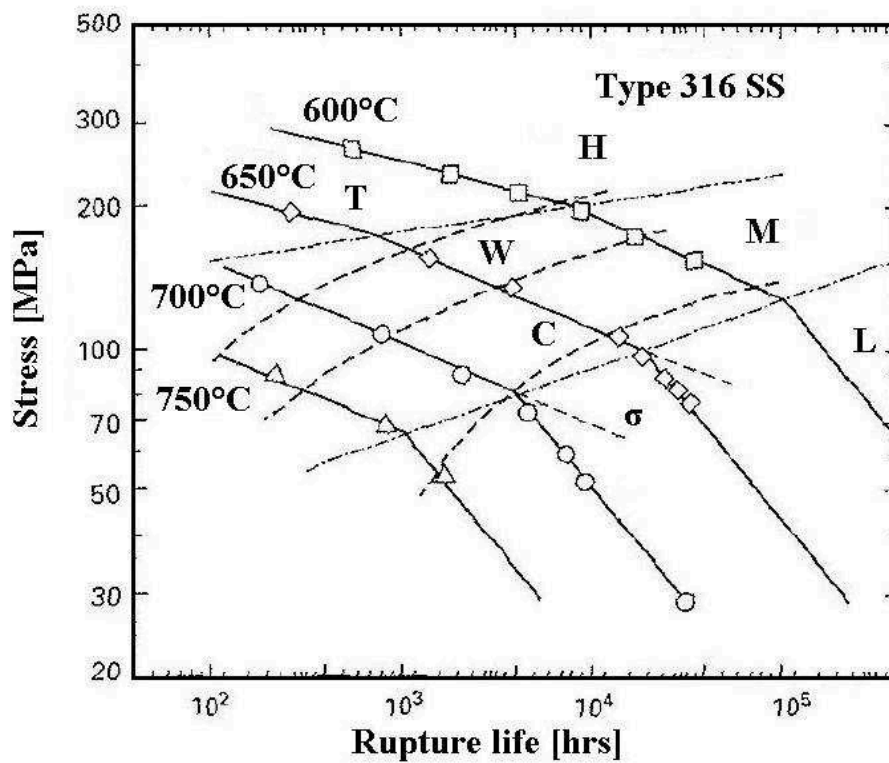


Fig.2.8: Type 316SS fracture mechanism map, [1]

Light microscopy allows to identify the creep damage conditions, as it is shown in Fig.2.9 and Fig.2.10. At low stress, boundary diffusion leads to intergranular failure modes characterized by grain boundary cavities coalescing perpendicular to the applied load direction (see Fig.2.9).

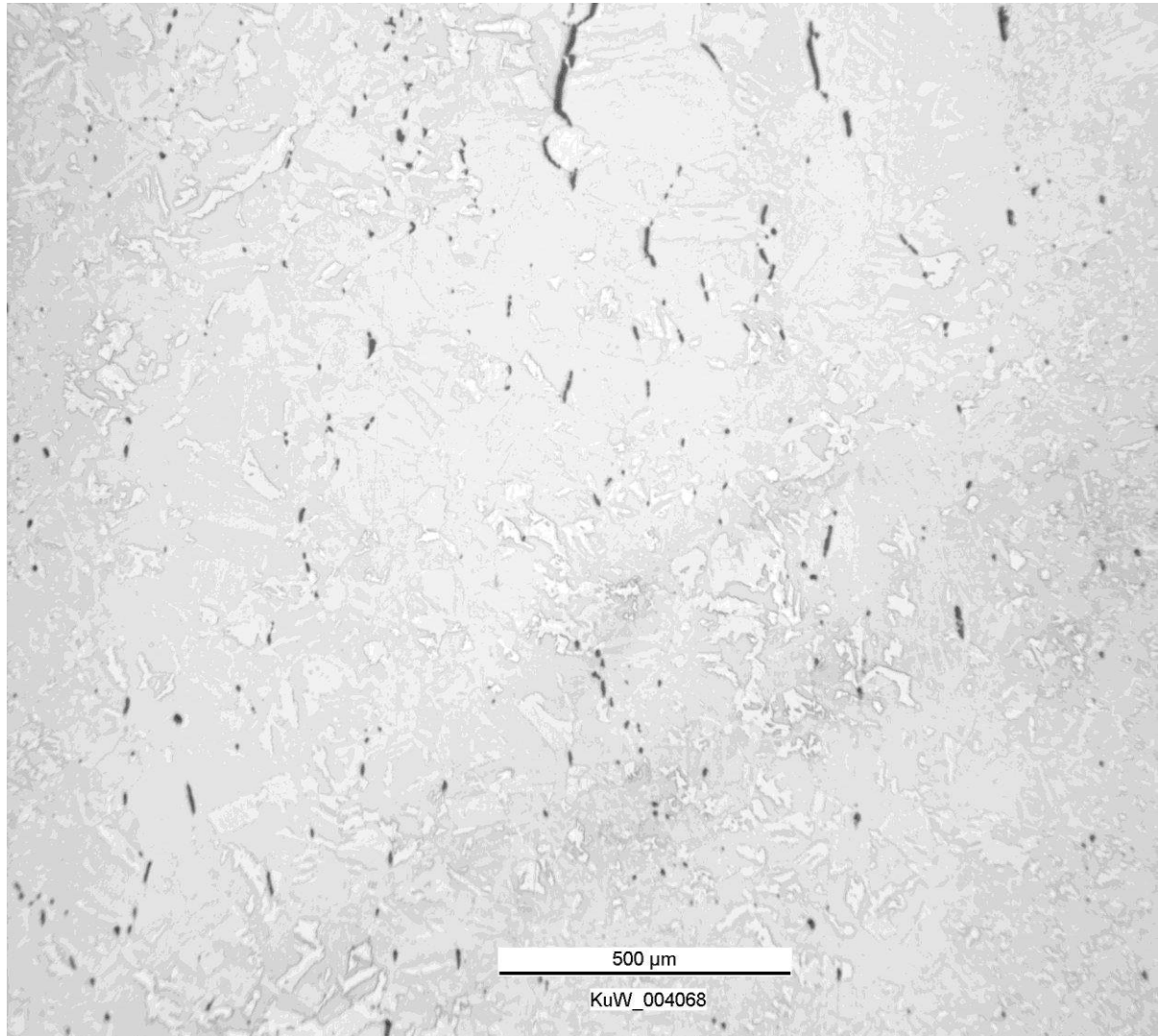


Fig.2.9: Intergranular creep damage in the form of cavities coalescing perpendicular to the applied load direction, in 1CrMoV (550°C, 211MPa, 33565hours)

At high stress, lattice diffusion leads to transgranular failure modes due to matrix-particle decohesion nucleated at inclusions (see Fig.2.10).

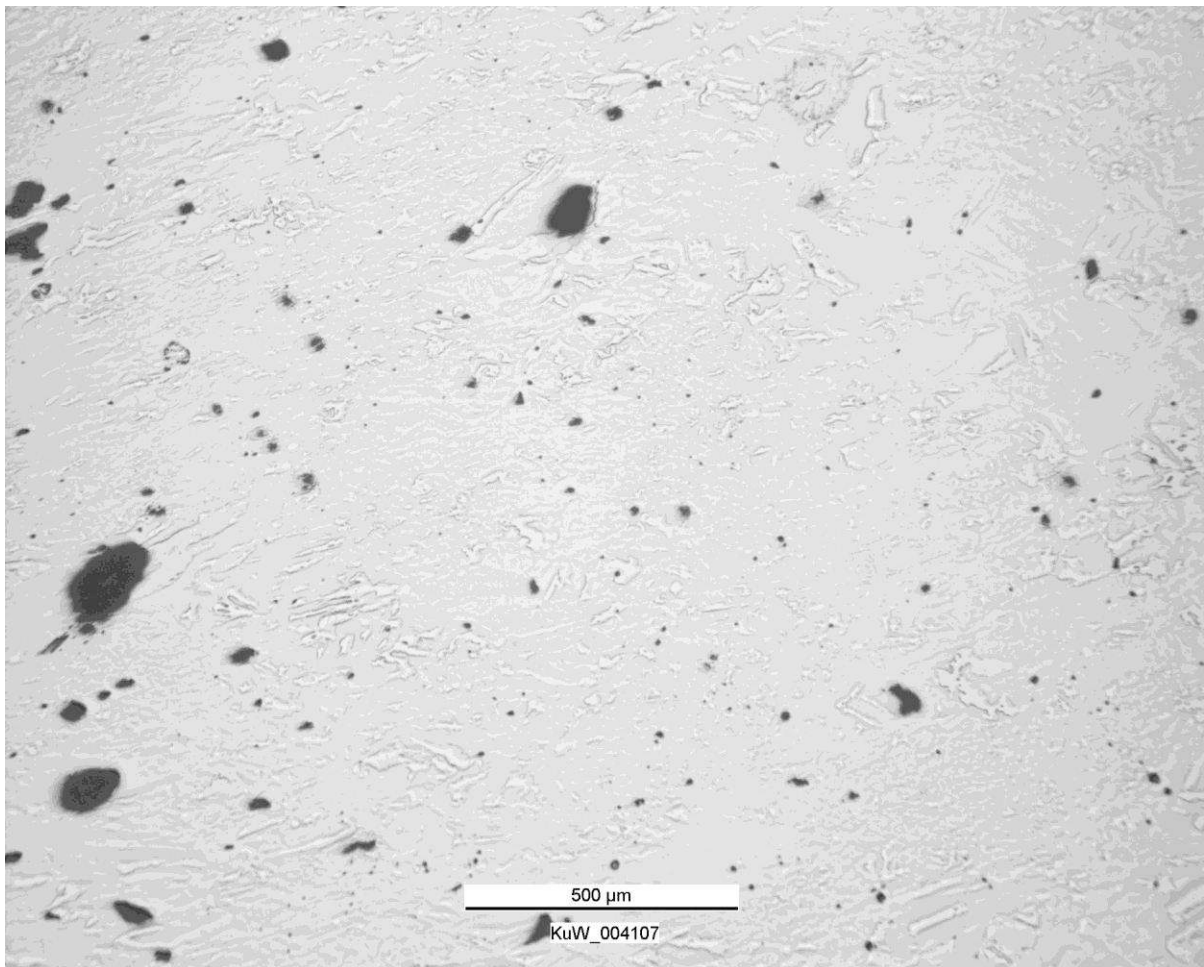


Fig.2.10: Transgranular creep damage in 1CrMoV (550°C, 306MPa, 1154hours)

2.1.3 Creep Ductility

The most common way to represent the creep ductility is either as a function of the creep strain rate or as a function of the creep rupture time.

The creep loading condition influences the deformation mechanism and hence the damage mechanism, as observed in paragraphs 2.1.1.1 and 2.1.2.3, ultimately affecting the creep rupture properties of the steel.

Fig.2.11 and Fig.2.12 show how the creep rupture ductility varies with respect to different creep strain rates and creep rupture times according to the activated creep damage mechanisms.

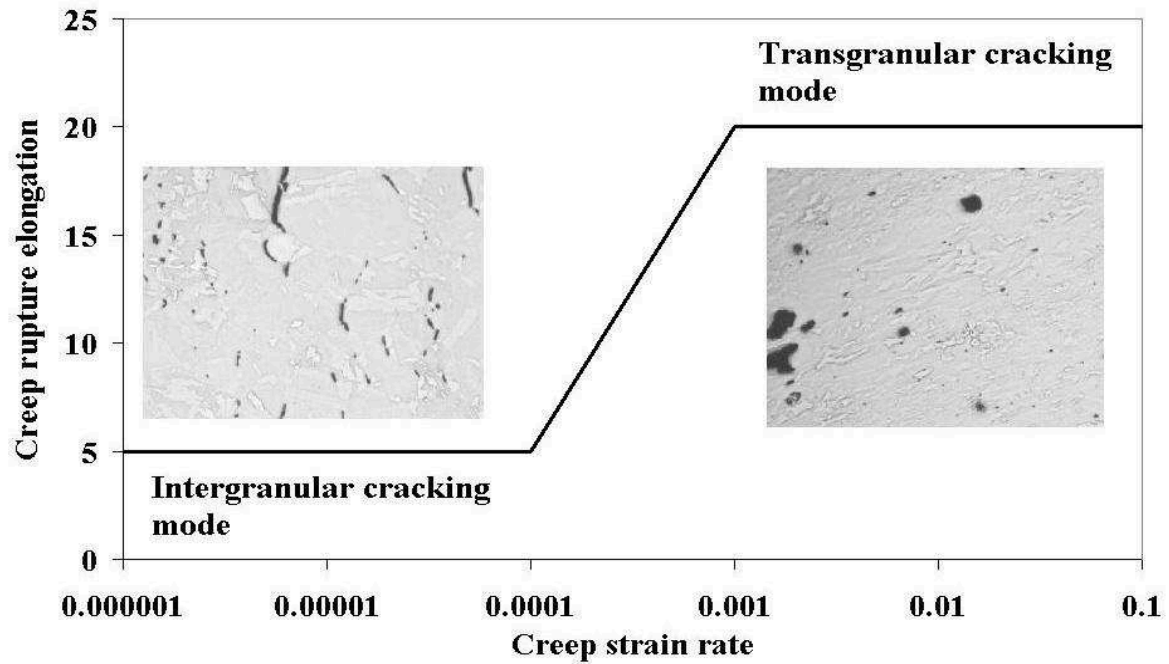


Fig.2.11: Creep ductility as a function of the creep strain rate for different damage mechanisms

The creep rupture ductility is generally low when the creep damage mechanism is an intergranular one arising from grain boundary cavitation, typically at low creep strain rates and high rupture times (eg. Fig.2.11 and Fig.2.12). The ductility is high when the creep damage mechanism is a transgranular one arising from matrix-particle decohesion, typically at high creep strain rates and low rupture times (eg. Fig.2.11 and Fig.2.12).

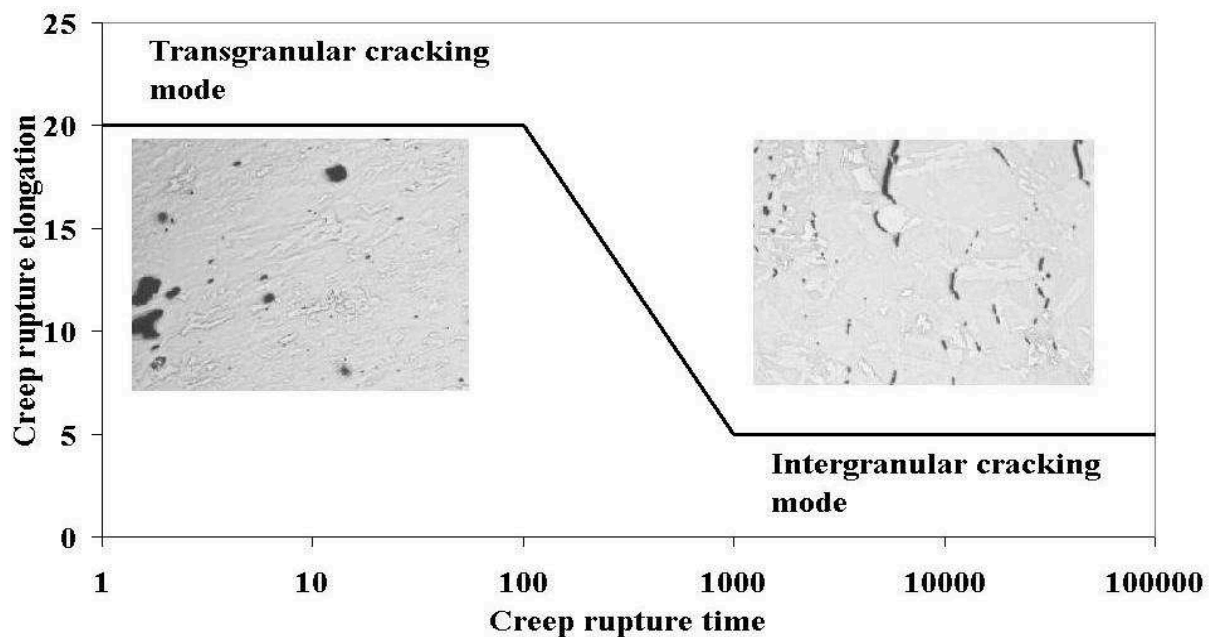


Fig.2.12: Creep ductility as a function of creep rupture time for different damage mechanisms

2.2 Fatigue

2.2.1 Fatigue deformation

The Ramberg-Osgood equation [52] describes the non linear relationship between stress and strain:

eqn.2.9

$$\varepsilon = \frac{\sigma}{E} + k \cdot \left(\frac{\sigma}{E} \right)^n$$

where k, n are material constants which describe the plastic component of strain. The n-base exponential law is able to describe particularly well the stress-strain response of a material characterised by non-linear hardening. The equation describes the monotonic stress-strain curve as well as the cyclic stress-strain curve.

TMF numerical analyses were performed on the basis of a constitutive model, representative of the material behaviour, which was characterized by a non-unified model approach. The cyclic deformation approach was described by a time independent plastic strain model which was developed on the basis of the non-linear isotropic-kinematic hardening model proposed by Lemaitre and Chaboche [38].

The yield criterion and the evolution equation for the “back stress” tensor X are:

eqn.2.10

$$f = J_2 \cdot (\sigma - X) = \sigma_y$$

$$\dot{X} = C \cdot \dot{\varepsilon}_{pl} \cdot \frac{(\sigma - X)}{\sigma_y} - \gamma \cdot X \cdot \dot{\varepsilon}_{pl} + \frac{1}{C} X \dot{C}$$

$$\sigma_y = \frac{C}{\gamma} \cdot \left(1 - e^{-\gamma \cdot \varepsilon_{pl}} \right) + \sigma_0$$

where σ is the stress tensor, J_2 the second invariant of the deviatoric stress tensor and ε_{pl} the equivalent plastic strain. The parameters σ_0 , C and γ were determined from monotonic elastic-plastic stress-strain curves.

2.2.2 Fatigue damage

The Coffin-Manson relation describes the low cycle fatigue endurance:

eqn.2.11

$$\frac{\Delta \varepsilon_p}{2} = \varepsilon_f' (2N)^c$$

where $\Delta \varepsilon_p/2$ is the plastic strain amplitude, ε_f' is the failure strain for a single reversal, $2N$ is the number of reversals to failure (i.e. N is the number of cycles) and c is a material constant (-0.5 ± -0.7).

Where there are k different strain magnitudes in a spectrum, $\varepsilon_j (1 \leq j \leq k)$, each contributing $n_j(\varepsilon_j)$ cycles, then if $N_j(\varepsilon_j)$ is the number of cycles to failure of a constant stress reversal ε_j , failure occurs when:

eqn.2.12

$$\sum_{j=1}^k \frac{n_j(\varepsilon_j)}{N_j(\varepsilon_j)} = C$$

where C is experimentally found to be between 0.7 and 2.2. For design purposes C is assumed to be 1 in this equation, which is widely known as the Miner rule.

Failure is usually defined according to two main criteria:

- $N = N_i$, number of cycles to the stress-cycle response deviation from the stability regime line
- $N = N_{2\%}$, number of cycles to a 2% load drop from the stress-cycle stability regime line

Such concepts are shown in Fig.2.13.

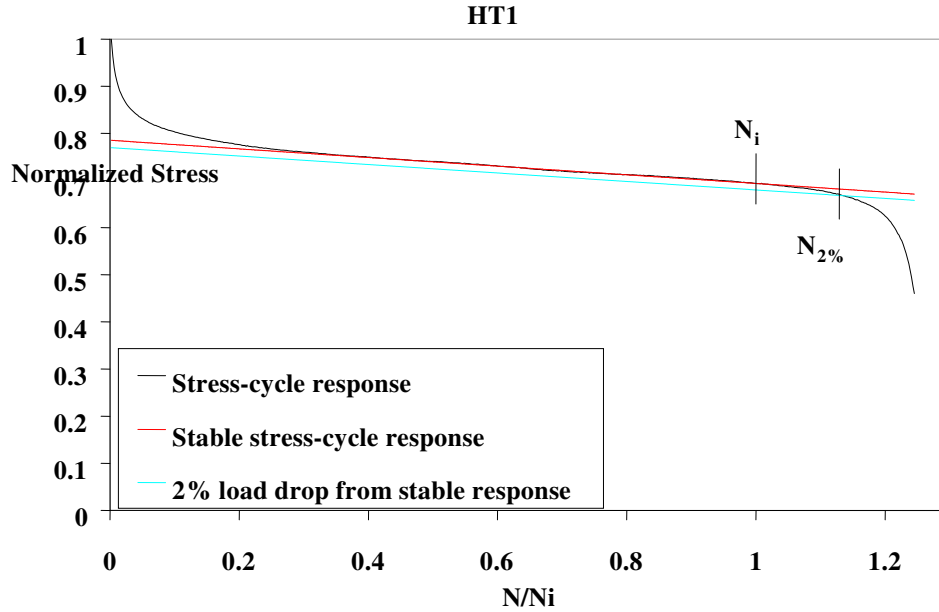


Fig.2.13: Stress-cycle response and fatigue failure criteria N_i and $N_{2\%}$

2.2.2.1 Fatigue damage mechanisms

The process of fatigue can be generally divided into a number of stages, each of them involving either different damage mechanisms or being governed by different stress criteria, ultimately leading to failure. A simple multi-stage fatigue model proposed by Plumbridge-Ryder [48] entails the following processes:

- Crack initiation, which occurs within the 10% of the fatigue life of ductile materials but may not occur at all in brittle material-notched testpieces. Cracks initiate however in slip bands at the free surface through dislocations glide mechanisms controlled by the shear stress.
- Slip-band crack growth, where the crack grows along the maximum shear stress plane through dislocations glide mechanisms. This stage can last till 90% of fatigue life in ductile materials, but may not occur at all in brittle material-notched testpieces.
- Crack growth on high tensile stress planes, where the process is controlled by the stress intensity at the crack tip. This stage can occupy the last 10% of the fatigue life of ductile materials, but it may also last up to the whole fatigue life in brittle-material-notched testpieces.

According to Plumbridge-Ryder [48] this simple model seems to adequately describe high-strain (LCF) as well as low strain (HCF) cyclic deformation.

The fatigue crack initiation and growth phenomena were also observed by Thompson [61], who recognized through HCF tests that fatigue cracks initiate on slip bands at the free surface and who realized that by removing surface material (e.g. by electro-polishing) the initial con-

dition were restored: this allowed them to state that by continuous surface material removal, the fatigue life could be indefinitely extended.

2.3 Creep-fatigue damage characterisation

Depending on the applied loading conditions, creep damage and fatigue damage may arise or not, and under particular circumstances the damage may be given by creep and fatigue interaction (see Fig.2.14).

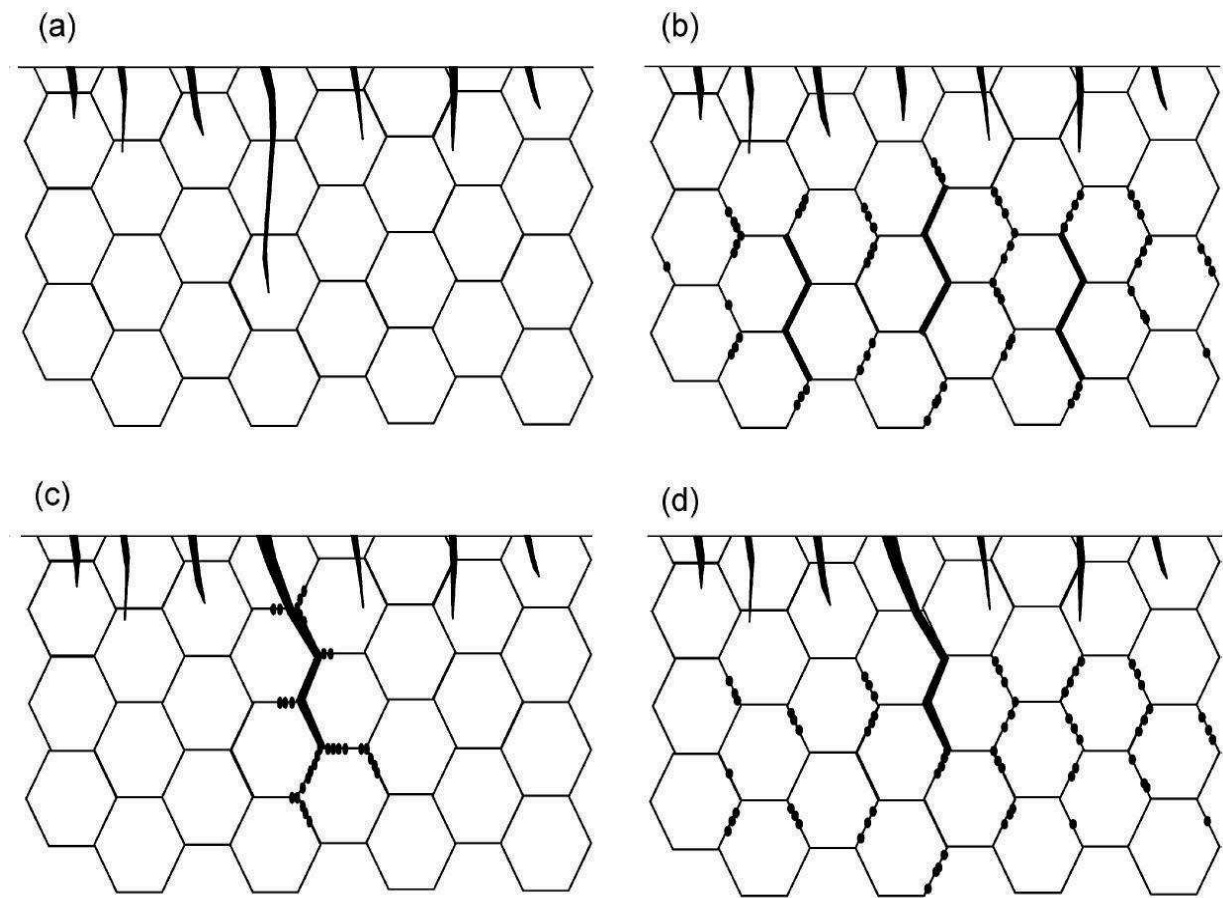


Fig.2.14: Creep-fatigue failure mechanisms: a) fatigue dominated, b) creep dominated, c) creep-fatigue interaction (due to consequential creep damage accumulation), d) creep-fatigue interaction (due to simultaneous creep damage accumulation), [33]

Fatigue damage (calculated on the basis of the Miner rule) and creep damage (either on the basis of the time fraction rule or on the basis of the ductility exhaustion rule) are accounted together to provide indication of the remaining life of a component or to design its operating lifetime.

A number of creep-fatigue assessment procedures rely on a bi-linear damage summation locus of the type shown in Fig.2.15, e.g. [2],[54] and [51]. This may be analytically represented by, e.g. [30].

$$D_F = 1 - D_C \cdot (1 - D'_F) / D'_C \quad \text{for } D_C < D'_C$$

$$D_F = (1 - D_C) \cdot D'_F / (1 - D'_C) \quad \text{for } D_C > D'_C$$

where (D'_C, D'_F) defines the intersection co-ordinate in the bi-linear damage locus construction Fig.2.15.

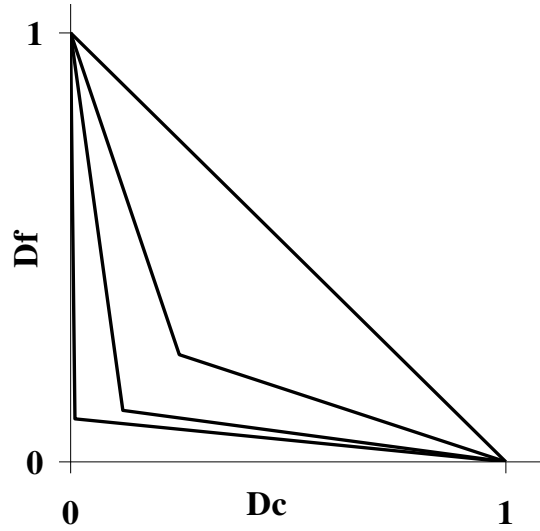


Fig.2.15: Bi-linear damage locus construction

For linear damage accumulation, $(D'_C, D'_F) = (0.5, 0.5)$.

Typically, the (D'_C, D'_F) co-ordinate is empirically derived and very dependent on the method of determination of D_F and D_C for the source damage co-ordinates used to determine the intersection point. It has been analytically demonstrated that (D'_C, D'_F) is unlikely to be less than $(0.33, 0.33)$ [58], and yet values of $(0.12, 0.12)$ and even $(0.01, 0.10)$ are given in published standards, e.g. [2]. These low co-ordinates are most probably due to the adopted magnitude of the damage fraction normalising parameter, e.g. $N_i(T, \varepsilon_a)$ in eqn.2.12 and $t_u(T, \sigma_t)$ in eqn.2.6. For example, D_F can be underestimated if $N_i(T, \varepsilon_a)$ does not account for the effect of creep condition (e.g. softening) and/or fully reflect the extent of any enhanced oxidation interaction, arising for example due to accelerated oxidation kinetics during large thermal transients. Similarly, D_C can be underestimated as a consequence of neglecting the influence of cyclic loading on $t_u(T, \sigma_t)$.

3 CREEP

This chapter analyses the creep properties of 1CrMoV steam turbine rotor steel in terms of strength and ductility on the basis of literature review and tests performed at the EMPA High Temperature testing laboratory.

Observations of classic time-strain rate based relationship (Monkman-Grant), and its temperature independence in particular, are used here as the basis for creep lifetime prediction.

A rupture ductility model has been developed in order to take greater cognizance of the influence of the material pedigree on the creep properties and it is here proposed as tool for creep damage assessment.

This chapter forms also the basis to understand how the creep properties change as consequence of prior cyclic deformation, as will be discussed in chapter 5.

3.1 Creep tests on 1CrMoV

Creep tests were performed in accordance with [21] on a 1CrMoV steel at 550 °C [34] and at 565°C in the as-received condition. Details of the investigated 1CrMoV steel are given in appendix I.

For the creep tests at both 550°C and 565°C, stress values were selected in order to characterise the material creep properties for both high ductility transgranular and low ductility intergranular rupture. The obtained creep database is shown in Table3.1.

Table3.1 Results of creep tests performed at 550°C and 565°C

T [°C]	σ MPa]	t_u [hrs]	$\dot{\epsilon}_{min}$ [1/hrs]	A_u [%]	Z_u [%]	ϵ_f [%]	Data source
550	306	1154	$1.84 \cdot 10^{-5}$	15.4	72.5	129.1	[34]
550	287	3392	$6.5 \cdot 10^{-6}$	12.9	61.97	96.7	EMPA-HT227
550	275	5935	$3.17 \cdot 10^{-6}$	9.2	44.56	24.5	[34]
550	245	13439	$8.23 \cdot 10^{-7}$	5	24.5	28.1	[34]
550	211	33565	$2.5 \cdot 10^{-7}$	4.1	22	24.8	[34]
565	308	280.52	$9.0 \cdot 10^{-5}$	14.7	83.22	178.5	EMPA-HT12
565	308	446	$4.5 \cdot 10^{-5}$	6.7	73.44	132.6	EMPA-HT85
565	270	1947	$1.0 \cdot 10^{-5}$	9.7	62.68	98.6	EMPA-HT228
565	243	6799	$1.8 \cdot 10^{-6}$	5.01	17.23	18.9	EMPA-HT89

3.1.1 Post Test Inspections

As a generality, reducing the applied stress produces a progressive change in the creep damage mechanism from transgranular to intergranular, a reduction in the minimum creep strain rate, a reduction of creep rupture ductility and an increase in rupture time.

The hardnesses of crept materials were measured in accordance with [4]. The grain size of crept material was measured according to the intercept method given in [5].

3.1.1.1 Hardness

Measurements of the hardness of crept testpieces reveal a systematic softening with a decrease in the stress responsible for creep and the consequent change in damage mechanism from transgranular to intergranular (see Table3.2).

Table3.2: Vickers hardness measurements in creep specimen gauge sections (HV30)

As received	565°C - 308MPa	565°C - 270MPa	565°C - 243MPa	550°C - 306MPa	550°C - 287MPa	550°C - 275MPa	550°C - 245MPa	550°C - 211MPa
245	222	220	220	224	221	218	217	215

3.1.1.2 Grain size

The grain sizes of two crept testpieces (HT12 and HT85) subjected to 308MPa at 565°C were measured (see Table3.3). The average grain size of such crept material was 36.5µm, slightly larger than what observed in as-received material (34.5 µm, see appendix I), but not enough to justify a direct creep deformation-grain size correlation (also because the testpiece which experienced the largest creep deformation -HT12- shows smaller average grain size -35.4µm).

Table3.3: Grain size of material crept at 308MPa at 565°C

field	magnification	n°grains	grain size[µm]
1 (HT12)	X335	65	34.3
2 (HT12)	X335	61	36.6
3 (HT85)	X335	64	35.6
4 (HT85)	X335	57	40.0
AVG (total)		247	36.5

3.1.1.3 Creep damage

Optical microscopy activity was performed in order to characterize the creep damage with respect to different creep loading conditions. Fig.3.1 to Fig.3.3 show how the observed physical creep damage changes by changing the creep loading conditions. At high applied stresses, cavities nucleate at inclusions within the grains as a result of particle-matrix decohesion leading to transgranular creep failure, whereas at low stresses cavity nucleation occurs at grain boundaries leading to intergranular creep failure. At high stresses the cavity nucleation produced by a particle (e.g. inclusion) leads to a globular void usually elongated in the applied stress direction, as a consequence of the higher particle strength and of decohesion occurring at the particle-matrix interface lying on a perpendicular plane with respect to the max tensile stress direction Fig.3.1.

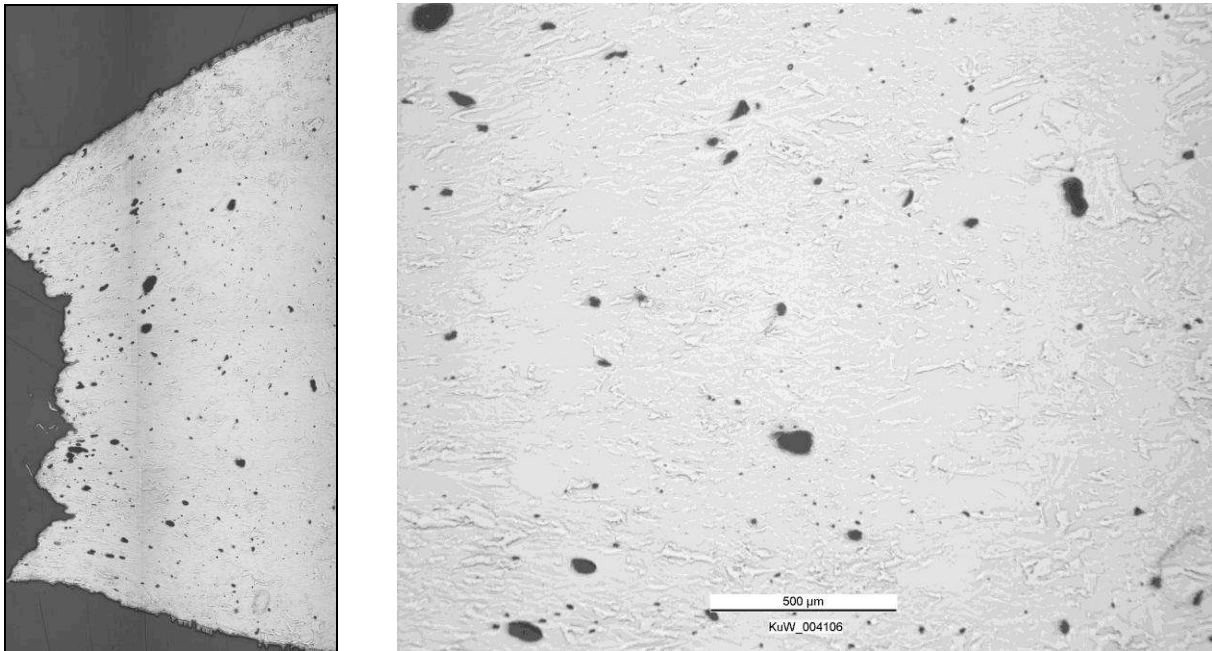


Fig.3.1: Creep: 550°C - 306MPa

At intermediate stress values the failure mode is a combination of intergranular and transgranular damage (Fig.3.2).

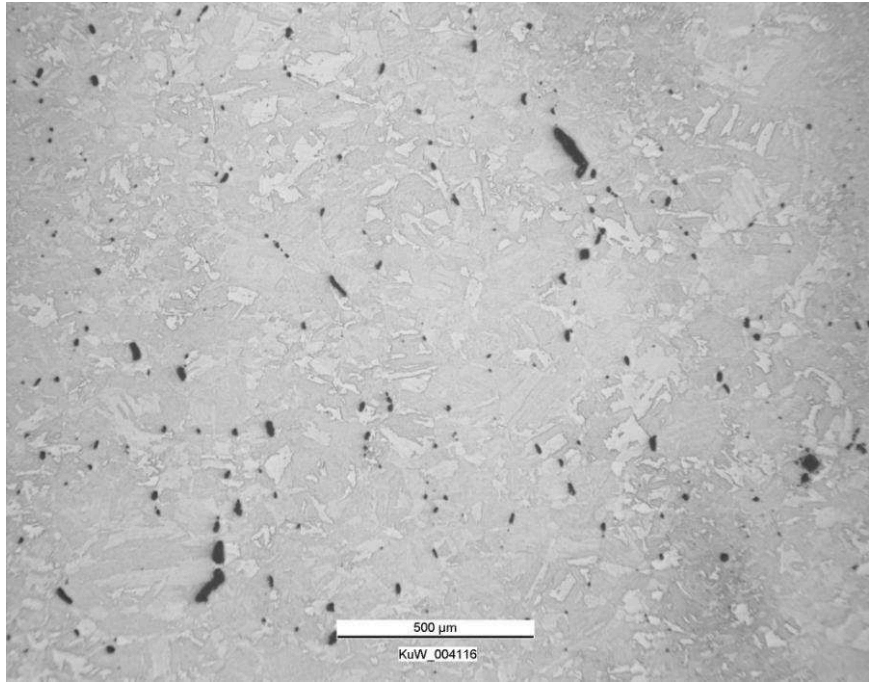
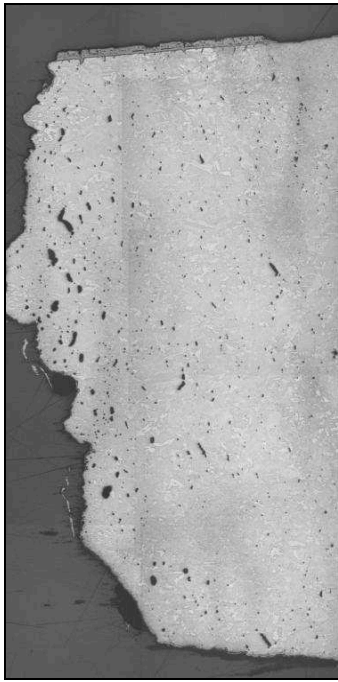


Fig.3.2: Creep: 550°C - 275MPa

At low stresses applied for a few thousand hours, grain boundaries suffer from dissolution and re-precipitation of carbides in a way that is harmful to strength and ductility. Cavities nucleate at prior austenite grain boundaries perpendicular to the stress direction, where the deformation tends to localize (Fig.3.3).

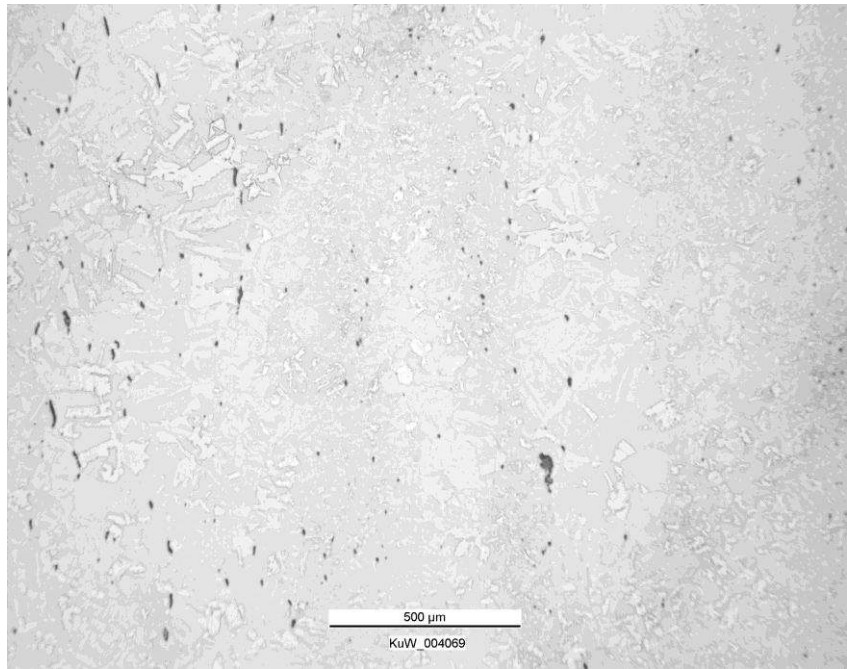


Fig.3.3: Creep: 550°C - 211MPa

3.1.2 Creep rupture properties

3.1.2.1 Creep strain

The effect of stress on the creep rupture properties of 1CrMoV steel at high application temperatures (550/565°C) is well known. According to the definition of the creep phases given in 2.1.1, the creep response of 1CrMoV is the following: with reducing stress, *i*) the proportion of primary and secondary creep strain increases, *ii*) the proportion of tertiary creep strain decreases, *iii*) the minimum creep rate decreases, *iv*) the rupture time increases and *v*) the rupture ductility decreases (Fig.3.4 and Fig.3.5).

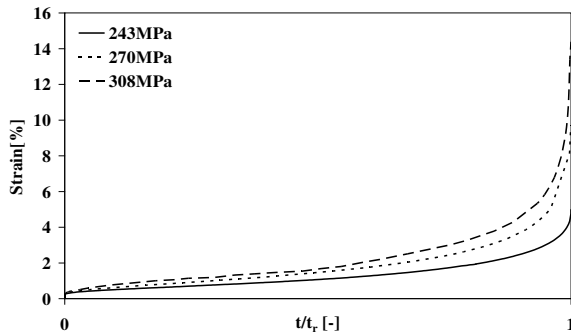


Fig.3.4: Creep curves for 1CrMoV at 565°C

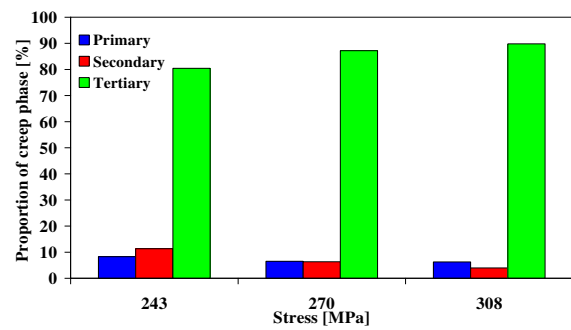


Fig.3.5: Creep regime proportions at 565°C, as described in Fig.2.1.

This observation is true for all (T, σ) loading conditions responsible for creep rupture. The influence of temperature on creep strength is shown in Fig.3.6, with rupture times reducing systematically with increasing temperature and stress. In Fig.3.6 the creep data were fitted with a Manson-Brown model [39], i.e.:

eqn.3.1

$$(P_{MB} =) \frac{\log(t_u) - \log(t_a)}{\left[\frac{T + 273.15 - T_a}{1000} \right]^R} = \sum_{i=0}^N B_i \cdot \log^i(\sigma)$$

where the adopted polynomial was of the second order, and the coefficients were as reported in Table3.4:

Table3.4: 1CrMoV, coefficients for interpolation with Manson-Brown model

$\log(t_a)$	T_a [K]	R	N	B_0	B_1	B_2
8.15	770	0.4	2	-630.715	541.7204	-118.494

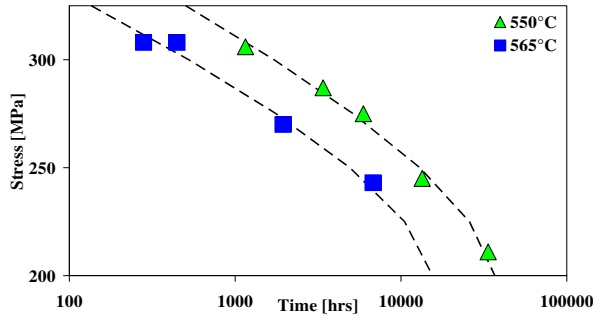


Fig.3.6: Influence of temperature on creep strength

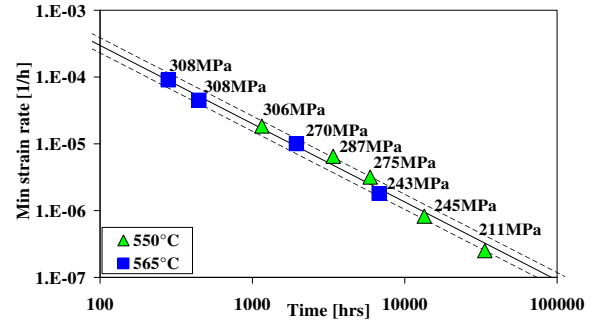


Fig.3.7: Influence of temperature on MG parameter

The reduction of rupture times and creep strain rates are directly related, as shown in Fig.3.7, such that the same Monkman-Grant (MG) relationship applies for all creep loading conditions applied to the same heat of 1CrMoV steel at temperatures in the range 450 to 675°C (e.g. as demonstrated by the evidence provided by the NRIM-1CrMoV creep data sheet [45] and shown in the paragraph 3.1.2.2). In particular, an increase of temperature and/or stress produces a displacement along the MG parameter line towards higher creep strain rates and lower rupture times. The Monkman-Grant relationship is represented by eqn.2.5, where for the 9 heats of 1CrMoV steel in [45], P_{MG} is $\sim 2-4$ depending on material characteristics.

3.1.2.2 The Monkman-Grant temperature independency

The temperature independency of the Monkman-Grant relation (eqn.2.5) can be demonstrated through the fundamental creep equations defining the creep behaviour of 1CrMoV:

Assuming that A, B, n, w, k, i may only be material pedigree dependent, the coefficients n, w, k, i of eqn.2.2 and eqn.2.4 were determined by fitting data coordinates [45] with

1. same material pedigree and same temperature (n,w)
2. same material pedigree and same stress levels (k,i)

The corresponding equations for the data coordinates belonging to the creep tests X, Y are:

$$n = \frac{\log\left(\frac{\dot{\epsilon}_X}{\dot{\epsilon}_Y}\right)}{\log\left(\frac{\sigma_X}{\sigma_Y}\right)} \quad \text{eqn.3.2;}$$

$$w = \frac{\log\left(\frac{t_{uX}}{t_{uY}}\right)}{\log\left(\frac{\sigma_X}{\sigma_Y}\right)} \quad \text{eqn.3.3}$$

for data coordinates with same material pedigree and testing temperature, and

$$k = \frac{\log\left(\frac{\dot{\varepsilon}_X}{\dot{\varepsilon}_Y}\right)}{\frac{Q}{R} \cdot \left(\frac{1}{T_X} - \frac{1}{T_Y}\right)} \quad \text{eqn.3.4;}$$

$$i = \frac{\log\left(\frac{t_{uX}}{t_{uY}}\right)}{\frac{Q}{R} \cdot \left(\frac{1}{T_X} - \frac{1}{T_Y}\right)} \quad \text{eqn.3.5}$$

for data coordinates with same material pedigree and stress level.

The coefficients A, B were then directly determined from the creep equations (eqn.2.2 and eqn.2.4) same material pedigree, after n, w, k and i were calculated:

$$A = \frac{\dot{\varepsilon}}{e^{\left(\frac{k \cdot Q}{R \cdot T}\right)} \cdot \sigma^n} \quad \text{eqn.3.6;}$$

$$B = \frac{t_u}{e^{\left(\frac{i \cdot Q}{R \cdot T}\right)} \cdot \sigma^w} \quad \text{eqn.3.7;}$$

Whereas k, i, n and w are constant from heat to heat, A and B vary for different material pedigrees.

Table3.5: Mean values and standard deviations for coefficients k, i, n, w of eqn.2.2 and eqn.2.4.

	k	i	n	w
AVG	-0.614	0.597	9.79	-9.34
data to data std dev	0.051	0.042	4.65	4.64
heat to heat std dev	0.035	0.023	0.508	0.589

Table3.6: Mean values for every heat of [45] for coefficients A, B of eqn.2.2 and eqn.2.4.

Heat	VaA	VaB	VaC	VaD	VaE
A	2.46E-15	4.29E-15	1.64E-15	2.4E-15	1.65E-15
B	2.39E10	2.56E11	1.13E10	3.74E11	3.08E11

Heat	VaG	VaH	VaJ	VaR
A	8.38E-16	1.28E-15	1.98E-15	1.7E-15
B	2.16E11	3.04E11	3.19E11	2.94E11

The data in Table3.5 show that the coefficient $k \cong -i$ and $n \cong -w$. This allows to solve eqn.2.2 and eqn.2.4 with respect to the stress:

eqn.3.8

$$\sigma = \sqrt[w]{\frac{t_u}{B \cdot e^{\left(\frac{i \cdot Q}{R \cdot T}\right)}}$$

and then to solve eqn.2.2 and eqn.2.4 through eqn.3.8:

eqn.3.9

$$\dot{\varepsilon} = A \cdot e^{\left(\frac{k \cdot Q}{R \cdot T}\right)} \cdot \left(\frac{t_u}{B \cdot e^{\left(\frac{i \cdot Q}{R \cdot T}\right)}} \right)^{\frac{n}{w}}$$

which, assuming $k = -i$ and $n = -w$, becomes:

eqn.3.10

$$\dot{\varepsilon}_{\min} = A \cdot B \cdot t_u^{-1} = P_{\text{MG}} \cdot t_u^{-1}$$

It can be concluded that for every heat of 1CrMoV of [45] the Monkman-Grant equation (eqn.3.10) is independent from the temperature.

3.1.2.3 Creep ductility

The influence of minimum creep strain rate and temperature on the creep rupture ductility of 1CrMoV steel, heat 1 EMPA [13] and [34] is shown in Fig.3.8.

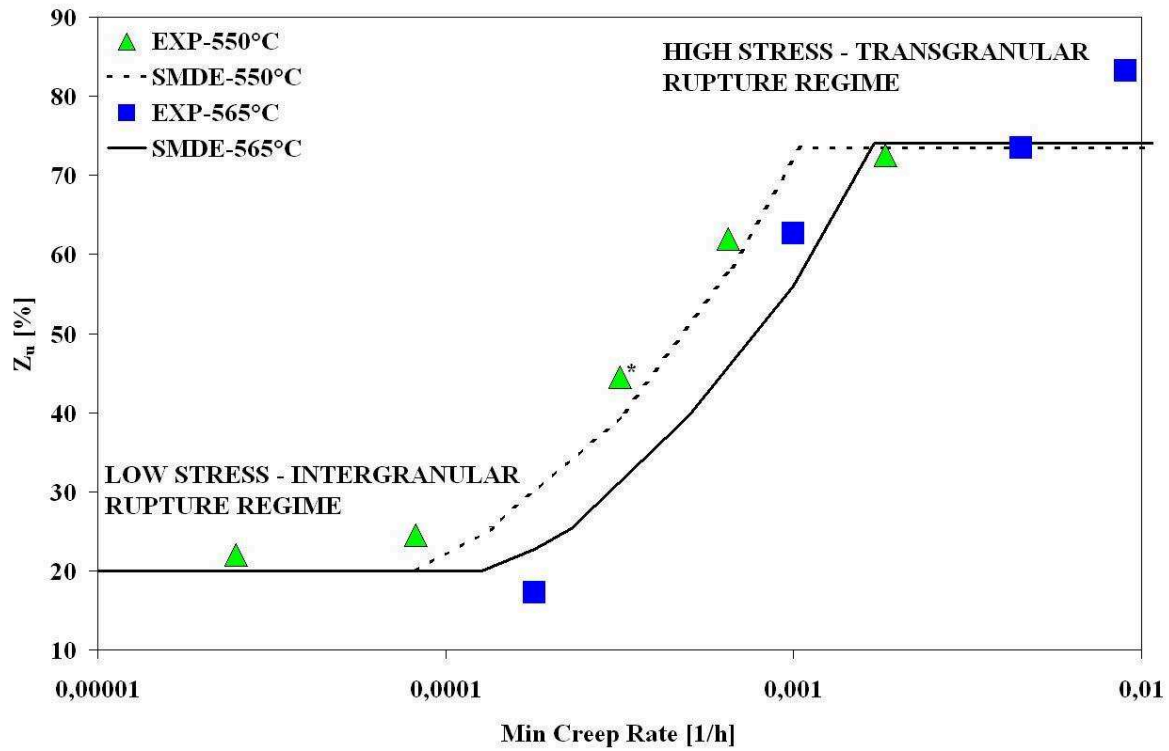


Fig.3.8: Influence of temperature on $Z_u(\dot{\epsilon})$ of 1CrMoV, heat 1 (EMPA [13] and [34]) (lines represent model predictions). * indicates the creep rupture ductility (Z_u) was calculated on the basis of elongation at rupture (A_u).

Creep rupture ductility values are normally expressed in this dissertation in terms of Z_u , being the area reduction a directly measurable variable and hence preferred with respect to other ductility representative parameter like, for instance, the local elongation at rupture. Z_u was also preferred to the total elongation measure, because it represents the really occurred deformation in the ruptured area.

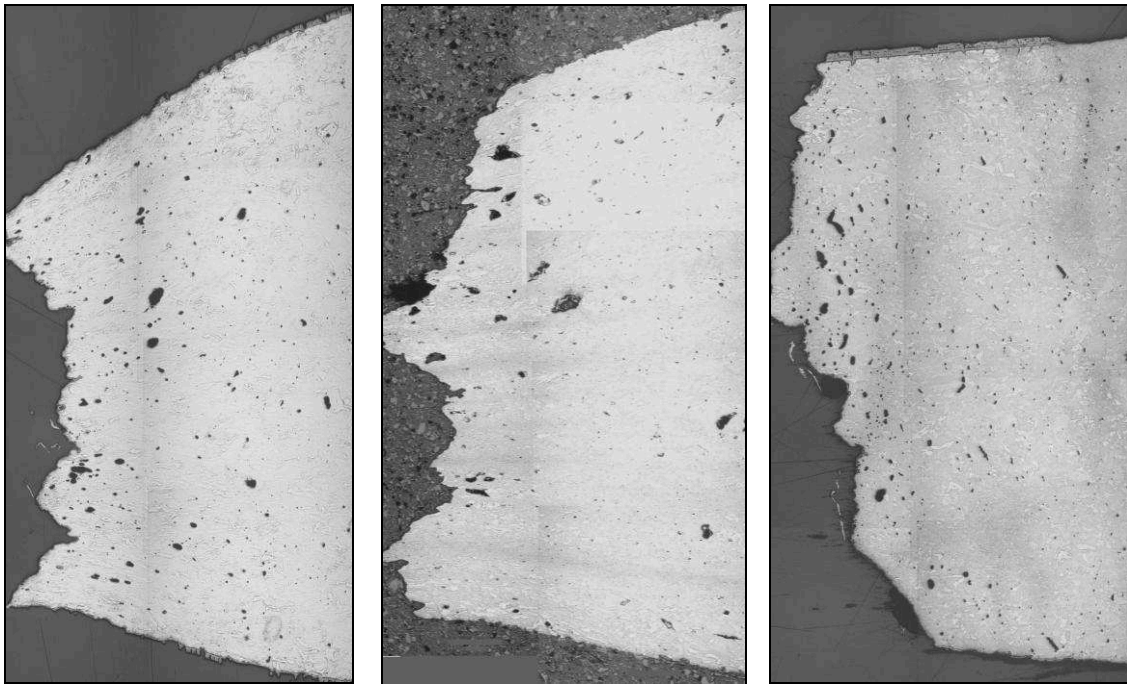
The variation of rupture ductility with stress is strongly related to the rupture mechanism. The dependence of the creep rupture ductility on stress as well as on strain rate is worth of mention as far as this model is concerned: in fact it is common practice to represent ductility as a reference of the minimum creep rate and this stress modified approach for the modelling of the creep rupture ductility may seem to be overcomplicated. Indeed it reflects the purpose of developing a model in which all the creep input parameters are treated as independent variables.

As a direct consequence it is also important to say that the creep rupture data points as well as the creep rupture ductility lines plotted in Fig.3.8 and the similar following are obtained for constant temperature levels and different values of minimum creep rate and stress.

The photo-micrographs contained in Fig.3.9 (and partially already seen in paragraph 3.1.1.3) show the observed physical creep damage resulting from a series of creep tests performed at 550°C [34], the $Z_u(\dot{\epsilon})$ properties for which are contained in Table3.1.

Rupture ductility remains high on the upper-shelf when the test stress is reduced in the high stress regime in which damage develops relatively late in life as a consequence of particle/matrix decohesion and rupture is by a creep ductile-transgranular, dimple-rupture mechanism (Fig.3.9a). At lower stresses (and longer rupture times), rupture ductility remains relatively low, with reducing stress, on the lower-shelf. In the lower-shelf regime, damage develops as cavities on grain boundaries, from as early as the onset of tertiary creep (depending on the magnitude of the creep ductility of the specific cast of 1CrMoV steel), and rupture is by a creep brittle intergranular mechanism (Fig.3.9e). At stresses responsible for rupture between the upper and lower shelf regimes, the rupture ductility decreases continuously with reducing stress and the rupture mechanism is mixed transgranular/intergranular (Fig.3.9c).

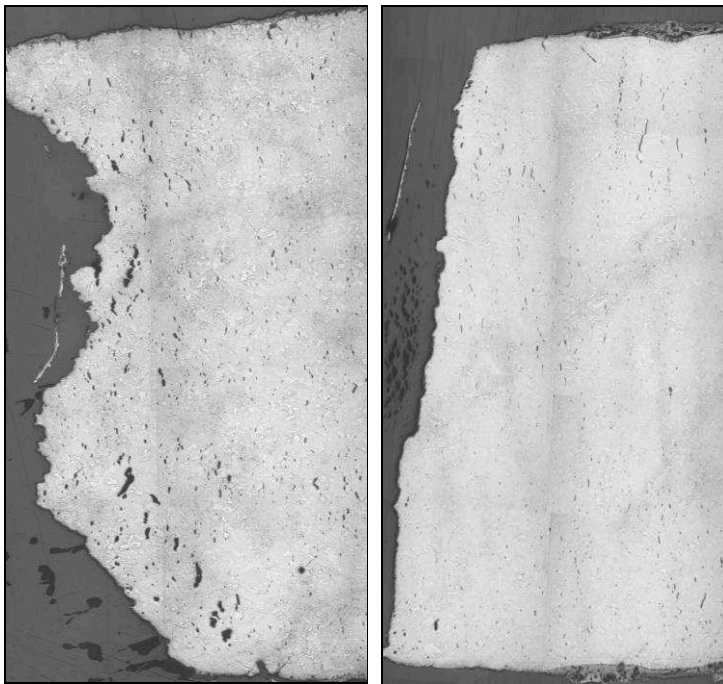
Fig.3.9: Influence of the applied stress on creep damage mechanisms



a. Creep: 550°C - 306MPa

b. Creep: 550°C - 287MPa

c. Creep: 550°C - 275MPa



d. Creep: 550°C - 245MPa

e. Creep: 550°C - 211MPa

3.2 The Exhaustion of Creep Ductility in 1CrMoV Steel

This chapter presents a creep rupture ductility model implemented on the basis of the standard stress-modified ductility exhaustion (SMDE) approach and modified to include the effect of the material pedigree. Further details can be found in [14].

3.2.1 Introduction

While there have been significant developments in the understanding and assessment of creep rupture behaviour during the recent past [29], the focus has primarily concerned strength and strain accumulation properties rather than rupture ductility. The importance of being able to accurately represent creep rupture ductility behaviour has become more acute with the increasing use of ductility exhaustion as a measure of the creep damage accumulated as a consequence of secondary self-equilibrating loading in the assessment of high temperature components subject to creep-fatigue loading, e.g. [51] and [59]. However, in addition there is a requirement for long duration rupture ductility properties to provide the basis for design life limits for components containing multi-axial features [28].

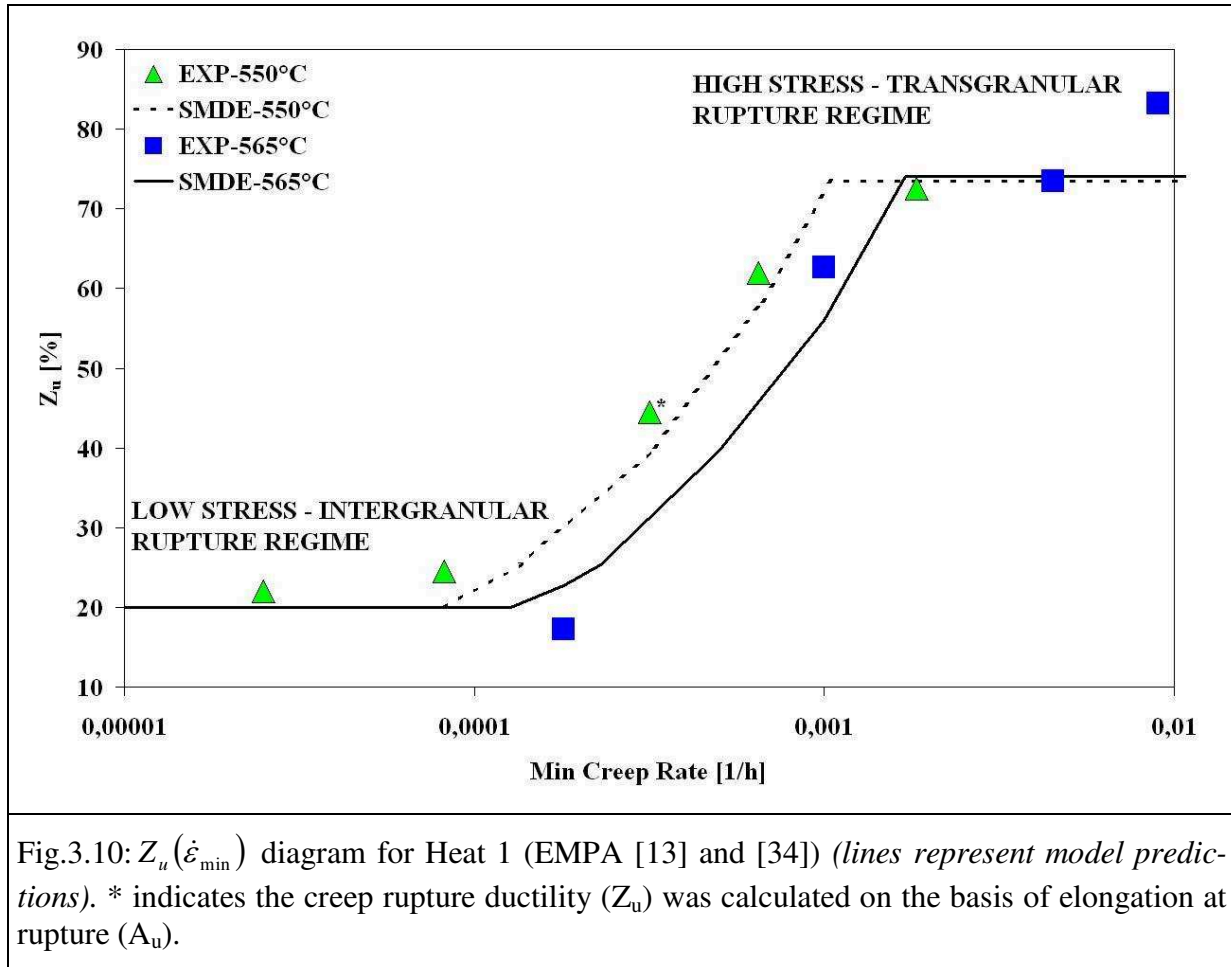
There have been advances in the development of more effective rupture ductility models (e.g. the SMDE model [59]), but there is still scope for improvement. A major complexity with the assessment of rupture ductility data is the large material heat-to-heat variability which is much greater than that for creep strength data [31]. This chapter presents a material pedigree enhanced version of the stress based ductility exhaustion model of Spindler [59] which has been devised to further accommodate the extent of this inherent variability for 1CrMoV steel.

The basis for the developed material pedigree functions is a comprehensive review of published literature on the influence of compositional and heat treatment variables on the creep rupture properties of CrMoV type steels, and the results of this are summarised in this chapter. This information underpins the individual parameter $f(\text{mp})$ functions which are normalised with respect to the mean variable quantities for 1CrMoV steel. The effectiveness of the newly proposed creep rupture ductility model is tested with reference to observations collated in a dataset comprising the results of 88 tests involving, for 10 heats of 1CrMoV steel, a comprehensive range of temperatures and loading conditions responsible for a complete spectrum of the rupture mechanisms encountered in practice for this steel [13], [34] and [45].

3.2.2 Creep Rupture Ductility Model

The rupture ductility of 1CrMoV remains high for relatively high stress loading conditions responsible for high creep strain rates and ductile-transgranular failure arising from matrix/particle decohesion and plastic growth. In contrast, rupture ductility is low for the relatively low stress loading conditions responsible for low creep strain rates and intergranular

failure due to constrained grain boundary cavity nucleation and growth (Fig.3.10). For intermediate stress loading conditions the creep damage mechanism is mixed as the rupture ductility decreases with decreasing strain rate due to reducing the applied stress.



The data shown in Fig.3.10 cover the practical range for engineering assessment. Creep damage calculations for this type of application are typically based on ductilities in the transition regime and at the beginning of the upper shelf regime.

The new ductility model aims to represent the transition between lower-shelf intergranular rupture and upper-shelf ductile-transgranular rupture as a function of temperature, strain rate, stress and material pedigree.

Lower and upper shelf rupture ductilities are based directly on observations from the data collated from references [13], [34] and [45], and determine the lower and upper limits for the transition regime. In this model, the dependence of $Z_{u,L}$ and $Z_{u,U}$ on the material pedigree and/or on stress is neglected. In practice, both the lower and upper rupture ductility limits depend on temperature. There is also likely a recovery in creep rupture ductility at very low creep strain rates at high temperatures. The consideration of these effects is not the present objective.

In the following text, the focus is on the transition regime, which is characterised by a $Z_u(T, \dot{\epsilon}_{\min}, \sigma, f(\text{MP}))$ model able to define the region between $Z_{u,L}$ and $Z_{u,U}$, i.e by the following logic equation:

eqn.3.11

$$\text{for } Z_{u,L} < Z_u < Z_{u,U} \quad Z_u(T, \dot{\epsilon}_{\min}, \sigma, f(\text{MP})) = A \cdot f(\text{MP}) \cdot e^{\left(\frac{Q}{R(T-T_{\text{ref}})}\right)} \cdot (\dot{\epsilon}_{\min})^m \cdot \sigma^{-n}$$

where upper shelf ductility has been modelled as a function of temperature between 450°C and 575°C, i.e.:

eqn.3.12

$$Z_{u,U} = (52.2 + 0.0387 \cdot T)$$

whereas at temperatures lower than 450°C and higher than 575°C $Z_{u,U}$ has been modelled to remain constant. This function representative of $Z_{u,U}$ was determined by linear regression of the project dataset $Z_{u,U}(\dot{\epsilon})$ co-ordinates remote from the transition regime (i.e. with $\dot{\epsilon}_{u,U}$ values 50% greater than those at the upper end of the transition region). $Z_{u,U}$ remained constant for values of $\dot{\epsilon}_{\min}$ and σ responsible for ductile-transgranular rupture, this being confirmed by results from tensile tests performed at constant strain rates of 0.004/min (0.24/h) at 525°C and 575°C for which the area reduction at fracture was respectively 76.4% and 82.5%. The model parameter values adopted in eqn.3.11 and eqn.3.12 for the 1CrMoV steel are summarised in Table3.7.

Table3.7: Summary of Model Parameter Values for 1CrMoV

$Z_{u,L}$ [%]	$Z_{u,U}$ (450°C) [%]	$Z_{u,U}$ (575°C) [%]	A	Q [KJ/mol]	R [J/molK]	T_{ref} [K]	n	m
20.0	69.6	74.5	152	289.0	8.314	400	0.605	1.2695

The exponents n and m in Table3.7 are consistent with those adopted in reference [59], and apply equally well for the 1CrMoV steel. Other parameters were optimised with respect to the compiled dataset [13], [34] and [45] to achieve the best model fitting.

In the model defined by eqn.3.11 and eqn.3.12, creep ductility is expressed in terms of Z_u . Alternatively, it may be considered in terms of local fracture strain at rupture, i.e. eqn.3.13.

eqn.3.13

$$\epsilon_f = \ln\left(\frac{1}{1 - Z_u/100}\right)$$

Independent functions have been determined to cover the effects of a range of material pedigree parameters relating to chemical composition and heat treatment on creep rupture proper-

ties (and rupture ductility in particular). On the basis of these, the means to determine an overall material pedigree function for individual heats of 1CrMoV steel is proposed, i.e. $f(\text{MP})$.

The model prediction lines plotted in Fig. 3.10 were constructed by joining the $Z_u(\dot{\epsilon}_{\min})$ co-ordinates determined using the $(T, \dot{\epsilon}_{\min}, \sigma, f(\text{MP}))$ model with the respective experimental creep testing and material conditions as input variables. This approach was adopted to enable the easiest graphical comparison of experimental observation with model prediction.

3.2.3 Material Pedigree Functions

The new feature of the stress-modified ductility exhaustion model defined by eqn.3.11 and eqn.3.12 is the introduction of a material pedigree function, $f(\text{MP})$. This function is composed of a series of individual $f(\text{mp})$ functions covering a spectrum of chemical composition and heat treatment parameters derived from the results of an extensive literature review.

Reference papers were found covering the influence of major material parameters (i.e.: one chemical element content or one heat treatment variable) by mean of laboratory creep tests. The influence of such material parameters was hence plotted on graphs reproducing the normalized creep rupture ductility change as a function of material parameter value ($Z_u=f(\text{mp})$), obtaining then, interpolating the data through least squares linear regression, an equation (namely the material parameter function) representative of the material parameter. Later on in this chapter, the analyses performed with respect to each material parameter is briefly discussed and, although the representative graphs are not included, a final table summarizing the representative influence of each single material parameter on the 1CrMoV creep rupture ductility (Table3.12).

In cases where individual parameters cannot be treated in isolation because of known interrelation effects, either individual functions are combined in an appropriate way, or the effects of the parameter are contained within the functions for other parameters.

The individual material pedigree functions relating to chemical composition and heat treatment temperatures are tabulated in Table3.12. The table lists for each parameter: the individual $f(\text{mp})$ function, the parameter range covered by the literature surveyed, the parameter range over which the $f(\text{mp})$ function is established, and the application range of the $f(\text{mp})$ function for 1CrMoV steel.

The way in which the individual functions are combined to form the $f(\text{MP})$ function is given in paragraph 3.2.4. The basis for the individual functions is reviewed in the following sections covering the influence of the chemical composition and the heat treatment process on the creep properties of the 1CrMoV rotor steel.

The characterisation of the melting practice and its influence on the creep properties of the 1CrMoV rotor steel, although important for the control it exerts on inclusions' characteristics which in turn control the upper shelf creep rupture ductility, are not objective of the present model, since research on the influence of melting practice on creep ductility was insufficient to allow a quantitative characterization. Anyway the effects of common melting practices may

be indirectly identifiable throughout the analyses of fundamental material pedigree parameters which have been instead investigated.

3.2.3.1 Chemical Composition

The $f(\text{MP})$ function in the creep rupture ductility model includes individual terms covering the effects of a number of different elements. The constants in the individual chemical element functions defined in Table3.12 have been determined by linear regression of published observations and subsequent normalisation with respect to the mean reference compositions defined in Table3.8.

Table3.8: Alloy Mean Reference Values for 1CrMoV (in weight percentage)

C	Mn	Si	P	S	Ni	Cr	Mo	V
0.25	0.725	0.15	0.0075	0.0075	0.60	0.85	0.80	0.33

Al	Cu	As	Sb	Sn	Ce
0.005	0.075	0.0125	0.0025	0.0075	0

Carbon [C]

While carbon is a potent solid solution strengthening element, its main contribution to the creep properties of 1CrMoV is through the formation of a fine dispersion of vanadium carbide precipitate during tempering heat treatment [10]. In this respect, the element has a greater influence on creep strength than ductility.

In former times, it was believed that creep cavities formed primarily at carbide particles on prior austenite grain boundaries as a consequence of grain boundary sliding, but it is now known that cavity nucleation in low alloy steels also occurs at incoherent sulphide particles also residing on the grain boundaries [15]. Chen et al. [16] concluded that there was no correlation between C concentration and creep rupture ductility, that the main element responsible for cavity nucleation at grain boundaries was sulphur (S), and that the effectiveness of the element in this role was influenced by manganese (Mn), silicon (Si) and phosphorus (P) concentrations. Interestingly, George et al. [24] reported a beneficial effect of very small concentrations of C on the rupture ductility of relatively pure iron, observing a similar behaviour to that of P in its tendency to compete with S to occupy grain boundary cavity nucleation sites.

The $f(\text{MP})$ function in the present creep rupture ductility model is not directly dependent on C (see paragraph 3.2.4), although its influence is inherently covered by the effects of the carbide forming elements and the heat treatment conditions responsible for their formation.

Manganese [Mn]

Mn (like cerium) is a strong sulphide former and can minimise sulphide dissolution during austenitisation and the subsequent re-precipitation on grain boundaries ultimately responsible for creep cavity formation [25] and [26]. In this way, increasing Mn is responsible for improving rupture ductility or maintaining it at a high level. An observed decrease in creep strength resulting from increasing Mn content from 0.03 to 0.71%, is attributed to the

consequential increase in stacking fault energy and enhanced dislocation mobility leading to the possibility of easier cross slip [37].

The present creep rupture ductility model is provided for Mn contents ranging from 0 to 0.76%. $f(\text{Mn})$ applies as a variable within the range $0 < \text{Mn} < 0.56\%$, but is constant for higher values of Mn (at least up to 0.76% [25] and [26]).

The influence of Mn on creep rupture ductility complements that associated with P and Si, because doping a steel with one of these three elements has no additional effect if the other two are already present in sufficient quantities.

Silicon [Si]

Wilkinson et al. [66] observed a beneficial effect of the addition of Mn, Si and/or P on the creep rupture ductility at 500°C of high purity 2¼CrMo steel at 500°C. Si does not appear to modify the creep properties if added to a steel which already contains significant Mn and P since the rupture ductility is already high. Steels doped with Mn + Si + P or with Si + P exhibit higher rupture ductilities than those steels simply doped with Mn or P, both variants of this alloy being more creep ductile than high purity steels.

The evidence that the effect of Si on the rupture ductility of low alloy bainitic steels is complementary to that of Mn and P is concluded from the results of a number of investigations. The rupture ductility of 2¼CrMo at 550°C is significantly improved by increasing Si from 0.12 to 0.32% [43]. Although Si may considerably improve ductility, it appears to have little effect on creep strength [66].

Middleton [42] confirmed the apparent relationship between Si and other sulphur-stabilizing elements by observing that Si added to Mn-free ½Cr½Mo¼V steel leads to an increase in rupture elongation from 1.5 to 6%, whereas Si added to ½Cr½Mo¼V containing 0.57%Mn does not increase the rupture ductility at all (in this case, the rupture elongation was already high, being 18%).

Phosphorous [P]

The effect of P on cavity formation is complex. P weakens the interface between particles and the matrix, enhancing cavity nucleation [66], but also lowers the grain boundary self diffusion coefficient and thereby the cavity growth rate. Increasing P leads to higher rupture ductility because it competes with S for site occupancy at the grain boundaries [16].

The phenomenon of grain boundary site occupancy is a kinematic (non-equilibrium) effect. Increasing the austenitising temperature reduces the rupture ductility because the diffusivity of S exponentially increases with temperature and the element becomes dominant with respect to P in occupying grain boundary sites. Fattorini [22] observed that P segregation to the grain boundaries is very fast (also at creep temperatures), and the presence of P can affect cavity nucleation by lowering the surface energy and hence the critical radius ($r_c = 2\gamma/\sigma$) above which cavities becomes stable. Needham & Orr [43] observed that the simultaneous addition of S and P to a 2¼CrMo steel leads to no substantial variation of creep properties at 550°C.

Additions of Mn, P and Si appear to influence rupture ductility in low alloy bainitic steels in a complementary way. For this reason, the respective individual material $f(\text{mp})$ functions for the three elements are combined as follows:

eqn.3.14

If $[f(\text{Mn})] + [f(\text{P})] + [f(\text{Si})] < -1$ then $f(\text{Mn,P,Si}) = [f(\text{Mn})] + [f(\text{P})] + [f(\text{Si})]$

else $f(\text{Mn,P,Si}) = 0$

Sulphur [S]

Creep rupture tests performed on iron at temperatures between 500°C and 800°C have shown that S concentrations greater than 20ppm are responsible for low ductility intergranular fracture [26]. At temperatures lower than 600°C, S has solubility in iron of about 10 ppm [26] and [9], and concentrations exceeding this solubility limit lead to precipitation. Sulphur precipitates weaken the interface between matrix and particles, leading to decohesion and cavitation, and low ductility intergranular rupture.

At 500°C, Z_u decreases with increasing S concentration.

At 700°C, Z_u is at a minimum for intermediate S concentrations of ~40ppm (compare with a solubility limit of ~30ppm) because increasing S leads to further coarsening of sulphur bearing precipitates which are less harmful with respect to matrix-particle decohesion and cavitation.

Myers et al. [41] demonstrated that, while cavities tended always to form at grain boundary sulphide particles in 1Cr½Mo steels, these were not the only nucleation sites. Cavities also nucleated at Fe₃C, Mo₂C and other precipitate particles.

It is said that sulphides can dissolve to provide S to coat the free surfaces created by cavity formation, making it possible for a fine sulphide to nucleate a cavity, but then dissolve at 500°C as the cavity grows, making it impossible to identify the cavity nucleation promoter [16].

While S can have a significant influence on rupture ductility, it is concluded that its effect on creep strength is minimal [55].

Mainly based on the work of George et al. [26], the $f(S)$ function given in Table 3.12 has been obtained from fitting data at 500°C and 600°C.

Nickel [Ni]

Ni concentrations in excess of 1.0% are responsible for a decrease in creep strength [37], the effect being due to the consequential increase in stacking fault energy and enhanced dislocation mobility leading to the possibility of easier cross slip.

An individual material pedigree function for Ni is not proposed for the present rupture ductility model.

Chromium [Cr]

Increasing the Cr content produces changes in matrix precipitation characteristics, with Cr₇C₃ or Cr₂₃C₆ replacing V₄C₃ and thereby reducing the creep strength of the steel [37] and [60]. For example, increasing Cr from 2.25 to 3.25% can be responsible for halving the density of V₄C₃ strengthening precipitates. Cr can chemically stabilise the grain-boundary sulphide dispersion in ferrite by progressively substituting for Mn (in MnS), thereby also increasing particle/matrix cohesion [15].

Cr reduces the creep strength of the matrix (and eventually increases that of the grain boundaries) with the effect of shifting damage development from the grain boundaries to matrix/particle locations within the grains, and ultimately increasing rupture ductility.

Molybdenum [Mo]

Mo influences creep strength in two ways. Firstly, it is an important solid solution strengthening element. However in CrMoV steels, increasing Mo has a detrimental effect on

creep strength because it reduces the density of V_4C_3 precipitates through the preferential formation of Mo_2C and Mo_6C . Kadoya et al. [37] observed that Mo in concentrations below 1.0% does not have a significant influence on creep strength, because of the dominating contribution to matrix strengthening, but with the optimum concentration for creep strength being ~0.7%. A Mo concentration above 1.5% offers no further matrix strengthening advantage, but has an increasingly significant influence on the density of V_4C_3 precipitate density. The effect is however not comparable to that produced by Cr in terms of magnitude of creep strength reduction. This applies for $0 < Mo < 1.8\%$.

An individual material pedigree function for Mo is not proposed for the present rupture ductility model.

Vanadium [V]

Vanadium has a major influence on the creep properties of CrMoV steels due to the precipitation of an intense distribution of fine V_4C_3 particles during tempering heat treatment. Fine V_4C_3 nano-particles are responsible for the control of dislocation free paths and highly influential in the determination of creep properties. More intense V_4C_3 precipitation leads to higher creep strength, also by reducing the formation of Fe_3C [60]. The interaction of dissolved V with dislocations is also said to influence creep deformation [10].

Increasing the V content up to the stoichiometric level of $V:C = 5.66$ is responsible for a reduction in rupture ductility. Fe_3C is completely eliminated when the stoichiometric ratio is satisfied. Once exceeded, V_4C_3 precipitation becomes less intense and coarser, and for larger V contents the creep rupture ductility recovers to relatively high values.

The effect of V on creep rupture properties is complementary to the effect of the hardening treatment (see 3.2.3.2). Hence, the proposed creep rupture ductility model is dependent only on the most influential of these two parameters in terms of their magnitude, i.e.

eqn.3.15

$$f(H, V) = \min[f(H), f(V)]$$

Aluminium [Al]

Ratliff & Brown [53] quantified the influence of Al on the creep rupture ductility for CrMoV steel at ~525°C and observed a transition from high to low creep rupture ductility for contents of soluble Al in the range 0.012 to 0.017%. For Al below 0.012%, creep rupture ductility is high, whereas for Al larger than 0.017%, creep rupture ductility is low. Viswanathan & Beck [65] observed that high soluble Al contents resulted in a hardening reaction which impairs rupture ductility. The strengthening mechanism may be in terms of the precipitation of larger amounts of MC type carbides and retardation of the formation of $M_{23}C_6$ type carbides in the steels containing Al. Starting with the assumption that CrMoV steels derive their creep and rupture strengths principally from MC type carbides, Viswanathan & Beck postulated that increased precipitation of fine MC results in increased strength at the expense of ductility. Hence it appears that Al affects rupture properties not by segregating to grain boundaries but by strengthening the matrix under creep conditions. In fact it had been unsuccessfully attempted to demonstrate whether Al induces weakening by grain boundary segregation, since it was impossible to produce cold, brittle fracture at grain boundaries (whereas it is possible for CrMoV steels doped with P, Sb, Sn, As) and this was considered proof that Al does not segregate at grain boundaries. The proposed $f(Al)$ function does not apply to 1CrMoVTiB, since the influence of Al on the properties of this steel is known to be quite different to that of 1CrMoV steel [43].

Copper [Cu]

Benes & Skvor [8] observed the highest creep strength and lowest rupture ductility corresponding to a copper content of 0.2% in a $\frac{1}{2}\text{Cr}\frac{1}{2}\text{Mo}\frac{1}{4}\text{V}$ steel. Most of their results were very much conditioned by variations of other alloying elements (in particular Si and S). However, a comparison of the properties of heats with similar S and Sn concentrations and equivalent Si and P contents led to the development of a $f(\text{Cu})$ function based on Cu in the range 0 to 0.36%.

Arsenic [As]

Needham & Orr [43] observed no substantial influence of increasing As content from 0.003 to 0.063% on the rupture ductility of $2\frac{1}{4}\text{CrMo}$ steel at 550°C. Similarly, Roan & Seth [55] observed that increasing the As content in a $1\text{Cr}1\text{Mo}\frac{1}{4}\text{V}$ steel had no effect on either rupture life or secondary creep rate. Consequently, there is no $f(\text{As})$ function for the proposed ductility model.

Antimony [Sb]

Increasing Sb from 0.001 to 0.021% can be responsible for a significant reduction in the rupture ductility of $2\frac{1}{4}\text{CrMo}$ at 550°C [43]. Similar evidence is available for CrMoV [22] and [56]. There appears to be little influence of Sb on creep properties [22] and [55].

Tin [Sn]

The influence of Sn on creep rupture properties is strongly dependent on the presence of other residual elements [63] and [64]. Hence, there is no $f(\text{Sn})$ function for the proposed ductility model.

Titanium [Ti]

The influence of Ti on creep properties is complex since the presence of other impurities has a strong impact on its effect. Nevertheless, as a generality, rupture ductility is enhanced by the presence of Ti, independently of the presence of B, Sn, Sb and P [64]. In $1\text{Cr}1\text{Mo}\frac{3}{4}\text{V}$ steel, the addition of Ti leads to a marked improvement in rupture ductility, which is further enhanced when the addition of Ti is made in combination with B [60]. In both cases the creep strength is not affected. Ti de-oxidation is preferred to Al de-oxidation practice to maximise rupture ductility in $\frac{1}{2}\text{Cr}\frac{1}{2}\text{Mo}\frac{1}{4}\text{V}$ steels [7].

Cerium [Ce]

Recognizing the impact of sulphides as cavity nucleation sites, George et al. [25] and [26] showed that ductility can be kept high either by reducing S or through the addition of Ce. Cerium is a strong sulphide former and the temperature at which CeS dissolves and goes into solution is higher than for most sulphides. Consequently, S may not diffuse during the heat treatment process and does not precipitate on grain boundaries. Middleton [42] observed a strong increase in rupture elongation (to 20.5%) as a consequence of increasing the Ce content from 0.017% to 0.06%. Norton & Strang [44] observed that increasing the Ce content from 0 to 0.105% only influences the creep rupture ductility and not the creep strength of 1CrMoV steel.

3.2.3.2 Heat Treatment

The heat treatment conditions applied to 1CrMoV have an important influence on the ultimate creep properties of the steel. Typically, a 2 stage procedure is adopted involving a hardening (austenitising) treatment and a tempering treatment. In the hardening treatment, the steel is taken to a temperature (in the range 950-1050°C) and soaked for sufficient time to ensure that most carbide particles have been taken into solution in the austenite phase, but insufficient time to avoid excessive grain growth. The steel is then quenched at a rate normally to give a mid-to-upper bainite microstructure. This procedure is referred to as the hardening treatment because the quenched transformation product (in this case bainite) is much harder than the equilibrium microstructure of ferrite and carbide which would be realised during slow cooling. The tempering treatment involves (for this steel) heating to a temperature of ~700°C for sufficient time to allow precipitation of an appropriate distribution of the fine V_4C_3 nano-particles which determine the strength and creep property characteristics of the material.

The $f(MP)$ function in the creep rupture ductility model includes individual terms covering the effects of the hardening and tempering temperatures. The constants in the $f(H)$ and $f(T)$ functions defined in Table3.12 have been determined by linear regression of published observations and subsequent normalisation with respect to the mean reference temperatures defined in Table3.9.

Table3.9: Heat Treatment Temperature Reference Values for 1CrMoV

Hardening	Tempering
967.5°C	700°C

Hardening treatment

Increasing the heat treatment austenitizing temperature from 950 to 1050°C is responsible for a reduction of creep rupture ductility [60]. This increase in temperature not only leads to an increase in the austenite grain size, but also the more effective dissolution of carbide particles. The reduction in ductility is therefore partly due to the reduction in grain surface area available for strain accommodation during grain boundary sliding as a consequence of the increasing grain size. In addition, subsequent precipitation of V_4C_3 particles is finer and more intense the greater the degree of super-saturation of V and C during the austenitisation treatment. A finer and more intense V_4C_3 precipitate distribution is responsible for more effective matrix hardening and narrower precipitate denudated zones adjacent to grain boundaries, both developments promoting low ductility intergranular rupture. At high austenitising temperature sulphides may dissolve and re-precipitate on grain boundaries, a development also leading ultimately to the formation of cavities [25] and [26].

The austenitizing temperature to be considered for the accounting of $f(H)$ in case of multistep temperature austenitisation treatments is the last executed austenitizing temperature.

The effect of the austenitizing temperature on the creep rupture properties is complementary to the effect of Vanadium content, and hence the $f(MP)$ function is affected only by the most influential of the two parameters in terms of magnitude (see eqn.3.15).

Tempering treatment

The effect of tempering temperature and time on strength and ductility may be correlated in terms of the Hollomon and Jaffe P_{HJ} parameter [35]. While P_{HJ} (Table3.12) has been found to vary linearly with creep strength over a wide range of tempering times and temperatures, no equivalent evidence relating to rupture ductility was located. The expression given in Table3.12 is based on limited evidence assessed from the dataset available for this investigation [13], [34] and [45].

3.2.4 Model Effectiveness

The effectiveness of the ductility model was examined using a creep property (and associated material pedigree) dataset comprising 88 test results covering 10 heats of 1CrMoV steel [13], [34] and [45]. Creep rupture ductilities were calculated through eqn.3.11 and eqn.3.12 with $f(\text{MP})$ being determined by summing the individual material pedigree functions defined in Table3.12 in accordance with eqn.3.16, i.e.

eqn.3.16

$$f(\text{MP}) = f(\text{H, V}) + f(\text{T}) + f(\text{Cr}) + f(\text{Mn, P, Si}) + f(\text{Al}) + f(\text{Ce}) + f(\text{Cu}) + f(\text{S}) + f(\text{Sb}) + f(\text{Ti}) + 1$$

The $f(\text{MP})$ values determined for a number of individual heats of 1CrMoV [13], [34] and [45] are summarised in Table3.10.

Table3.10: Summary of $f(\text{MP})$ Values for Individual Heats of 1CrMoV

Heat	Heat 1 [13], [34]	VaA [45]	VaB [45]	VaC [45]	VaD [45]	VaE [45]	VaG [45]	VaH [45]	VaJ [45]	VaR [45]
$f(\text{MP})$	0.95	0.74	0.79	0.91	0.67	0.72	1.44	1.22	1.28	1.01

The $f(\text{MP})$ function was designed in a way to match unity in the case of material pedigree coincident with Table3.8 and Table3.9.

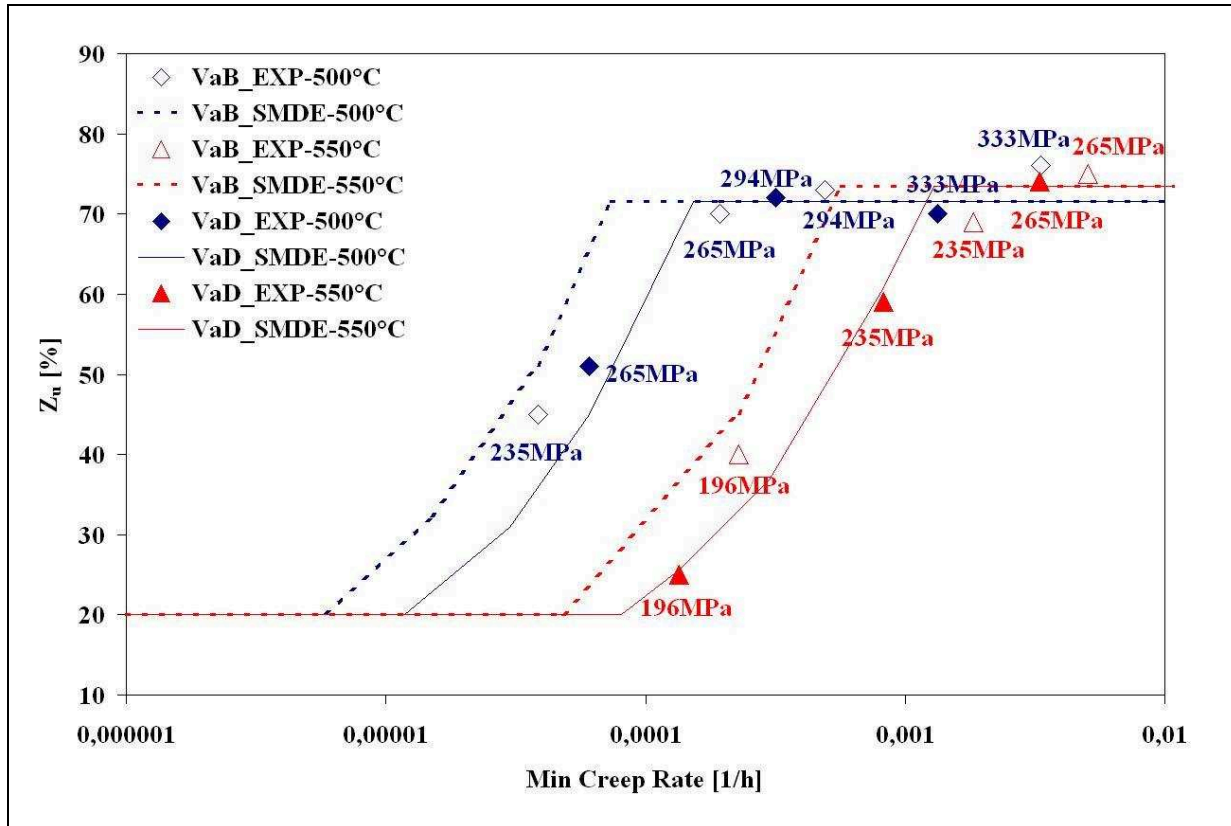


Fig.3.11: $Z_u(\dot{\epsilon}_{\min})$ diagram for Heat VaB and VaD (NRIM [45]), representative of the influence of different material pedigrees on the measured creep rupture properties (*lines represent model predictions*)

The effectiveness of the creep rupture ductility model to fit the observed $Z_u(\dot{\epsilon})$ behaviour for different heats of 1CrMoV (i.e. Heat 1 [13] and [34] and VaB and VaD [45]) is demonstrated in Fig.3.10 and Fig.3.11.

In addition to that, Fig.3.11 highlights the relevance of accounting for the effect of the material pedigree in the SMDE model: in fact the 1CrMoV heats VaB and VaD, which are characterised by different material pedigrees, exhibit completely different creep rupture properties (in terms of min creep rate and creep rupture ductility) when subject to the same creep loading conditions, namely stress and temperature (e.g.: observe the different material response at 500°C and 265MPa).

The capability of the new model to predict the rupture ductilities of 10 different heats of 1CrMoV steel is shown in Fig.3.12.

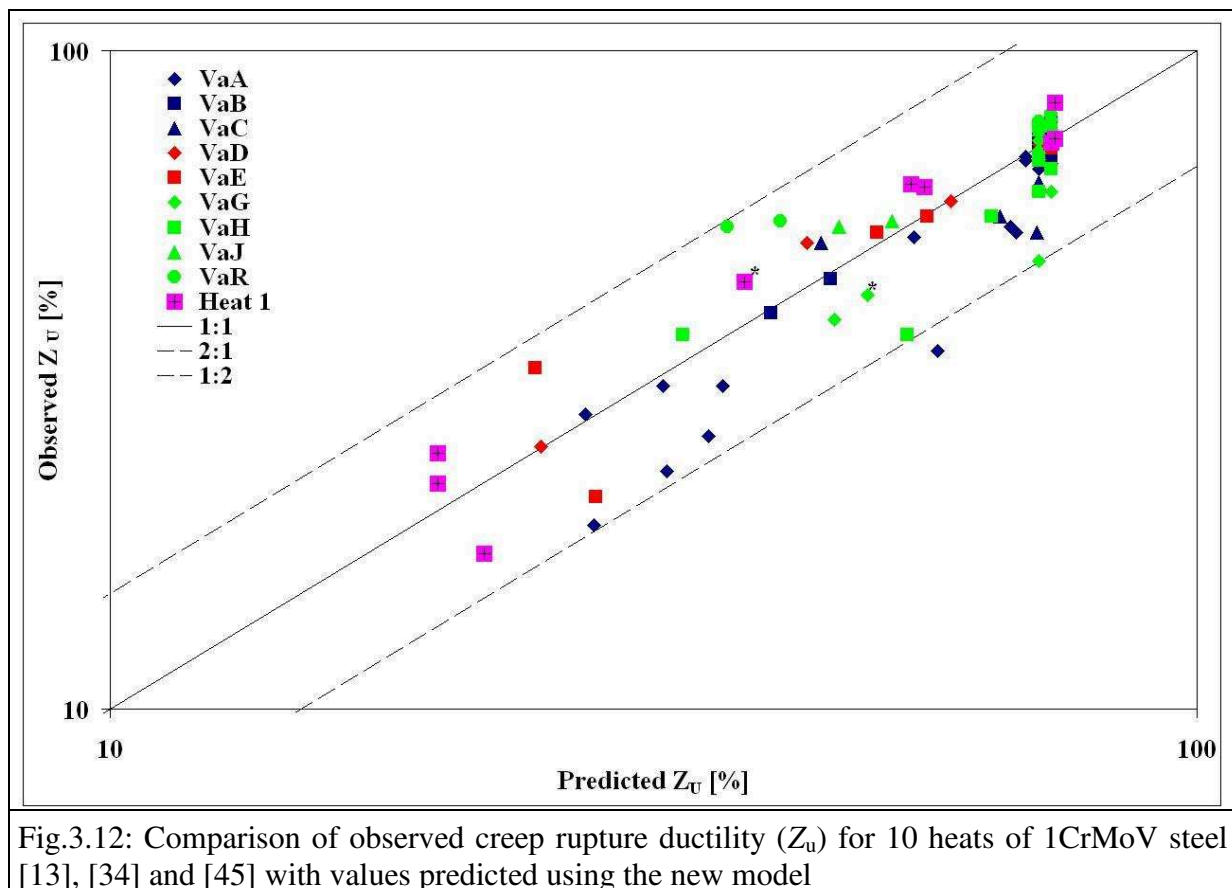


Table3.11 shows the statistical improvement (restricting the statistical analyses to the transition regime only) obtained by implementing the $f(\text{MP})$ material pedigree function in the creep rupture ductility model.

The established dependence on material pedigree parameters provides a basis for the determination of ductility scatterband minima and maxima for the specified alloy.

Table3.11: Summary of statistical results related to the transition regime only

Model	Variance	Standard Error
Without $f(\text{MP})$ function	0.107	0.327
With $f(\text{MP})$ function	0.049	0.221
Improvement*	54%	32%

(*) Variance and Standard error are reduced by 54% and 32% respectively, according to the new SMDE model.

3.2.5 Discussion

Variability of results is reduced by adopting the new creep ductility model with respect to results from the standard stress-modified ductility exhaustion approach (although the improvement may be barely distinguishable out of the graphical test of Fig.3.12, the statistical results in Table3.11 are surely more convincing).

Nevertheless the overall scatter remains high. This aspect is for sure due to laboratory-to-laboratory variability: the SMDE model here proposed is, in fact, determined by material parameters' functions obtained from analyses of different laboratories' results. Furthermore, the high scatter may be also due to creep damage and deformation inner scatter. In fact, experiments have provided evidence of different creep responses to identical creep testing conditions applied to namely identical material pedigrees (i.e.: testpieces were obtained from the same part of the same heat and machining was executed with respect to testpiece axis orientation relative to the forged rotor). Proof of this is given by testpieces HT12 and HT85, both obtained from the same manufacturing process and tested under identical loading conditions (at 565°C and 308MPa), which showed important differences in terms of creep properties as reported in Table3.1.

Hence it is evident that the creep rupture ductility model here proposed is not intended to be an instrument able to predict creep ductilities with absolute accuracy. Indeed the achieved scope of this research was to implement this model in order to minimize the error occurring in the creep ductility prediction.

3.2.6 The Creep Ductility model and the creep damage mechanisms

The creep rupture ductility model could also be employed to qualitatively predict the form of creep damage which characterises the crept material. The model predicts progressively larger creep rupture ductility and creep strain rate as a consequence of the higher applied stress (at 550°C). Fig.3.13 shows the good consistency between the predicted creep rupture ductility and the progressive creep damage change from intergranular (in the form of cavities coalesced at grain boundaries) to transgranular (in the form of matrix-particle decohesion) creep damage, consequence of progressively higher applied stresses.

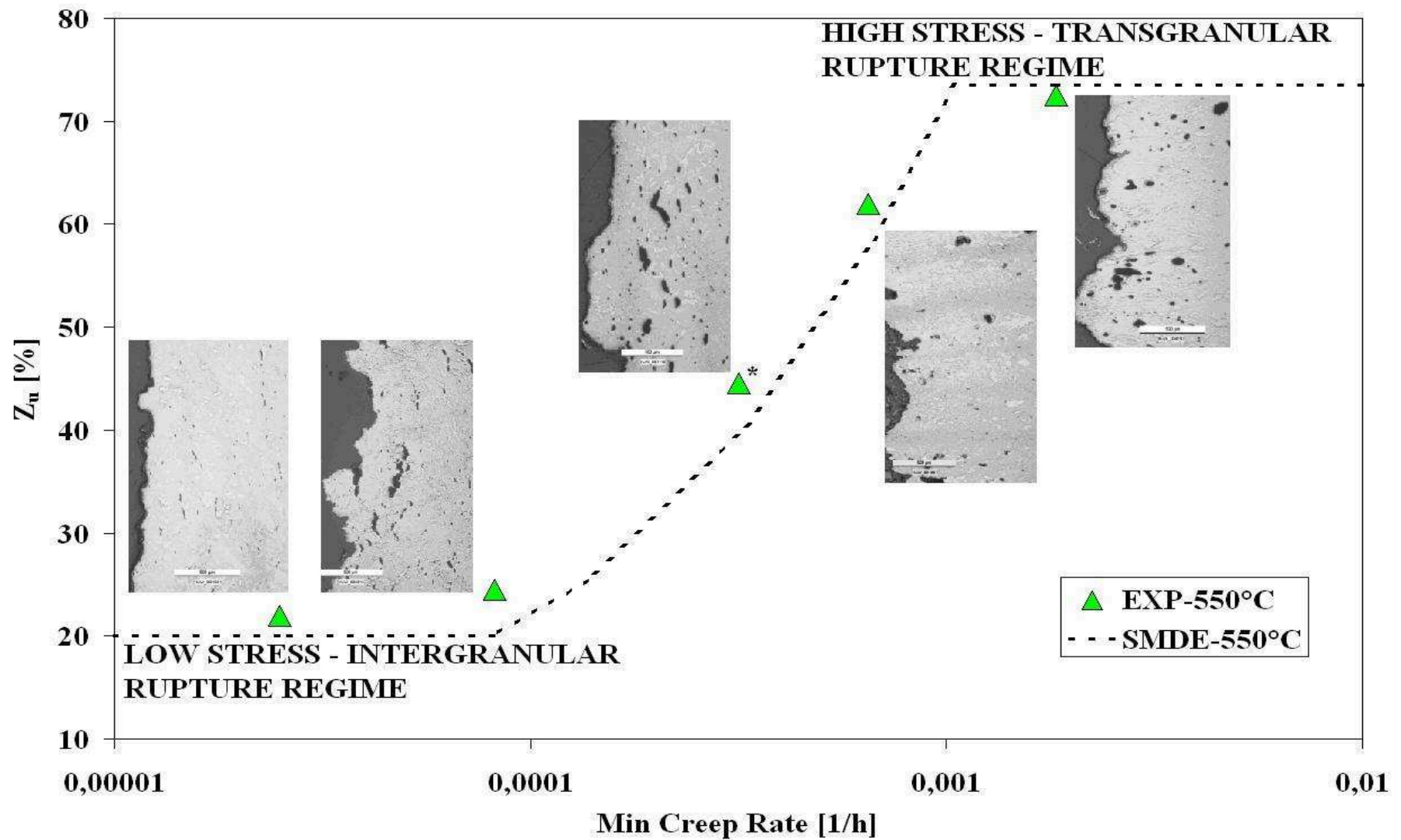


Fig.3.13: The consistency between the creep rupture ductility model and the observed creep damage mechanisms.

The creep damage pictures schematically shown in Fig.3.13 are more clearly depicted in Fig.3.14.

Fig.3.14: Influence of the applied stress on creep damage mechanisms

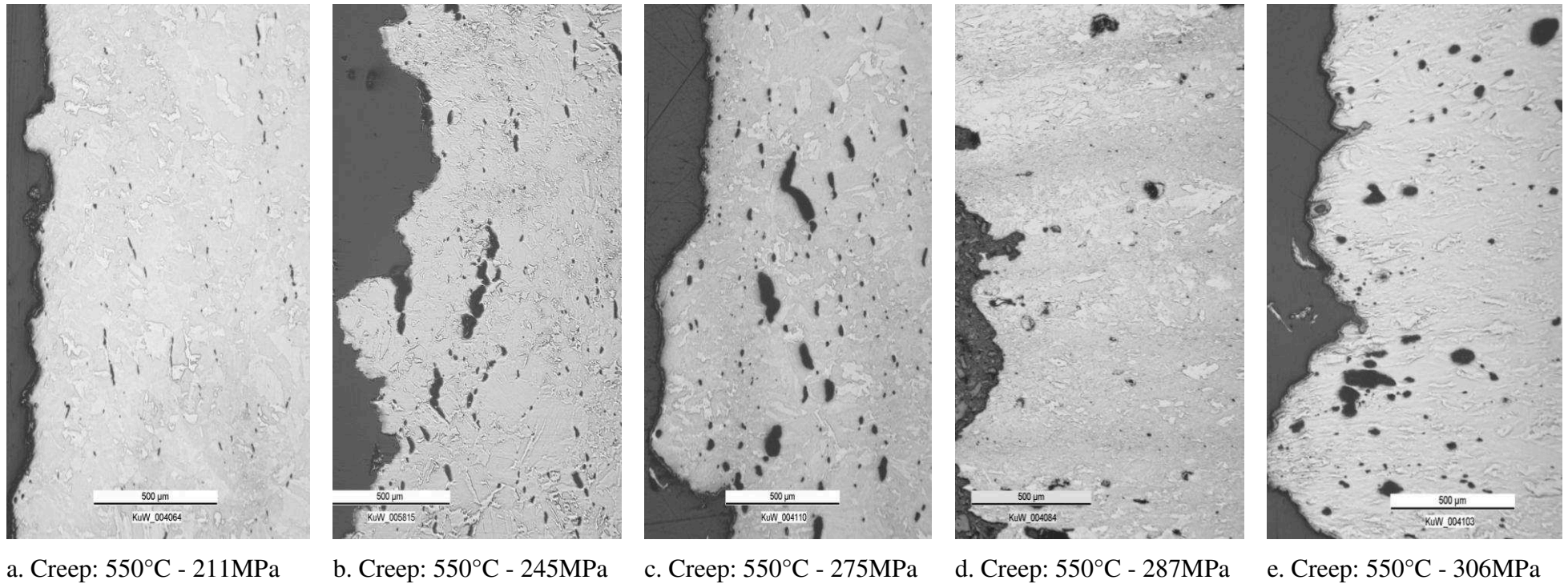


Table3.12: Individual Material Pedigree Functions

Parameter	Individual $f(\text{mp})$ function	Parameter range covered by literature	Parameter range over which $f(\text{mp})$ function established	$f(\text{mp})$ application range for 1CrMoV
Manganese	$f(\text{Mn}) = (0.1615 + 0.979 \cdot [\text{Mn} - 0.725])$ $f(\text{Mn}) = 0$ <i>but see eqn.3.14</i>	$\leq 0.76\%$	$\leq 0.56\%$ $0.56 - 0.85\%$	0.60 - 0.85%
Silicon	$f(\text{Si}) = (3.83 \cdot [\text{Si} - 0.15])$ <i>but see eqn.3.14</i>	$\leq 0.35\%$	$\leq 0.35\%$	$\leq 0.30\%$
Phosphorous	$f(\text{P}) = (45 \cdot [\text{P} - 0.0075] + 3600 \cdot [\text{P} - 0.0075]^2)$ <i>but see eqn.3.14</i>	$\leq 0.025\%$	$\leq 0.018\%$	$\leq 0.015\%$
Sulphur	$f(\text{S}) = -1416.7 \cdot [\text{S} - 0.0075] - 3.54167$	$\leq 0.015\%$	0.001% - 0.005%	$\leq 0.015\%$
Chromium	$f(\text{Cr}) = (1.05 \cdot [\text{Cr} - 0.85] + 0.79 \cdot [\text{Cr} - 0.85]^2)$	$\leq 2.88\%$	$\leq 2.88\%$	0.7 - 1.0%
Vanadium	$f(\text{V}) = (-5.381 \cdot [\text{V} - 0.33] + 7.822 \cdot [\text{V} - 0.33]^2)$ <i>but see eqn.3.15</i>	0.20 - 1.11%	0.20 - 1.11%	0.30 - 0.36%
Aluminium	$f(\text{Al}) = (1.225 - 175 \cdot [\text{Al} - 0.005])$	$\leq 0.03\%$	0.012 - 0.017%	$\leq 0.01\%$
Copper	$f(\text{Cu}) = (-6.43 \cdot [\text{Cu} - 0.075] + 16.4 \cdot [\text{Cu} - 0.075]^2)$	$\leq 0.36\%$	$\leq 0.36\%$	$\leq 0.015\%$
Antimony	$f(\text{Sb}) = -42 \cdot [\text{Sb} - 0.0025]$	$\leq 0.010\%$	0.002 - 0.010%	$\leq 0.005\%$
Cerium	$f(\text{Ce}) = -13.3 \cdot [\text{Ce}] + 2166 \cdot [\text{Ce}]^2$	$\leq 0.105\%$	$\leq 0.060\%$	-
Titanium	$f(\text{Ti}) = -5.8824 \cdot [\text{Ti}]$	$\leq 0.080\%$	0.012 - 0.080%	-
Hardening temperature	$f(\text{H}) = (-0.011 \cdot (T_{\text{H}} - 967.5) + 5.5 \cdot 10^{-5} \cdot (T_{\text{H}} - 967.5)^2)$ <i>but see eqn.3.15</i>	950 - 1050°C	950 - 1050°C	960 - 975°C
Tempering temperature	$f(\text{T}) = (0.006174 \cdot P_{\text{HJ}} - 1.2545)$ with $P_{\text{HJ}} = (T_{\text{T}} + 273.15) \cdot (19.5 + \log(t))/1000$	50 - 700°C	50 - 700°C , 0-100h	690 - 710°C

3.3 Type 316 Stainless Steel

This section describes the creep properties of the Type 316 SS at 550°C. Further information can be found in appendix II.b.iii and in Douglas et al. [19]. The Type 316 Stainless steel was investigated in the same way as 1CrMoV, in order to fully understand the response to fatigue-creep loading conditions for both cyclic softening and cyclic hardening materials. The influence of prior cyclic deformation on subsequent creep properties will be described in chapter 5.

3.3.1 Creep deformation

Creep tests were performed on Type 316 SS at 550°C with stress values of 250MPa and 300MPa. Such loading conditions exceed the yield stress (see TableII.4) and in this respect are considerably higher than those applied to 1CrMoV and presented above. Hence different creep deformation responses are expected.

The high applied stress leads to different proportions of the creep regime components (see Fig.3.15). With respect to time, the primary creep phase disappears with increasing load, the tertiary creep phase reduces also whereas the secondary creep phase increases. With respect to total deformation, the applied load leads to high instantaneous plastic strain and since the tertiary creep phase reduces, most of the creep deformation is accumulated during secondary creep phase.

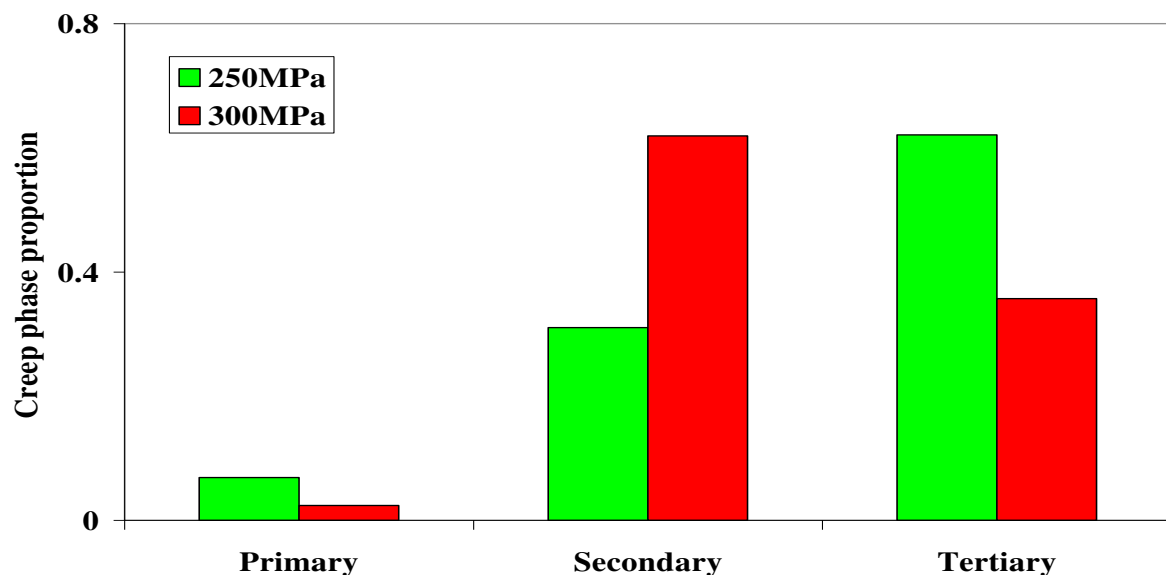


Fig.3.15: Effect of stress on the relative proportions of the regime components in Type 316 SS at 550°C. Creep phases refer to the identification provided and explained through Fig.2.1

Fig.3.16 and Fig.3.17 show the creep curves obtained at 550°C with 250 and 300MPa.

Fig.3.16: Creep curve of Type 316 SS subject to 250MPa creep loading at 550°C

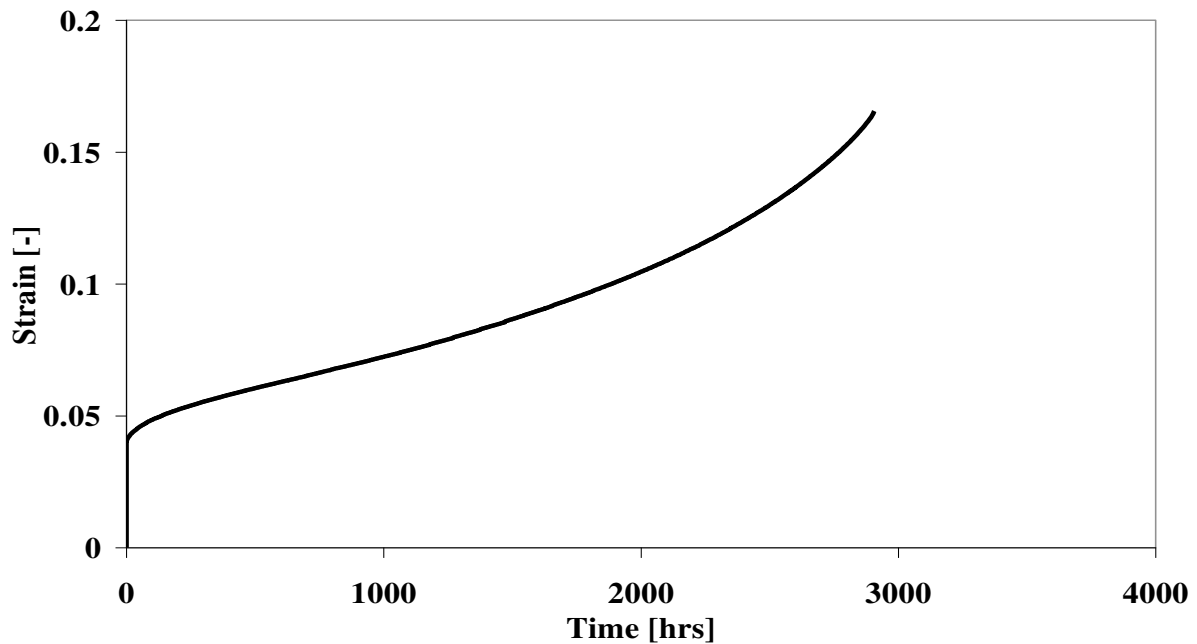
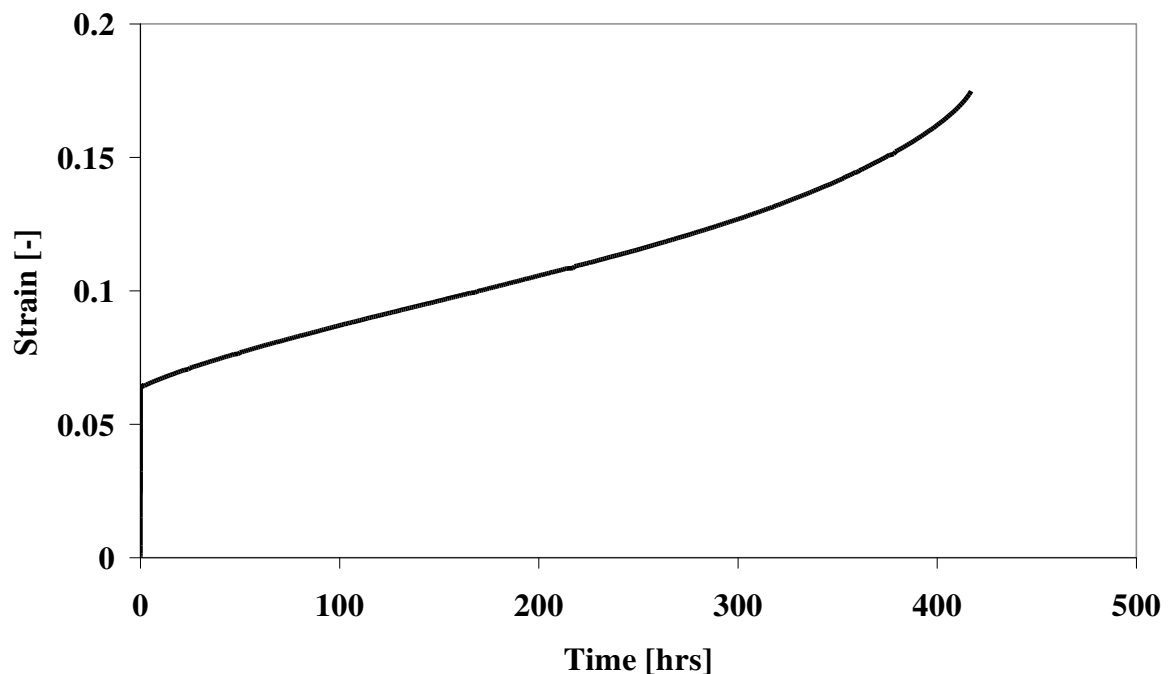


Fig.3.17: Creep curve of Type 316 SS subject to 300MPa creep loading at 550°C



The creep response of the Type 316 stainless steel differs from that of 1CrMoV (see Fig.2.1) for the presence of instantaneous plastic strain and for the accumulation of most of the creep deformation during secondary creep phase (which also increases at larger stress values, as schematically shown in Fig.3.15).

3.4 Concluding Remarks

This chapter analyzed the behaviour of 1CrMoV subjected to static loading conditions at high temperatures. The creep properties were discussed in terms of both creep strength and creep ductility.

The Monkman-Grant equation was defined as a means of predicting the rupture-strength properties of 1CrMoV steel and demonstration of the temperature independency of the relationship was identified as an important outcome of this study.

A stress modified ductility exhaustion model with an added material pedigree function was developed to more effectively predict the creep rupture ductility of 1CrMoV steel. The $f(MP)$ function relies on a knowledge of the influence of individual parameters on the rupture ductility of the steel which in turn are based on observations collated from an exhaustive review of the published literature.

The new creep rupture ductility model has been tested on a 1CrMoV steam turbine rotor steel dataset for 10 different heats containing a total of 88 $Z_u(T, \sigma)$ test observations [13], [34] and [45]. The model is able to considerably reduce the error between observed and predicted creep rupture ductility with respect to a material pedigree independent model (Table 3.11 show that the variance decreases by 54%).

The interesting consistency between the creep rupture ductility model and the observed creep damage condition (and in particular the intergranular/transgranular creep damage proportion) has been also highlighted: indeed, although quantitative creep damage measurements were not executed, the 1CrMoV steel was found to be mostly affected by intergranular creep damage in the form of cavities coalesced at grain boundaries when the predicted ductility was minima. The creep damage was on the other hand completely transgranular in the form of matrix-particle decohesion when the predicted creep rupture ductility was maxima.

The observed creep properties, as well as the results obtained with the MG relationship and the ductility model, will be useful to better understand the results of the research performed in order to assess the influence of prior cyclic deformation on subsequent creep behaviour, which will be presented in chapter 5.

But before moving to chapter 5, the response of 1CrMoV to cyclic loading conditions (LCF) at high temperature will be analysed in chapter 4 to provide the basis for assessing the influence of prior cyclic deformation on subsequent creep properties.

4 CYCLIC DEFORMATION

The objective of this chapter is to consider the response of 1CrMoV to cyclic deformation (LCF) at high temperatures. Since cyclic deformation is responsible for modifications to the microstructure and ultimately to changes in the mechanical properties, the core of this chapter concerns pre and post test inspection through microscopy. The results of this section are of great importance for the present research, as will be clear in the next chapter, where the creep properties of 1CrMoV subjected to prior cyclic deformation will be discussed.

Furthermore, the effectiveness of Miner's rule for fatigue damage calculations is here successfully tested. This will emphasize in chapter 5 the greater importance of improving the way in which creep damage is calculated, since the fatigue damage assessment is proven to be effective.

4.1 Fatigue Tests on 1CrMoV

In order to characterize the response to cyclic deformation of 1CrMoV, fatigue testpieces have been obtained from a heat of 1CrMoV steam turbine rotor material through axial cutting close to the rotor outer surface (see TableI.1 for material pedigree). A campaign of fatigue tests with three constant cyclic deformation strain amplitudes (ϵ_a) was performed according to standard practice [36] and the testing parameters in Table4.1 in order to assess $N_i(\epsilon_a)$.

The strain rate was chosen in a way to avoid creep interaction effects as it was observed through post test inspections of TMF tests specimens in [33].

Test	T [°C]	ϵ_a [%]	$\dot{\epsilon}$ [%/s]
LCF1	565	± 0.25	0.1
LCF2	565	± 0.5	0.1
LCF3	565	± 0.7	0.1
Table4.1: Cyclic deformation testing conditions			

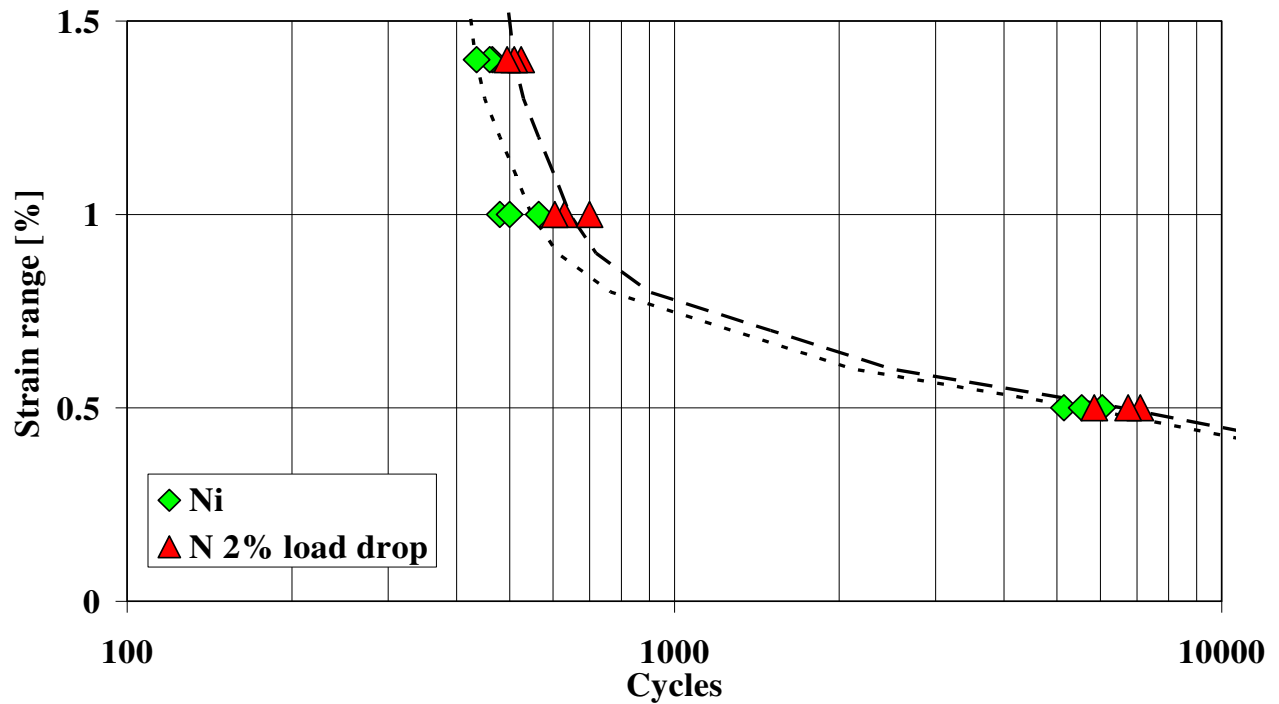


Fig.4.1: Crack initiation resistance of 1CrMoV subjected to cyclic deformation at 565°C expressed as a function of both N_i and $N_{2\%}$.

Table4.2: Crack initiation resistance of 1CrMoV subjected to cyclic deformation at 565°C

	LCF1	LCF2	LCF3
N_i	5583	515	453
$N_{2\% \text{ load drop}}$	6567	645	510

N_i and $N_{2\% \text{ load drop}}$ at 565°C are very similar to those obtained at 550°C (see appendix I), though a noticeable reduction was expected. This could be due to the too small temperature difference (15°C) as well as to a proportional increase of cyclic softening due to the higher temperature which could slow the propagation rate of surface micro-cracks.

As evident from the test results, the cyclic deformation is responsible for a stress-cycle response dominated by monotonic cyclic softening [13]. Also the softening rate was higher for cyclic deformation with larger strain amplitude.

For both strain amplitudes, the softening rate is maximal in the beginning and then it reaches an asymp-

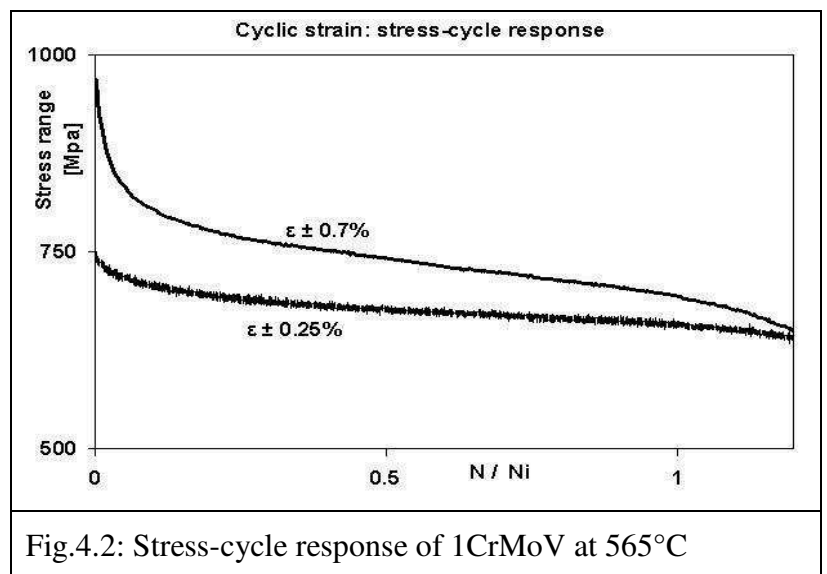


Fig.4.2: Stress-cycle response of 1CrMoV at 565°C

tote of minimum cyclic softening rate corresponding to a stable regime, interrupted at the end by one or more macro-cracks propagating along planes normal to maximum tensile stress and producing net section reduction and a strong load drop.

Research was performed in order to test the hypothesis that microstructural changes are induced by prior cyclic deformation: hence the following sections analyze the influence of cyclic deformation on the microstructure of 1CrMoV in order to understand the reasons for cyclic softening. It will be clear at the end of the present chapter that the mechanical properties (the creep properties in particular) of 1CrMoV change dramatically because of cyclic deformation. Hence the present research will underline the importance of assessing the influence of prior cyclic deformation on subsequent creep properties.

4.2 Post Test Inspection of cyclic deformed 1CrMoV

In order to investigate micro-structural changes produced during cyclic deformation and responsible for cyclic softening, two tests (LCF1-BIS and LCF3-BIS) equivalent to the cyclic deformation histories LCF1 and LCF3 were performed and stopped at $\frac{1}{2}$ Ni (see Table4.3). Such testpieces have been post test investigated together with material in the as received condition in order to assess microstructure evolution, considered to be responsible for cyclic softening. Investigation went then through Vickers hardness tests, grain size measurements, optical microscopy and transmission electron microscopy in order to find a relationship between mechanical properties change and micro-structural change.

Table4.3: Prior cyclic deformation details of post test inspected testpieces

Test	T [°C]	ϵ_a [%]	$\dot{\epsilon}$ [%/s]	Cycles	Test time
LCF1-BIS	565	± 0.25	0.1	2792	7h45'
LCF3-BIS	565	± 0.7	0.1	227	1h46'

4.2.1 Hardness

Hardness values were measured through HV30 tests (according to standard practice [4]) all along the parallel length for as-received material and for material subjected to LCF1-BIS and LCF3-BIS (Table4.4). The hardness was approximately constant along the specimen parallel length, both on the specimen axis and at mid-radius positions between axis and surface (HV values given below are mean values measured within the parallel length).

Table4.4: Hardness measures

	As-received	LCF1-BIS	LCF3-BIS
Vickers Hardness	245	240	221

The grip ends hardness of LCF1-BIS and LCF3-BIS was also measured and found to be 245 HV30, as that of as-received 1CrMoV. This proves that softening in the gauge length is due to cyclic deformation and not at all to thermal transient.

4.2.2 Grain size measurements

Grain sizes of as-received and cyclic deformed 1CrMoV were measured according to standard practice [5]. Prior cyclic deformation is not responsible for prior austenite grain size changes. According to the Hall-Petch relationship ($\sigma_y = \sigma_0 + K_y \cdot 1/\sqrt{d}$, [27] and [47]), the strength is inversely related to the grain size, but grain size measures have not reported any variation (see Table4.5 and Table4.6).

Table4.5: Grain size of as-received 1CrMoV

field	magnification	n°grains	grain size
1	X166	144	35.0
2	X335	72	33.6
3	X335	69	34.6
AVG	-	285	34.5

Table4.6: Grain size of cyclic deformed 1CrMoV according to LCF3-BIS

field	magnification	n°grains	grain size
1	X335	98	30.6
2	X335	85	35.3
3	X335	86	34.9
4	X335	89	33.7
5	X335	94	31.9
6	X335	98	30.6
AVG	-	550	32.7

The grain size is not considered to be the cause of cyclic softening during cyclic deformation.

4.2.3 Dislocation density

The cyclic deformation conditioning performed is so fast that neither re-crystallization nor coarsening of carbide precipitates occurs, so that softening variation should simply depend on dislocation density. Indeed, according to [10] the contributions to strength of steels are as follows:

$$\sigma = \sigma_{Fe} + x_{ss} \cdot \sigma_{ss} + x_c \cdot \sigma_c + K_{gs} \cdot L^{-1} + K_p \cdot \Delta^{-1} + C \cdot \rho_d^{0.5}$$

Where:

σ_{Fe} = strength of Iron

$x_{ss} \cdot \sigma_{ss}$ = solid solution strengthening contribution

$x_c \cdot \sigma_c$ = carbon content strengthening contribution

$K_{gs} \cdot L^{-1}$ = grain size strengthening effect (according to [27] and [47])

$K_p \cdot \Delta^{-1}$ = precipitates strengthening contribution

$C \cdot \rho_d^{0.5}$ = dislocation density strengthening contribution

An experimental dislocation density measurement was not performed, hence the following considerations are based on qualitative transmission electron microscopy and literature review. More in depth, the dislocation density contribution to strength (here, as reflected by the hardness, HV) may be defined by the Bailey-Hirsch relation [6]:

$$HV = 0.7 + 1.5 \cdot G \cdot b \cdot \sqrt{\rho},$$

where the shear modulus $G=80\text{GPa}$ and the Burgers vector $b=0.25\text{nm}$ are typical values for Iron and offer the possibility to predict the dislocations density for the 3 microstructures (as-received, LCF1-BIS and LCF3-BIS) on the basis of respective HV values.

Table4.7: Expected dislocation density values, according to [6]

Pre-conditioning	As-received	LCF1-BIS	LCF3-BIS
HV	245	240	221
Dislocation density [$1/\text{m}^2$]	$3.22 \cdot 10^{15}$	$3.04 \cdot 10^{15}$	$2.39 \cdot 10^{15}$
Dislocation density reduction	-	5.6%	25.8%

4.2.4 The Microstructure of 1CrMoV

One objective of this investigation is to understand and quantify the main causes of cyclic softening in 1CrMoV. Dislocations density change (annihilation and rearrangement from random to ordered distribution) and consequent sub-grain structure formation (i.e.: induced by dislocation movement) are observed to be the main structural changes responsible for mechanical properties variation due to cyclic deformation. In fact the cyclic deformation has been performed in a way to last only a few hours, in order to avoid any micro structural change induced by temperature and creep processes.

Being aware that ferrite / bainite phases are much inhomogeneous and characterized by relatively high dislocation density and high carbide precipitation density, the microscopy analyses of fatigue damaged material has followed a few first sessions working on as-received material (see appendix I) that were mandatory in order to become familiar with its microstructure.

4.2.4.1 Dislocation annihilation and rearrangement

In as-received material dislocations are disordered with relatively uniform density and look as tangles with no favorite orientation (forest of dislocations), as shown in Fig.4.3.

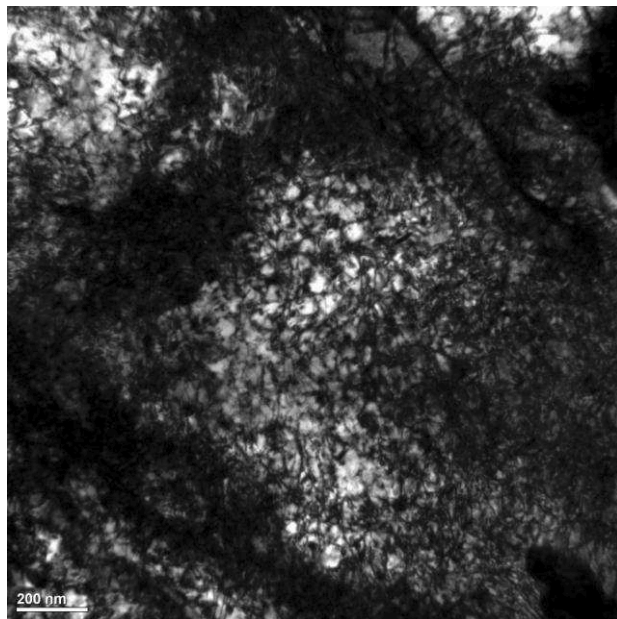


Fig.4.3: As-received 1CrMoV

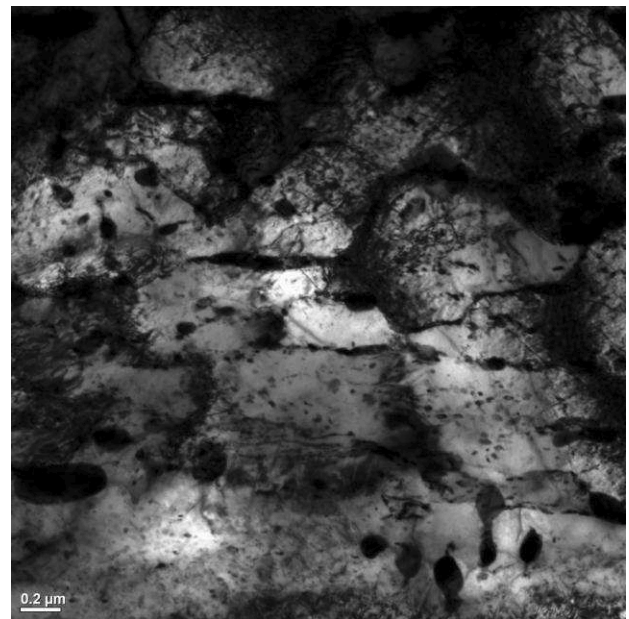


Fig.4.4: 1CrMoV after cyclic deformation according to LCF3-BIS

A first look at 1CrMoV after cyclic deformation indicates a much lower dislocation density, as expected to be after dislocations annihilation (compare Fig.4.3 with Fig.4.4). This would confirm the values expected as shown in Table4.7, ultimately being the reason for cyclic softening. A deeper investigation shows however that overall dislocation density may be lower because of annihilation, but more probably because dislocation density is not as uniform as for virgin material anymore: in material subjected to cyclic deformation dislocations are rearranged to form a sub-grain structure (see also paragraph 4.2.4.2) with boundaries well defined by high density of parallel dislocation lines. Dislocations density is much lower within the sub-grains. Here the few existing dislocations appear to be much more ordered and following two main perpendicular directions. The overall dislocation density appears to be much lower because of their displacement and pile up towards sub-grain boundaries producing arrays of dislocations (due to strain cycling).

Characterizing the dislocations pile-ups is difficult because they are quite often arranged on a plane which is not parallel to the foil specimen, hence producing overlapping of dislocations: This is a major problem in quantifying dislocation condition in order to assess the density. A sequence of thick dark lines (10nm) with constant inter-distance of about 20nm is considered to be an array of dislocations (a pile-up of dislocations) lying on the foils plane (The burgers vector in Iron is

0.25nm, whereas the thickness of dark lines identifying dislocations depends on the crystal distortion produced by the presence of the dislocation itself). Pile-ups with a less thick dark line (1nm or less) with constant mutual distance between dislocations of about 5nm have also been observed and considered as lying almost perpendicularly to the foils plane (see Fig.4.5). In other words the reciprocal dislocation distance in pile-up formations (i.e.: circa 20nm) is here adopted as a mean to establish the dislocations pile up orientation with respect to the foil plane. This is permitted, being such inter-distance theoretically constant, being the minimum energy position found to reach equilibrium between crystals bonding energy (stacking fault energy) and a dislocation repulsive energy (after annihilation, close dislocations create reciprocal interference and repulsion because of a coincident stress strain field).

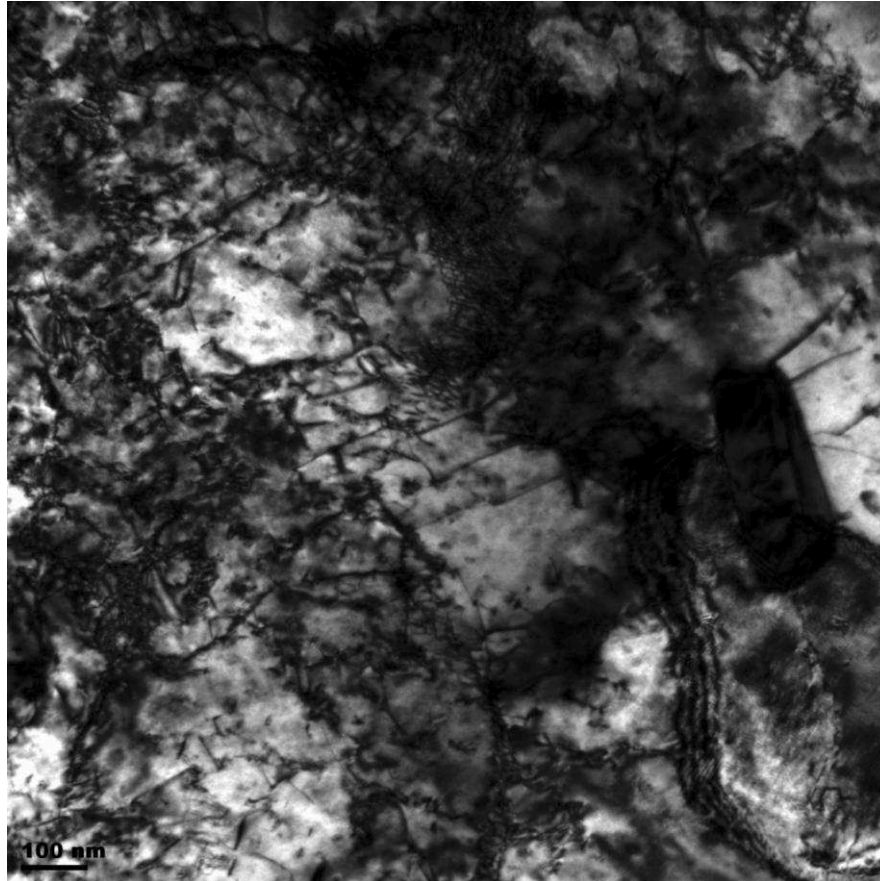


Fig.4.5: 1CrMoV after cyclic deformation according to LCF3-BIS

In a few circumstances, dislocations are arranged in similar form (pile-ups) in as-received material also. This however happens only close to large M_3C precipitates where the material can more easily stretch itself (e.g. to relax residual stresses) producing such dislocation features. Indeed M_3C rich areas are softer, being richer in Cr and denuded of V-C precipitates in accordance to the strengthening effect of V-C precipitates and the opposite effect of Cr-C precipitates explained by [44] and covered in appendix I.

4.2.4.2 Sub-grain (or sub-cell) structure formation

In as-received material the dislocation density is more uniform compared to that of material subjected to cyclic deformation. Sub-grain structure is present, though very much isolated, so that size measurement can not rely on standard guidelines offered for continuous sub-grain structure, whereas it must be locally performed. However sub-grains have globular shape and are surrounded by arrays (pile-ups) of dislocations. Sub-grains measurements exhibit a size of $1.02\ \mu\text{m}$ (and standard deviation of $0.28\ \mu\text{m}$).

As a direct consequence of cyclic deformation, dislocations move in search of a minimum energy position resulting in annihilation and pile up, ultimately modifying the material structure to a less-uniform dislocation density condition, where the sub-grains structure is more evident. Sub-grains in fatigue damaged material according to LCF3-BIS have size in the order of $0.74\ \mu\text{m}$ (and standard deviation of $0.28\ \mu\text{m}$, again).

Assuming that dislocations annihilation does not occur, the strength is expected to vary as a consequence of sub-grain structure formation (i.e.: formation of areas with different dislocation density). In particular the strength of sub-grains (relatively dislocation free areas) is expected to be lower than the uniform strength of virgin material.

Sub-grain size and sub-grain boundary thickness are expected to depend on cyclic deformation strain amplitude [48]. In particular it is expected to have thicker sub-grain boundaries (pile-ups) with increasing cyclic deformation strain amplitude. Grain size is expected to increase with decreasing cyclic deformation strain amplitude, with limits for which under a minimum strain amplitude sub-grain structure may not form at all.

To summarize, dislocations annihilation and rearrangement to form the sub-grain microstructure are the causes of cyclic softening during cyclic deformation of 1CrMoV.

4.3 Miner's rule: verification of effectiveness

The Palmgren-Miner rule is the most widely accepted rule for predicting the fatigue damage for multiple amplitude loading conditions. The equation,

$$\sum_{j=1}^k \frac{n_j(\varepsilon_j)}{N_j(\varepsilon_j)} = C$$

assumes C to be 1 for design purposes.

In the attempt to evaluate sources of inaccuracy in design and remaining life assessment of materials subject to creep-fatigue loading conditions, the Miner's rule was tested in order to assess its effectiveness when predicting fatigue damage of materials subject to cyclic loading conditions at high temperatures.

Four different loading histories with variable strain amplitude were performed. The loading histories were based on the same strain cycling (see Table4.1) performed to assess the constant strain amplitude LCF properties of 1CrMoV, so that the calculation to assess the fatigue damage was based on the results of Table4.2. According to common design practice, a fatigue damage (D_F) equal 1 was expected. The results are shown in Table4.8.

Table4.8 Results obtained testing the Miner's rule.

Loading history	Loading history details	Damage summation	Deviation [%]
<	$\frac{N_i(0.25)}{3} + \frac{N_i(0.5)}{3} + n_i(0.7)$	$D_F = \frac{1}{3} + \frac{1}{3} + \frac{157}{453} = 1.01$	+1
>	$\frac{N_i(0.7)}{3} + \frac{N_i(0.5)}{3} + n_i(0.25)$	$D_F = \frac{1}{3} + \frac{1}{3} + \frac{685}{5583} = 0.79$	-21
<>	$\frac{N_i(0.25)}{5} + \frac{N_i(0.5)}{5} + \frac{N_i(0.7)}{5} + \frac{N_i(0.5)}{5} + n_i(0.25)$	$D_F = \frac{1}{5} + \frac{1}{5} + \frac{1}{5} + \frac{1}{5} + \frac{658}{5583} = 0.92$	-8
><	$\frac{N_i(0.7)}{5} + \frac{N_i(0.5)}{5} + \frac{N_i(0.25)}{5} + \frac{N_i(0.5)}{5} + n_i(0.7)$	$D_F = \frac{1}{5} + \frac{1}{5} + \frac{1}{5} + \frac{1}{5} + \frac{62}{453} = 0.94$	-6

Where $N_i(0.25)$, $N_i(0.5)$ and $N_i(0.7)$ are number of cycles to crack initiation at respective strain amplitudes, whereas $n_i(0.25)$, $n_i(0.5)$ and $n_i(0.7)$ are the number of cycles to crack initiation of the last loading block.

The fatigue damage D_F has been calculated by summation of the fatigue damage fractions relative to every loading block.

The results in Table4.8 show the tendency to under estimate the fatigue damage for decreasing strain amplitude loading histories: the rule tends to predict lower fatigue damage when the decreasing strain amplitude is more important (i.e.: when the decreasing sequence is the one dominating the test), hence it becomes non-conservative.

With the scope of understanding what affects the material response during variable strain amplitude cyclic deformation tests, eventually observed phenomenon were analysed in order to find relationships with fatigue damage accumulation.

In particular, stress-strain hysteresis loops were analysed and plotted in terms of stress range versus cycles diagrams (see next figure, remembering that the cyclic deformation tests were performed at constant strain amplitudes) in order to evaluate the cyclic softening response of the 1CrMoV steel when subject to variable strain amplitude with respect to constant strain amplitude cyclic deformation.

In this contest, interesting results were found in terms of cyclic softening rate (calculated as the ratio of stress peak decrease on number of cycles increase during the steady regime of cyclic deformation. I.e.: the slope of the central part of a stress-cycle diagram representative of a material response to cyclic deformation) change with respect to the constant strain amplitude cyclic deformation tests, depending on whether the variable strain amplitude cyclic deformation was characterized by increasing or decreasing strain amplitudes.

In other words, during the comparison of variable to constant strain amplitude cyclic deformation tests, significant changes in the cyclic softening rate were observed to take place, depending on the previous strain amplitude.

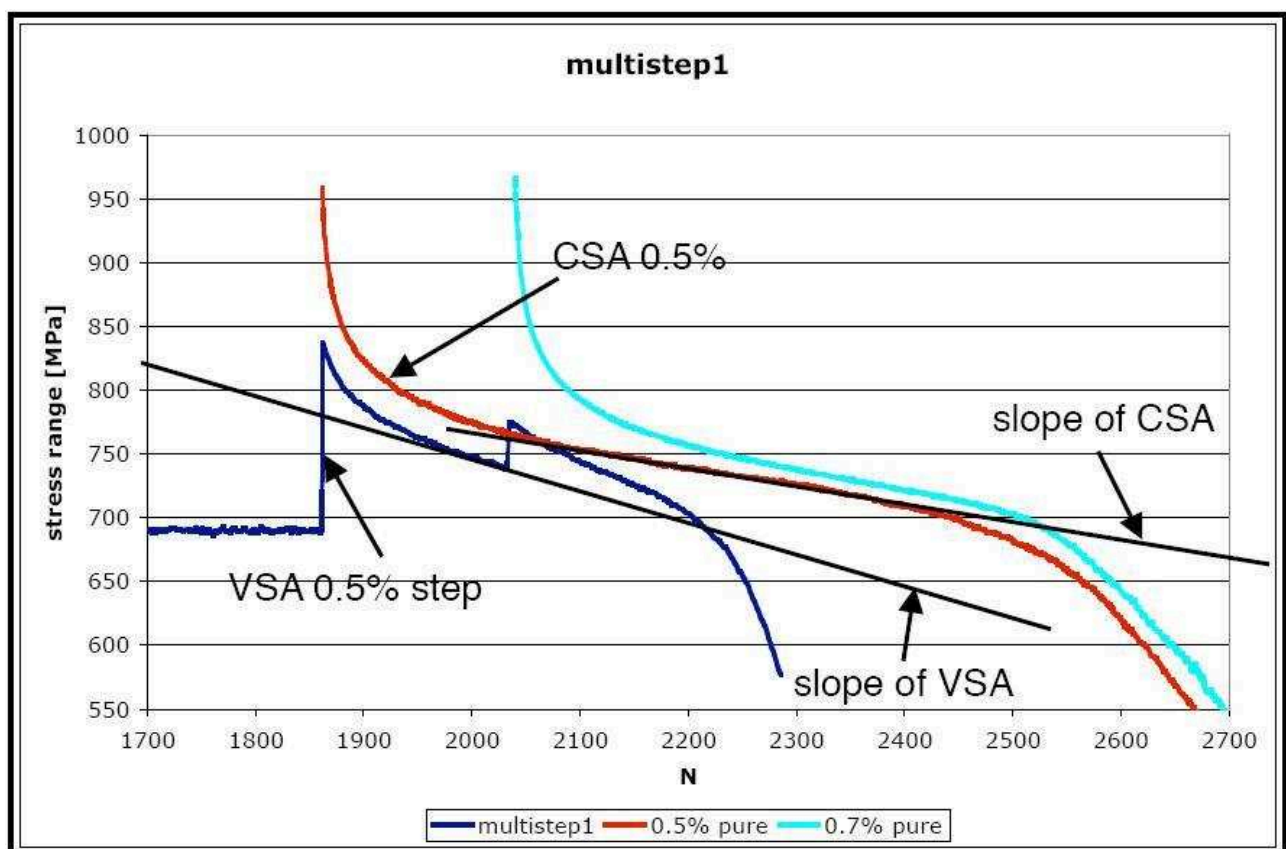


Fig.4.6: comparison of cyclic softening slopes of variable strain amplitude (VSA) to constant strain amplitude (CSA) cyclic deformation tests. In this case the multistep test is represented as the VSA test, characterized by decreasing strain amplitudes.

This observation was found being valid for the test campaign as it is confirmed by the following tables.

gradient of cyclic softening at quasi-steady part for CSA [MPa/cycle]					
0.25%		0.50%		0.70%	
HT98	-0.008	HT128	-0.138	HT1	-0.185
HT99	-0.0055	HT129	-0.138	HT93	-0.175
HT100	-0.0063	HT146	-0.127	HT94	-0.217
Average	-0.0066	Average	-0.134	Average	-0.192

Table4.9: Cyclic softening rate for CSA cyclic deformation tests. Average values are marked with colours.

Comparing the VSA to CSA of the same strain amplitude, the cyclic softening rate (i.e.: the slope) appears always higher - in absolute value - when the strain amplitude sequence is increasing, and lower when the strain amplitude sequence is decreasing.





slope of cyclic softening and stress range at ending part of each step for VSA [MPa/cycle]					
loading	step 1	step 2	step 3	step 4	step 5
	-	-0.284	-0.3556	-	-
	-	-0.08	-0.0043	-	-
	-	-0.784	-0.286	-0.1	-0.0059
	-	-0.14	-0.01,-0.0	-0.2324	-0.359

Table4.10: Cyclic softening rate of VSA cyclic deformation tests. Softening rate values of VSA tests are marked with colours used in the previous table for steps with same strain amplitude.

The comparison of VSA tests to CSA tests confirms that, in presence of descending strain amplitude loading the softening rate decreases (in absolute value) whereas in presence of increasing strain amplitude loading the softening rate increases (in absolute value).

This trend is shown in the following table, where the green filling identifies all the VSA tests steps where this observation is true and the red fill identifies the steps where the servation is not valid.





slope of cyclic softening and stress range at quasi-steady part for VSA [MPa/cycle]					
loading type	step 1	step 2	step 3	step 4	step 5
	-	-0.284	-0.3556	-	-
	-	-0.08	-0.0043	-	-
	-	-0.784	-0.286	-0.1	-0.0059
	-	-0.14	-0.01,-0.019	-0.2324	-0.359

Table4.11: Cyclic softening rate of VSA tests. Comparison to softening rate change theory: green cells indicate where the theory is confirmed, red cells where the theory is not confirmed by experiments.

The observation is not true for the steps 2 and 3 of the multistep test characterized by decreasing followed by increasing strain amplitude loading. The deviation from the softening rate values of the corresponding strain amplitude of CSA tests is anyway small, and the consideration that an increasing strain amplitude cyclic deformation increases the softening rate (and viceversa) of 1CrMoV at 565°C seems valid to the author.

Anyway, coming back to the analyses of the Miner's rule reliability for the fatigue damage assessment of the 1CrMoV steam turbine rotor steel at 565°C, the conclusion to this subchapter is that besides loading sequences largely dominated by decreasing strain amplitudes, the results confirm the effectiveness of the Miner's rule when predicting the fatigue damage under variable strain amplitude LCF.

4.4 Type 316 Stainless Steel

A Type 316 stainless steel was subjected to cyclic deformation in order to investigate its influence on subsequent creep properties. The details of material pedigree for this steel are given in appendix II. The influence of prior cyclic deformation on creep properties will be the subject of study of the following chapter. In this chapter the focus is on the response of the Type 316SS to cyclic deformation.

Table4.12 shows the cyclic deformation test details and the test results in terms of fatigue endurance and cyclic hardening.

Table4.12: Type 316SS: cyclic deformation test details and results

Test	T [°C]	ϵ_a [%]	$\dot{\epsilon}$ [%/s]	$N_{2\%}$	Time to $N_{2\%}$ [h]	N_{PH}	$\sigma_{N=N_{PH}}/\sigma_{N=1}$ [MPa/MPa]
LCFA	550	± 0.3	0.025	6348	85	500	3.34 (377/113)
LCFB	550	± 0.8	0.025	503	18	78	2.01 (337/168)

The stress-cycle response of the Type 316SS subjected to $\pm 0.8\%$ strain amplitude cyclic deformation at 550°C (LCFB) is shown in Fig.4.7. The initial fast cyclic hardening is a consequence of new dislocations generated during the accumulation of plastic strain. During the accumulation of plastic deformation, until the hardening peak, the rate of new dislocation generation is higher than the rate of dislocation annihilation. This leads to dislocation density increase, which is responsible for cyclic hardening.

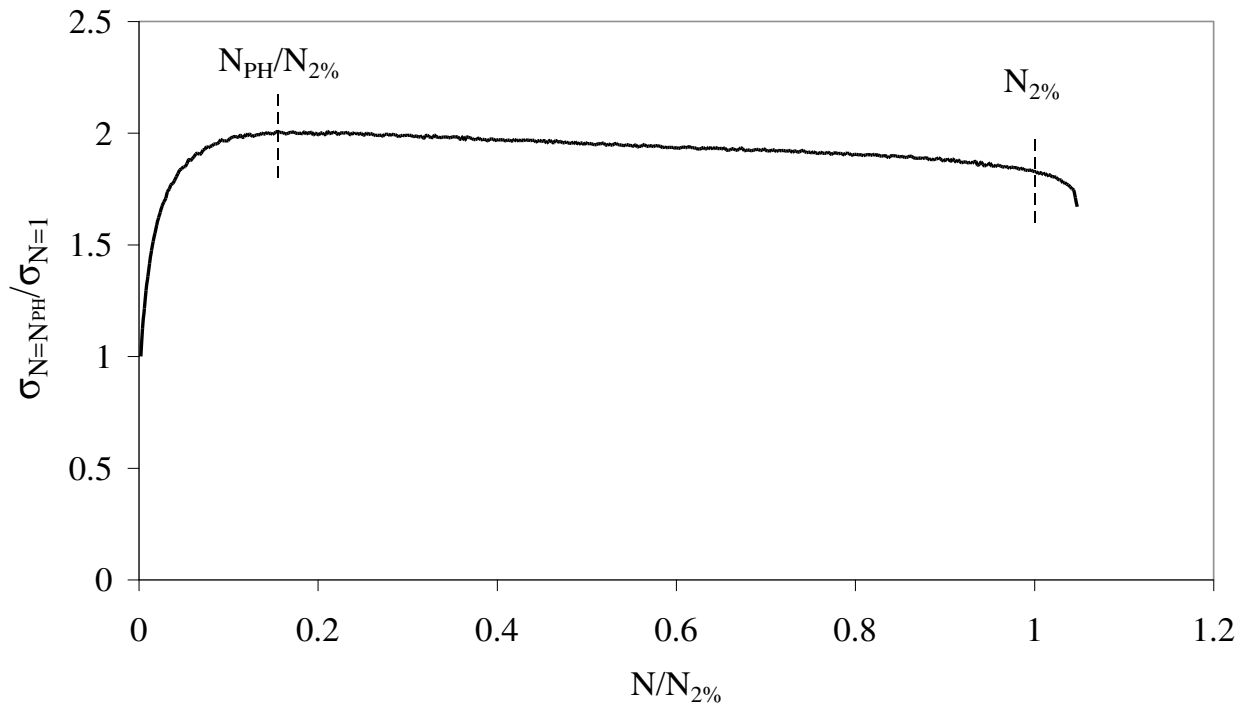


Fig.4.7: Stress-cycle response of Type 316SS at 550°C (LCFB)

For both LCFA and LCFB cyclic deformation tests the peak hardening was reached at about 10% of the fatigue life fraction (respectively 7.9% and 15.5% for LCFA and LCFB).

4.4.1 Post Test Inspection

In order to investigate micro-structural changes produced during cyclic deformation and responsible for cyclic hardening in 316SS, two tests (LCFA-BIS and LCFB-BIS) equivalent to the cyclic deformation histories LCFA and LCFB were performed and stopped at the same fatigue life fraction (0.1N_{2%} load drop, close to the hardening peak, see Table4.13).

Such testpieces have been post test investigated together with material in the as received condition in order to assess microstructure evolution, considered to be responsible for cyclic softening. Vickers hardness tests, grain size measurements and optical microscopy were performed in order to find a relationship between mechanical properties change and microstructural change.

Table4.13: Prior cyclic deformation details of post test inspections (PTI)

Test	T [°C]	ϵ_a [%]	$\dot{\epsilon}$ [%/s]	Cycles	Test time
LCFA-BIS	550	±0.3	0.025	634	8h30'
LCFB-BIS	550	±0.8	0.025	50	1h47'

4.4.1.1 Hardness

Hardness values were measured through HV30 tests (according to standard practice [4]) all along the parallel length for as-received material and for material subjected to LCFA-BIS (see Table4.14).

The hardness was approximately constant along the specimen parallel length, either on the specimen axis or at mid-radius positions between axis and surface (HV values given above are mean values measured within the parallel length).

Table4.14: Hardness measures

	As-received	LCFA-BIS
Vickers Hardness	143.7	189.6

As for the 1CrMoV steel, the grip end hardness was measured and found to be the same as that of as-received Type 316 stainless steel.

4.4.1.2 Grain size measurements

Grain sizes of as-received and cyclic deformed 1CrMoV were measured according to standard practice [5]. Prior cyclic deformation is not responsible for austenite grain size changes. According to the Hall-Petch relationship ($\sigma_y = \sigma_0 + K_y \cdot 1/\sqrt{d}$, [27] and [47]), the strength is inversely related to the grain size, but grain size measurements have not indicated any variation (see Table4.15 and Table4.16).

Table4.15: Grain size of as-received 316SS (X63 magnification)

Field	number of grains	grain size
1	66	119.4
2	62	127
3	67	117.6
4	70	112.6
5	63	125
6	66	119.4
7	68	115.9
8	69	114.2
9	59	133.6
10	66	119.4
avg grain size		120.4

Table4.16: Grain size of cyclic deformed 316SS according to LCFA

Field	number of grains	grain size
1	63	125.1
2	69	114.2
3	63	125.1
4	60	131.3
5	61	129.2
6	59	133.6
7	62	127.1
8	65	121.2
9	62	127.1
10	67	117.6
avg grain size		125.1

Hence the grain size is not considered to be the cause of cyclic hardening during cyclic deformation.

The dislocation dynamics seem to be once again the process governing the stress-cyclic response. Indeed the Type 316SS cyclic hardens because the dislocation density increases (the rate of new dislocations generation is higher than the rate of dislocations annihilation) to accommodate further plastic strain accumulation.

4.5 Concluding Remarks

The response of 1CrMoV to cyclic deformation at high temperatures was analyzed. Dislocation annihilation and rearrangement were identified as effects of cyclic deformation and causes of cyclic softening.

An investigation of the effectiveness of the Miner's rule (tested on 1CrMoV) leads to confirm its validity as a means for fatigue damage analyses and it also leads to focus on the creep damage determination as a possible source of error when the creep-fatigue damage calculation is performed.

The response of 316SS to cyclic deformation at high temperatures was also investigated. Dislocation multiplication was identified as the effect of cyclic deformation leading to cyclic hardening.

The observations above suggest considering the influence of prior cyclic deformation on subsequent creep behaviour as an important factor which may affect the creep damage calculation.

This will be the objective of chapter 5, where a typical TMF damage analyses is presented together with the research performed in order to understand the possible causes influencing the damage calculation.

5 CREEP-FATIGUE DAMAGE CHARACTERISATION

A series of service cycle thermo-mechanical fatigue tests were carried out prior to this research activity to provide a collation of well characterised deformation and endurance data for the 1CrMoV rotor steel heat under investigation (see [33]), ultimately to examine the analytical effectiveness of state-of-the-art creep-fatigue assessment procedures. An integral part of these investigations was the post test examination of TMF testpieces to fully characterise their damage condition with respect to the material mechanical property data to which it related. The main purpose of this action was to mechanistically qualify the deformation and endurance data gathered in terms of their practical applicability.

The evidence of physical damage accumulated during test by the specimens in this campaign is considered with reference to output from detailed finite element simulations of the series of TMF experiments. Recommendations are also offered in this chapter in order to analytically assess the creep-fatigue damage in a way which is more consistent with the physical damage observed in TMF testpieces as results of tests and post test inspections.

5.1 TMF tests on 1CrMoV

Details of TMF tests performed are available in [33]. Service-cycle TMF tests were performed on uniaxial tensile testpieces with a gauge section diameter of 12.7mm and gauge length of 12.7mm. Three types of TMF cycles were investigated. Common to each were the detail of the mechanical strain range cycle (1.4%), and the maximum temperature in the thermal cycle (565°C), Fig.5.1.

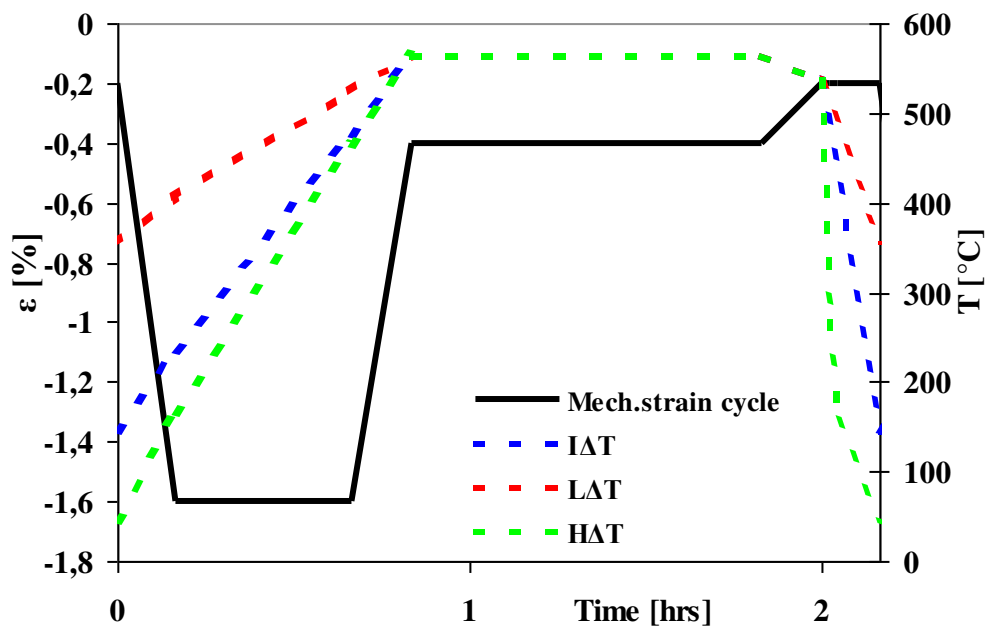


Fig.5.1: TMF test cycle details for the three cycle types LΔT, IΔT and HΔT [33].

The superimposed temperature transients between T_{\min} and 565°C resulted in TMF cycles which had both in-phase and out-of-phase components. ΔT for the three cycle types was 210°C (L ΔT), 420°C (I ΔT) and 520°C (H ΔT), to simulate a range of turbine start conditions.

The temperature along the gauge length was maintained to within $\pm 2^{\circ}\text{C}$ in order to avoid the geometrical instability observed in previous tests [32] where the temperature was maintained, according to the ASTM standards [3], to within $\max[\pm 0.01T_{\max}; \pm 3^{\circ}\text{C}]$.

5.1.1 Test results

The initiation criteria adopted to assess the endurance of 1CrMoV subjected to TMF and to interrupt the tests was the 2% load drop.

The magnitude of the thermal transient was the only variable differentiating the three TMF tests and affected $N_{2\%}$ in the way shown in Fig.5.2.

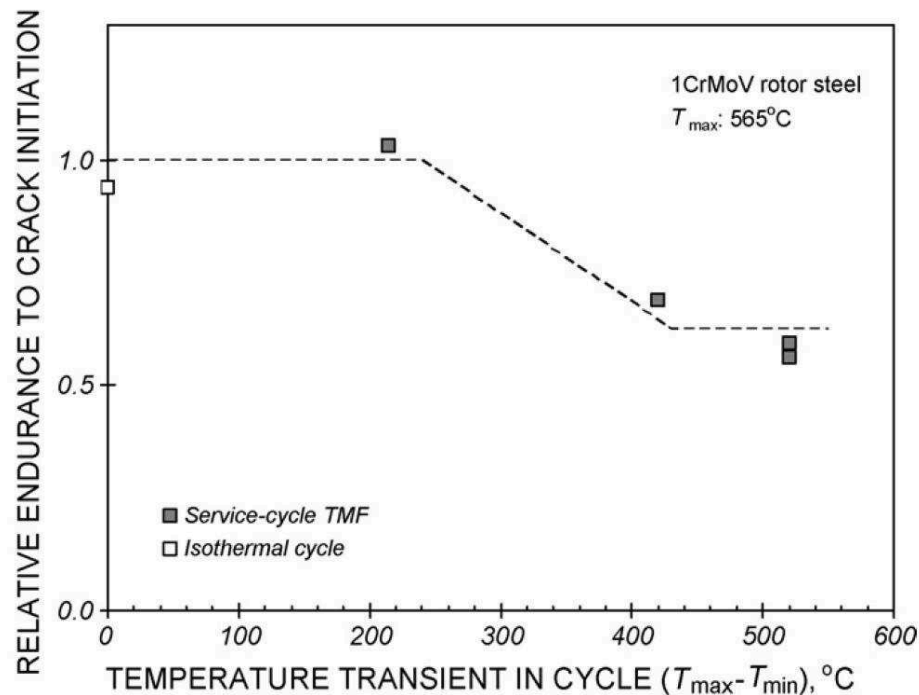


Fig.5.2: Effect of thermal transient on TMF crack initiation resistance [33]

The isothermal cycle result represents a test performed with the same mechanical strain cycle and constant temperature fixed at 565°C .

A thermal transient increase up to 200°C has no effect on fatigue crack initiation endurance. Over 200°C , the thermal transient reduces the number of TMF cycles to crack initiation.

Post test inspections and finite element analyses were performed in order to understand the reason for such fatigue endurance reduction.

5.1.2 Post Test Inspection

PTI form integral part of creep-fatigue damage assessment procedures. Optical microscopy investigations of testpieces subject to cycle types L Δ T, I Δ T and H Δ T are shown in Fig.5.3 [33].

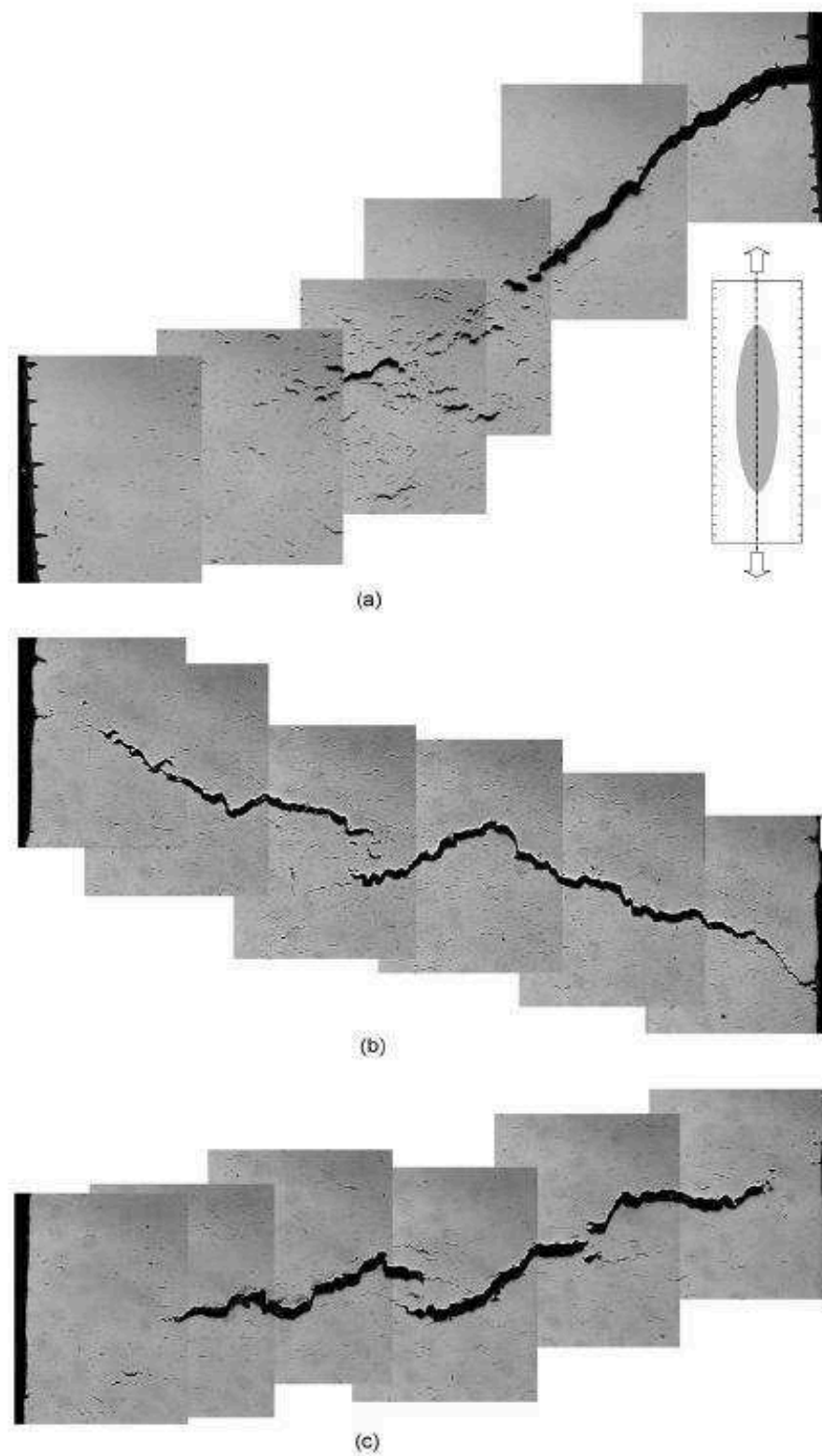


Fig.5.3: Damage development in TMF testpieces subject to (a)L Δ T, (b)I Δ T and (c)H Δ T cycle [33]

The L Δ T testpiece (a) was the only one exhibiting a crack initiating at the surface, with crack development to sub surface creep damage concentrated in the center of the parallel length. The surface is densely populated with short transgranular fatigue cracks, and the oxidation state is advanced. Hence the testpiece subjected to the L Δ T cycle was affected by simultaneous creep-fatigue interaction.

The situation is different for I Δ T (b) and H Δ T (c) testpieces, where the main crack initiated from the center and the short transgranular fatigue cracks density on the surface is much lower. There is also evidence of surface material removal induced by the larger thermal transient due to oxidation-spallation. Hence the testpieces subjected to the I Δ T and H Δ T cycles were damaged by a creep dominated failure mechanism (see paragraph 2.3).

5.2 Finite Element analyses

The scope of non-linear finite element analyses was to determine the stress-strain response of 1CrMoV subjected to the TMF cycles described in section 5.1. Results of finite element analyses were used, as it will be widely discussed later, to assess the creep-fatigue damage and to compare results of the assessment to those of post test inspections. The constitutive model implemented in Abaqus was the same developed by [18] and [40].

Fig.5.4 shows the finite element model adopted for the analysis. In order to simulate the real test loading conditions, the displacement of the nodes at plane B was imposed to control the gauge elongation (i.e. the relative displacement between node 4 and 11 along the u_2 direction).

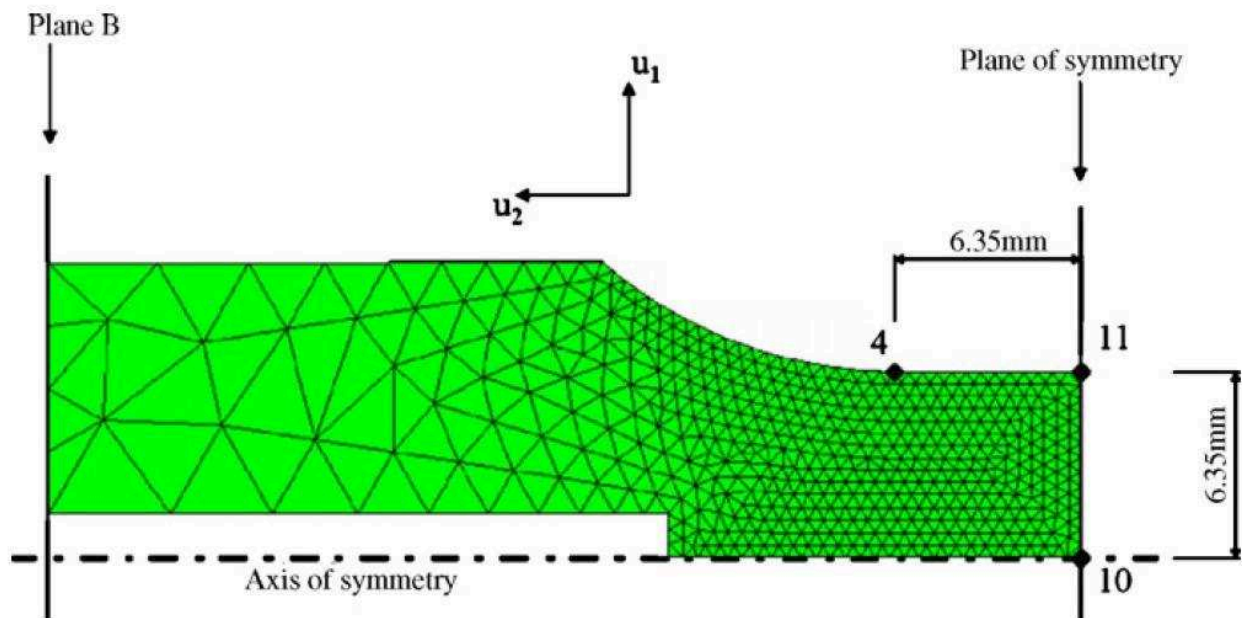


Fig.5.4: Details of the finite element mesh, with locations of nodes 4, 10 and 11 and plane B [33].

The finite element model is able to predict at each node the stress-strain response of 1CrMoV and the analytical creep-fatigue damage assessment (D_F - D_C) can then be locally performed on the basis of the Miner's rule (D_F) and on the basis of either the time fraction rule or the ductility exhaustion rule (D_C).

The creep-fatigue damage assessment discussed in the following text will be performed with reference to:

- 1) The creep deformation accumulated at the node 10, as far as the creep life fraction is concerned. At this node the plastic deformation was predicted larger and hence the occurring damage most critical.
- 2) The nominal cyclic deformation accumulated at the plane of symmetry, as far as the fatigue life fraction is concerned. On this plane the cyclic deformation is more severe and leads to fatigue cracks opening from the outer surface (i.e. from node 11) as demonstrated by common macrographs representative of fatigue damage (e.g.: Fig.5.3).

5.2.1 Time fraction rule based damage assessment

Creep-fatigue damage was assessed on the basis of standard assessment procedures (see chapter 2). The damage summation diagram with creep damage calculated on the basis of the time fraction rule is shown in Fig.5.5.

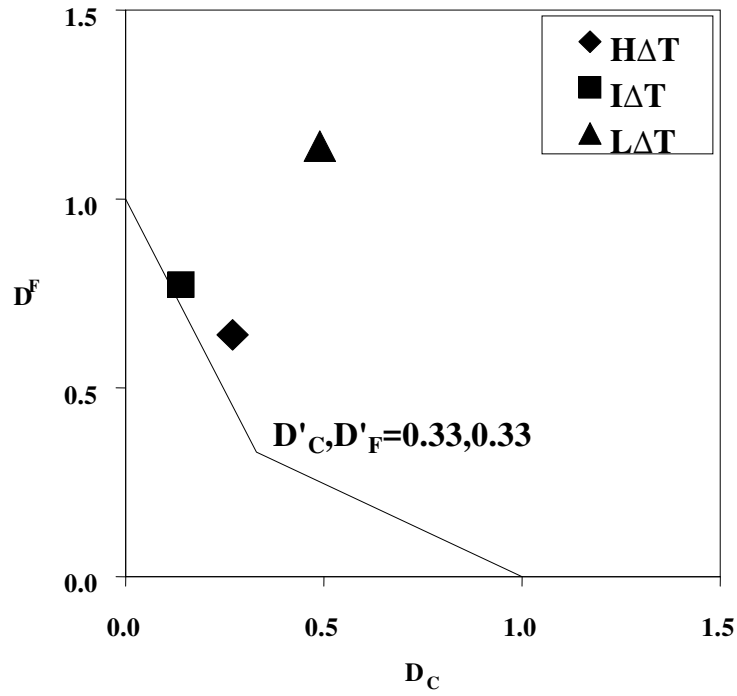


Fig.5.5: Bi-linear creep-fatigue damage summation diagram with (D_C, D_F) coordinates of service-cycle TMF tests based on conventional $N_f(T, \epsilon_a)$ and $t_u(T, \sigma_1)$ data, calculated according with the time fraction rule.

The D_F and D_C coordinates are also shown in Table5.1.

Table5.1: Damage coordinates according to ductility exhaustion

TMF test	D_F	D_C
$H\Delta T$	0.64	0.27
$I\Delta T$	0.77	0.14
$L\Delta T$	1.14	0.49

The damage assessed on the basis of the time fraction rule (Fig.5.5) shows non-negligible inconsistencies between analytical results and observed physical damage for the $I\Delta T$ and $H\Delta T$ testpieces.

5.2.2 Ductility exhaustion rule based damage assessment

The damage summation diagram with creep damage calculated on the basis of the ductility exhaustion rule is shown in Fig.5.6.

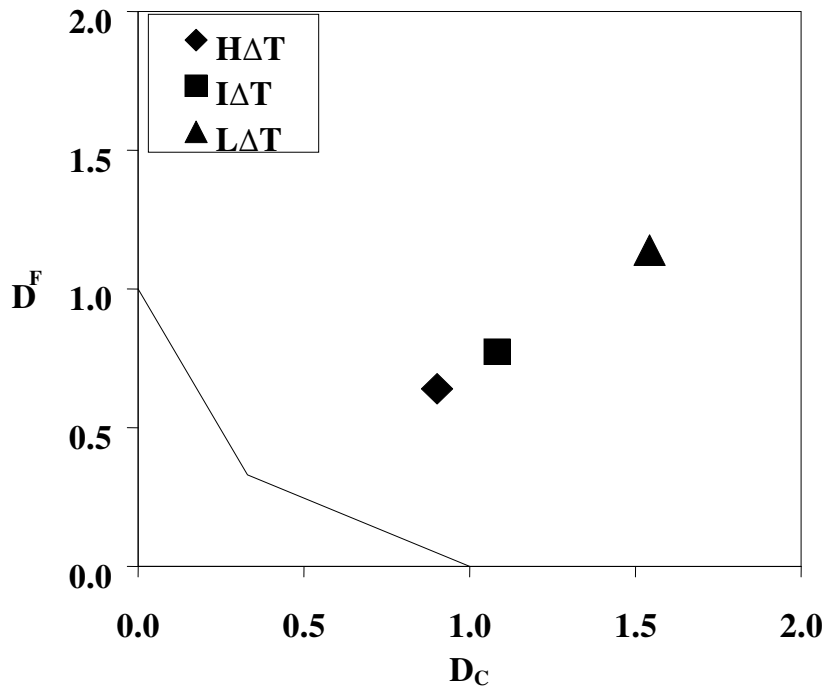


Fig.5.6: Bi-linear creep-fatigue damage summation diagram with (D_C, D_F) coordinates of service-cycle TMF tests based on conventional $N_f(T, \epsilon_a)$ and $t_u(T, \sigma_t)$ data, calculated according with the ductility exhaustion rule.

The D_F and D_C coordinates are also shown in Table5.2.

Table5.2: Damage coordinates according to ductility exhaustion

TMF test	D_F	D_C
$H\Delta T$	0.64	0.90
$I\Delta T$	0.77	1.08
$L\Delta T$	1.14	1.54

The damage assessed on the basis of the ductility exhaustion rule (Fig.5.6) shows non-negligible inconsistencies between analytical results and observed physical damage for the $L\Delta T$ testpiece.

5.3 Need for further research

Given the importance of post test inspections as integral part of the damage assessment procedure, it is mandatory to understand the reasons for which the standard creep-fatigue damage calculation methods (see the results at sections 5.2.1 and 5.2.2) are not effective. The following sections examine the influence of:

- prior creep deformation on subsequent fatigue endurance
- prior cyclic deformation on subsequent creep properties
- effective negative creep strain increments

as sources of creep-fatigue damage.

5.4 Influence of prior creep deformation on fatigue endurance

Creep may have a beneficial or detrimental influence on the fatigue crack initiation resistance of 1CrMoV steel, depending on the deformation regime and the mechanism of damage development [57]. Prior to the formation of physical creep damage, either as grain boundary cavities or voids due to particle/matrix decohesion, fatigue crack initiation resistance is enhanced in material which has accumulated primary or secondary creep deformation. The effect is attributed to matrix softening and is similar in magnitude to that arising from thermal ageing [57]. The beneficial effect of creep deformation is reversed once physical creep damage is present (Fig.5.7). The point at which this occurs depends on the stress and temperature conditions responsible for creep, and the creep ductility of the steel [50]. At higher stresses and/or lower temperatures, significant physical creep damage is generated relatively late in the creep life in the form of voids due to particle/matrix decohesion, and final fracture is transgranular. In these circumstances, fatigue crack initiation resistance continues to be enhanced until late in the creep life due to the softening associated with tertiary creep. At lower stresses and/or higher temperatures, physical creep damage in the form of constrained grain boundary cavity growth can occur relatively early in the creep life when the creep ductility is low and later in life when creep ductility is higher. The development of physical creep damage at the grain boundaries has an increasingly detrimental effect on fatigue crack initiation resistance.

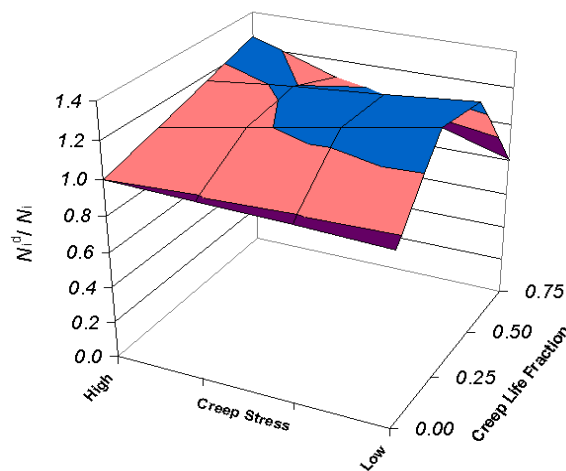


Fig.5.7: Influence of stress responsible for creep condition on fatigue endurance

The influence of prior creep deformation on fatigue crack initiation resistance was modeled according to the experimental results of [57], by interpolation of the data and taking the creep time fraction as reference parameter for the creep life fraction, and assuming a linear transition from high stress to low stress values as shown in Fig.5.7.

The equations representative of the influence of prior creep deformation on subsequent fatigue crack initiation resistance at high and low creep stress values are, respectively:

$$N_i^d / N_i = 0.0082 \cdot \left(\frac{t}{t_u} \right)^2 + 0.3313 \cdot \frac{t}{t_u} + 1 \quad (\sigma_{tg} \text{ high } \sigma - \text{transgranular}) \quad \text{eqn.5.1}$$

$$N_i^d / N_i = -3.61 \cdot \left(\frac{t}{t_u} \right)^2 + 2.5 \cdot \frac{t}{t_u} + 1 \quad (\sigma_{ig} \text{ low } \sigma - \text{intergranular}) \quad \text{eqn.5.2}$$

In transition between high and low stresses (i.e. between typical transgranular and intergranular creep damage mechanisms) the influence of prior creep deformation on subsequent fatigue crack initiation is leveraged on the basis of the stress value. This means that the influence of prior creep on fatigue endurance for an intermediate stress state is the weighted average of those represented in the above two equations, weighted on the basis of the stress relative value with respect to the transgranular and intergranular stress reference values.

So, for the general stress value σ , the corresponding influence of prior creep deformation on fatigue endurance is:

eqn.5.3

$$N_i^d / N_i (\sigma) = N_i^d / N_i (\sigma_{tg}) \cdot \frac{\sigma - \sigma_{ig}}{\sigma_{tg} - \sigma_{ig}} + N_i^d / N_i (\sigma_{ig}) \cdot \frac{\sigma - \sigma_{tg}}{\sigma_{tg} - \sigma_{ig}}$$

i.e.:

eqn.5.4

$$N_i^d / N_i (\sigma) = (0.0082 \cdot D_C^2 + 0.3313 \cdot D_C + 1) \cdot \frac{\sigma - \sigma_{ig}}{\sigma_{tg} - \sigma_{ig}} + (-3.61 \cdot D_C^2 + 2.5 \cdot D_C + 1) \cdot \frac{\sigma - \sigma_{tg}}{\sigma_{tg} - \sigma_{ig}}$$

This is the equation representative of the fatigue life fraction normalizing parameter corrected to take into account the influence of eventual prior creep deformation.

Hence, by knowing the amount of prior accumulated creep damage (D_C) and the number of cycles to crack initiation (N_i) of as-received material, accounting for a number of cycles to crack initiation of prior creep deformed material is possible. The consequent fatigue damage fraction will be calculated as:

eqn.5.5

$$d_F = \frac{1}{N_i^d}$$

5.5 Influence of prior cyclic deformation on creep properties

This chapter shows the results of an investigation performed in order to assess the influence of prior cyclic deformation on subsequent creep strength and ductility. Further details can be found in [12] and [13].

5.5.1 Creep tests of PCD 1CrMoV

Creep tests have been performed on a 1CrMoV steel at 565°C: *i*) in the virgin condition and following prior strain-controlled low cycle fatigue cycling to mid-life (i.e. $N/N_i = 0.5$) at strain amplitudes of *ii*) $\pm 0.25\%$ and *iii*) $\pm 0.7\%$. Details of the investigated 1CrMoV steel are given elsewhere (see appendix I). For the prior fatigue tests, the creep specimens shown in Fig.5.8b were tested to rupture following machining from the prior fatigue testpiece geometry shown in Fig.5.8a.

The variation in stress amplitude with cycle number for the two strain amplitude conditions is shown in the previous chapter. The softening associated with the $\pm 0.25\%$ strain cycle is significantly lower than that with the $\pm 0.70\%$ cycle.

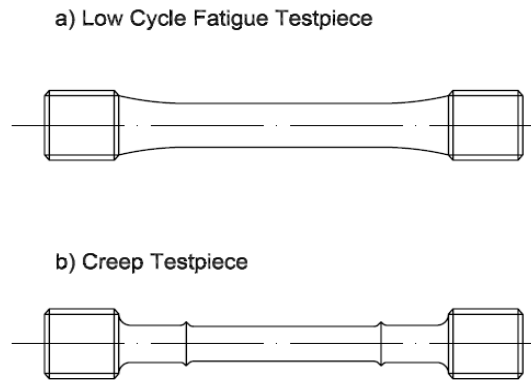


Fig.5.8: Testpiece geometries used for a) prior fatigue tests and b) subsequent creep tests, both at 565°C. b) is machined from a) after PCD

Tests were performed in order to assess the influence of prior cyclic deformation on subsequent creep properties.

The preconditioning was performed according to the ISO fatigue testing standard procedure [36] and with loading conditions indicated in paragraph 4.2 with labels LCF1-BIS and LCF3-BIS (hence till $N = 1/2 N_i$).

Creep tests were performed according to standard practice [21].

Results of creep tests performed on prior cyclic deformed 1CrMoV are shown in Table 5.3.

Table5.3: Creep properties of 1CrMoV subjected to PCD (565°C).

Testpiece	PCD	σ [MPa]	t_u [hrs]	$\dot{\varepsilon}_{\min}$ [%/hr]	A_u [%]	Z_u [%]	ε_f [%]
HT02	LCF3- BIS	243	4875	$2.85 \cdot 10^{-4}$	11.7	33.0	40.0
HT285	LCF3- BIS	270	428	$4.5 \cdot 10^{-3}$	14.3	73.8	134.1
HT156	LCF3- BIS	308	18.8	$1.8 \cdot 10^{-1}$	13.6	82.0	171.5
HT157	LCF3- BIS	308	9.2	$5.5 \cdot 10^{-1}$	16.9	81.8	170.1
HT103	LCF1-BIS	243	7201	$1.95 \cdot 10^{-4}$	5.9	16.2	17.6
HT104	LCF1-BIS	308	62	$4.5 \cdot 10^{-2}$	25	78.7	154.9

5.5.2 Post Test Inspection

5.5.2.1 Vickers Hardness measurements

Vickers Hardness was measured for as-received, cyclic deformed and crept materials (see Table5.4). The given hardness values are averages of measurements taken along testpiece axes and, for creep testpieces, starting from 4mm remote from the fracture surface (since plastic deformation affects local hardness).

Table5.4: Hardness values for As-received, Cyclic Deformed, Crept and PCD/Crept Materials

As-received	$\pm 0.25\%$ PCD	$\pm 0.70\%$ PCD	308MPa Crept	270MPa Crept	243MPa Crept
245	240	221	222	220	220

$\pm 0.25\%$ PCD -	$\pm 0.25\%$ PCD -	$\pm 0.25\%$ PCD -	$\pm 0.70\%$ PCD -	$\pm 0.70\%$ PCD -	$\pm 0.70\%$ PCD -
308MPa Crept	270MPa Crept	243MPa Crept	308MPa Crept	270MPa Crept	243MPa Crept
230	-	214	226	-	211

Hardness seems to depend on the amount of accumulated cyclic softening and on the accumulated creep deformation. In some cases, PCD reduces much the creep life of testpieces subjected to high loading conditions (responsible for ductile failure), hence also the possibility to reduce the strength below values measured with normal creep tests: this is evident with testpieces subjected to high stress (308MPa).

5.5.2.2 Grain size measurements

Grain sizes were measured to assess the influence of cyclic deformation on creep rupture properties (see Table5.5). In particular, grain size was measured for crept 1CrMoV (at 565°C, 308MPa) after PCD according to LCF3-BIS and the measurement was compared to that of as received, preconditioned material (subjected to LCF3-BIS) and normally crept 1CrMoV under same loading conditions. Cyclic deformation produced no grain size change, since the accumulated plastic strain was very small. In these tests, the grain size was measured to be 34.5µm for the as-received material and 32.7µm for cyclic deformed material ($N = 0.5N_i$, $\pm 0.70\%$, 565°C). The grain size measured in the crept testpiece affected by PCD was 41.1µm compared with that in the crept testpiece without PCD subjected to the same creep loading conditions (36.5µm).

Table5.5: Grain Sizes of As-received, Cyclic Deformed, Crept and PCD/Crept Materials

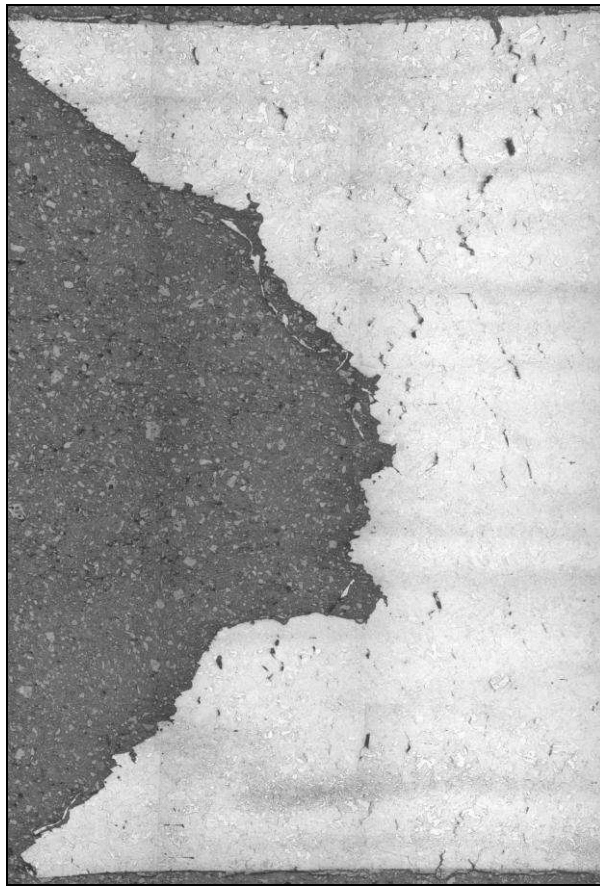
As-received	565°C $\pm 0.70\%$ PCD	565°C 308MPa Crept	565°C $\pm 0.70\%$ PCD 308MPa Crept
34.5 µm	32.7 µm	36.5 µm	41.1 µm

Whereas as-received 1CrMoV, PCD 1CrMoV and crept 1CrMoV seem to have nearly the same grain size, the PCD+Crept 1CrMoV shows relatively larger grain size.

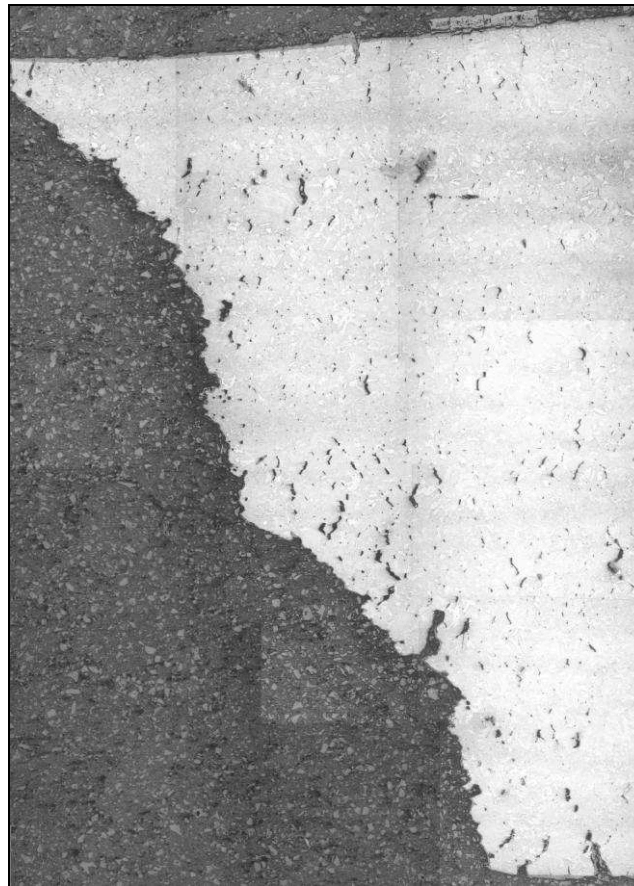
5.5.2.3 Creep damage mechanisms modification

The macrographs in Fig.5.9 show the observed modification to the creep damage mechanism occurring in creep testpieces subjected to a lower stress (243MPa) at 565°C *a)* without PCD, *b)* with PCD responsible for low cyclic softening and *c)* with PCD responsible for high cyclic softening. PCD shifts rupture from the lower shelf fully intergranular regime into the transition region in which there is a transgranular component to cracking.

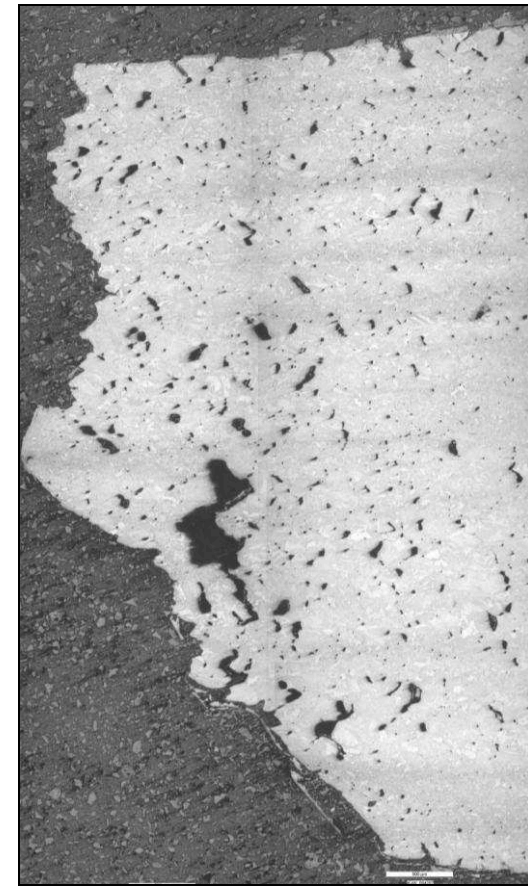
Fig.5.9: Influence of PCD on creep damage mechanisms



a. PCD: none ; Creep: 565°C, 243MPa



b. PCD: $\pm 0.25\%$; Creep: 565°C, 243MPa



c. PCD: $\pm 0.70\%$; Creep: 565°C, 243MPa

5.5.3 Influence of PCD on creep strength

A characteristic of 1CrMoV steel is that it softens as a consequence of cyclic strain controlled loading (see chapter 4). Cyclic softening occurs in such steels at elevated temperatures as a consequence of dislocation rearrangement from an initially tangled state to form a sub-grain structure in which the dislocation density is high at the boundaries and low in the intervening matrix [49]. The softening resulting from cyclic loading can be responsible for important changes in subsequent creep strength, creep deformation and creep damage mechanisms, the magnitude of the effect depending also on stress and temperature conditions.

The effect of mid-life prior fatigue damage on the creep strength of 1CrMoV steel at 565°C is shown in Fig.5.10. The effect of prior strain cycling is significantly more apparent in high stress creep tests than in lower stress creep tests.

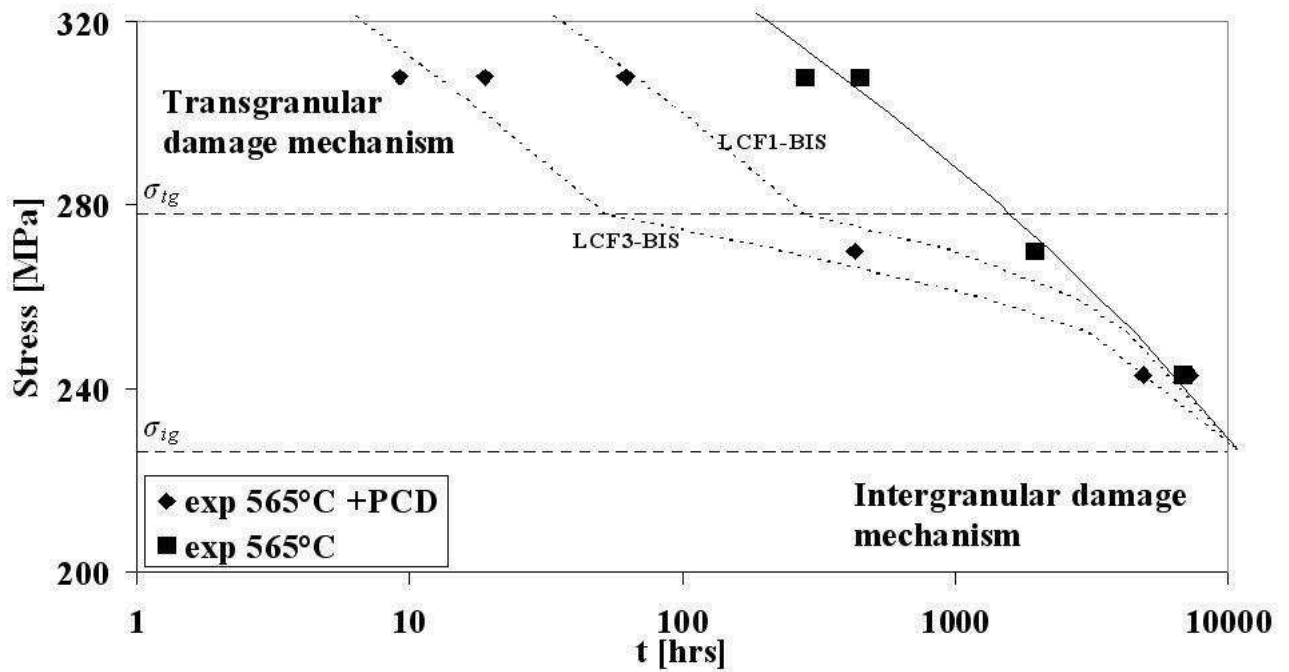


Fig.5.10: Influence of mid-life prior fatigue damage (PFD) on time to creep-rupture of 1CrMoV steel at 565°C

The results of experimental tests on 1CrMoV at 565°C have shown that cyclic softening can lead to an increase in minimum creep rate and a reduction in the time to creep-rupture in a way that is consistent with other observations [49]. Published information and the new results (Fig.5.10) form the basis of a model representation of t_u^s/t_u as a function of cyclic-softened condition and the stress responsible for creep (Fig.5.11).

At lower stresses leading to the development of creep damage by constrained cavity growth and intergranular creep rupture, there is not a significant reduction in rupture time with increasing cyclic-softening. In contrast, at higher stresses leading to transgranular creep rupture, there is a significant reduction in rupture time with increasing cyclic-softening.

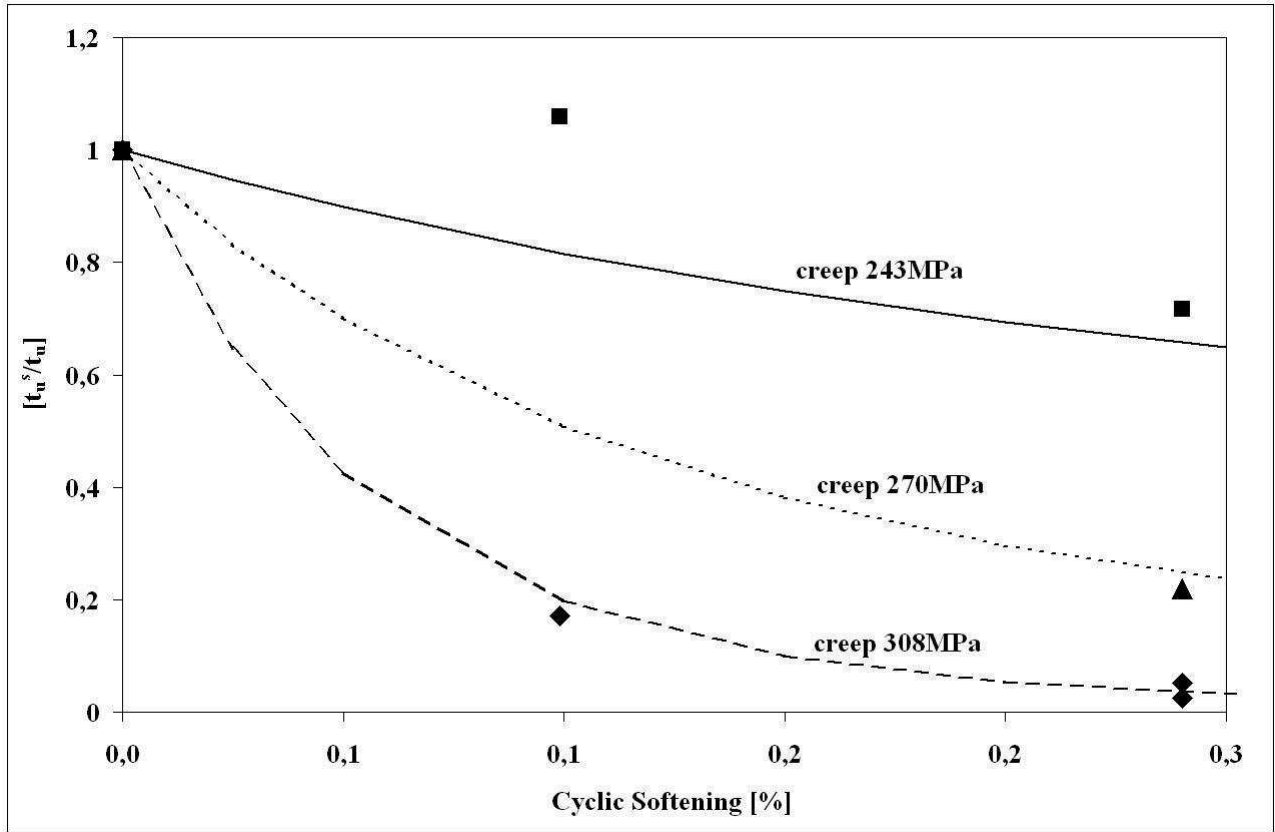


Fig.5.11: Influence of prior cyclic-softening ($1 - \sigma/\sigma_{N=1}$) and creep stress on t_u^s/t_u ratio

Times to creep-rupture reduce by an amount depending on the magnitude of the stress responsible for creep and on the amount of cyclic softening accumulated during strain cycling. Moreover, the effect is more significant if the amount of accumulated softening is high and if the subsequent creep test is loaded to relatively high stress (i.e. to a stress value responsible for power law creep and ductile transgranular creep rupture arising from particle/matrix decohesion). In this case, the critical inelastic matrix shear strain for rupture is attained earlier due to the plastic matrix shear strain already accumulated during prior cyclic deformation. If the subsequent creep test is loaded to relatively low stress (i.e. to a stress value responsible for diffusion creep and intergranular rupture), the influence of PCD on creep strength is much lower

These considerations can be modelled on the basis of experimental results, shown in Fig.5.11. For different values of stress responsible for creep, equations can describe the creep strength of 1CrMoV as reference of prior cumulated cyclic softening and stress responsible for creep, i.e.:

eqn.5.6

$$f(\text{cyclic} \cdot \text{softening}, \sigma)$$

More in detail, the creep rupture time of prior cyclic deformed 1CrMoV can be expressed as

eqn.5.7

$$t_u^s = t_u \cdot f(\text{cyclic} \cdot \text{softening}, \sigma)$$

and calculated by simply knowing the creep rupture time for as received material and the amount of prior cumulated cyclic softening.

In practice, $f(\text{cyclic} \cdot \text{softening})$ is specifically dependent on the material and testing conditions (both prior loading and subsequent creep), and was obtained simply through least square linear regres-

sion method (after removal of an outlier point correspondent to low softening and low creep stress) applied to experimental results obtained with the 1CrMoV, Heat 1 ([13] and [34]), at 565°C:

eqn.5.8

$$t_u^s/t_u = \text{EXP}((7,83 \cdot (\sigma/\sigma_{N=1})^2 - 8,531 \cdot (\sigma/\sigma_{N=1})) \cdot (6,264 \cdot 10^{-4} \cdot (\sigma - \sigma_{ig})^2 + 6,139 \cdot 10^{-3} \cdot (\sigma - \sigma_{ig})))$$

where $\sigma - \sigma_{ig}$ identifies the creep stress level exceeding the threshold for complete intergranular creep rupture whereas $\sigma/\sigma_{N=1}$ represents the amount of cyclic softening cumulated during prior cyclic deformation as reported in Fig.5.11.

Ultimately, the creep-fatigue damage assessment will be performed by calculating the creep damage fraction on the basis of the new normalizing parameter (t_u^s), i.e.:

eqn.5.9

$$d_c = \int_0^t \frac{dt}{t_u^s(\sigma, T, \text{cyclic} \cdot \text{softening})}$$

For simplicity, the present analysis neglects to consider the effect of the temperature on t_u^s , approximating it as constant and only dependent on stress and cumulated cyclic softening.

The same considerations concerning the influence of prior cumulated cyclic softening on creep properties are shown in Fig.5.12, in terms of creep strain rate as a reference of stress (Fig.5.10 and Fig.5.12 show the same information, though under different perspectives, of Fig.5.11, which is in fact the reference relationship to be considered for the most effective assessment of the influence of prior cyclic deformation on creep properties, as a mean for the creep damage calculation).

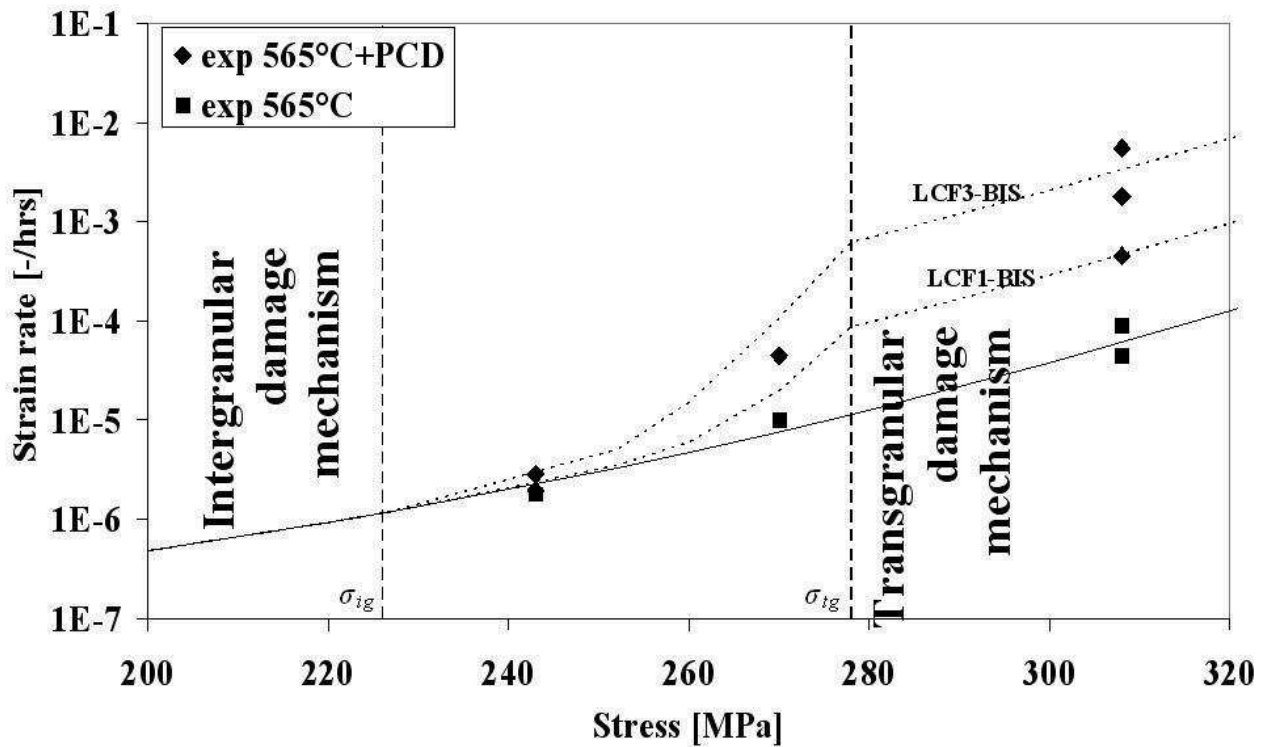


Fig.5.12: Influence of PCD and creep loading stress on minimum creep strain rate

5.5.3.1 The Monkman-Grant PCD independency

Fig.5.13 shows that the MG relationship for as-received 1CrMoV is also applicable for the steel in the PCD condition. PCD is responsible for a displacement along the MG $\dot{\epsilon}(t_u)$ line towards lower rupture times and higher creep rates.

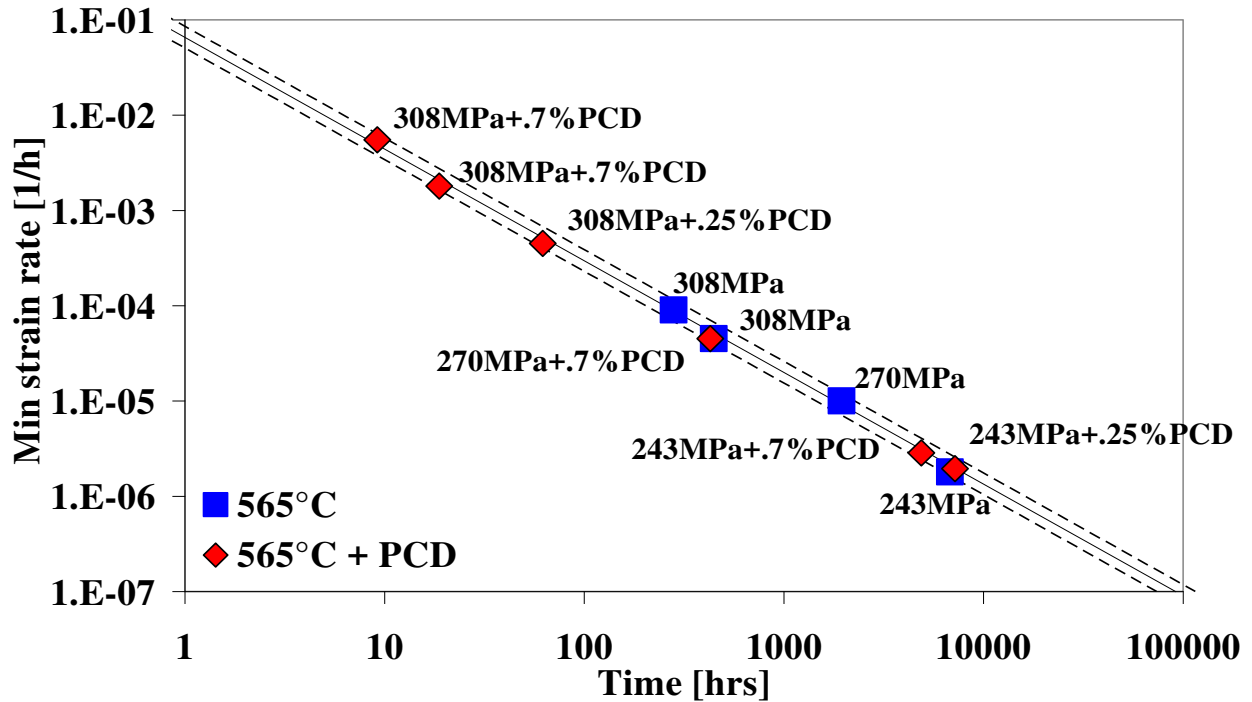


Fig.5.13: Influence of PCD on MG parameter at 565°C. Scatterbands are setted at $\pm 20\%$

The magnitude of the displacement is directly related to the amount of accumulated cyclic softening and/or to the stresses responsible for creep rupture. In addition to its influence on creep strength, PCD can significantly affect the creep rupture ductility by a change to the creep damage mechanism.

Such behaviour was observed at 565°C. Further research is required in order to analyse the material response at different temperature values.

5.5.3.2 Time fraction approach

Using the analytical constructions determined in the present study, the (D_C, D_F) co-ordinates given in Fig.5.5 to represent the IΔT and HΔT service-cycle TMF results described in section 5.1.1 have been recalculated. Relationships have been established to represent the effects of *i*) creep life fraction (creep condition) and stress (rupture mechanism regime) on N_i^d/N_i (Fig.5.7), and *ii*) fatigue softened condition and creep stress (rupture mechanism regime) on t_u^s/t_u (Fig.5.11), and these have been employed in an evolutionary damage calculation involving the constitutive equation set and FEA implementation mentioned in section 5.2. The new (D_C, D_F) co-ordinates are shown in (Fig.5.14) and more closely reflect the physical condition of damage exhibited by the IΔT and HΔT specimens following test (Fig.5.3). The new damage analyses of the LΔT specimen based on the time fraction rule, considering effective creep-fatigue reciprocal influences is however far more inconsistent with the observed physical damage.

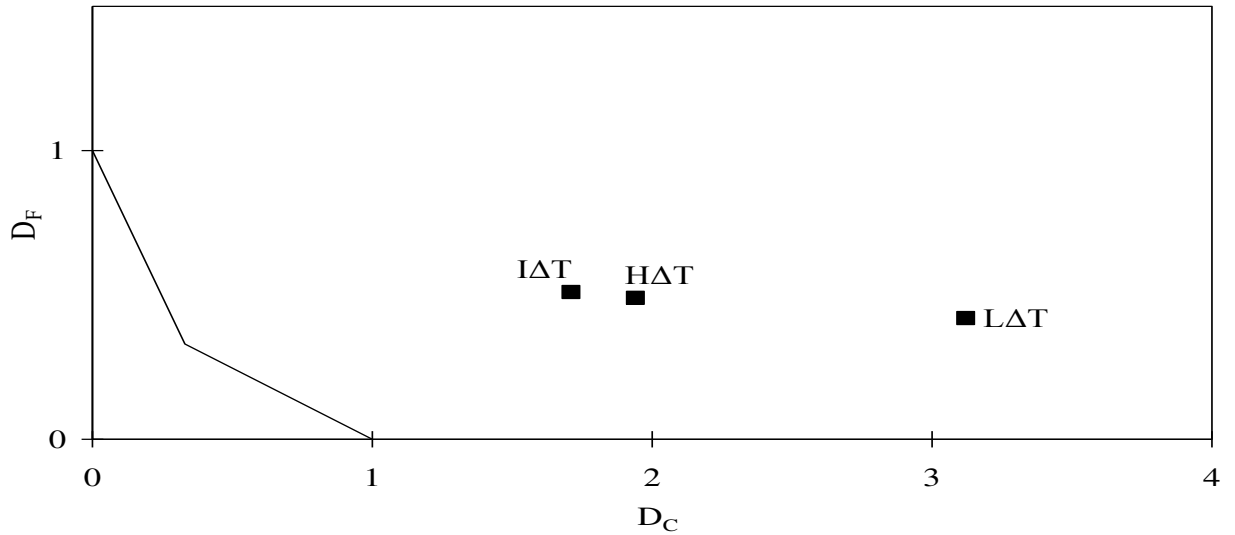
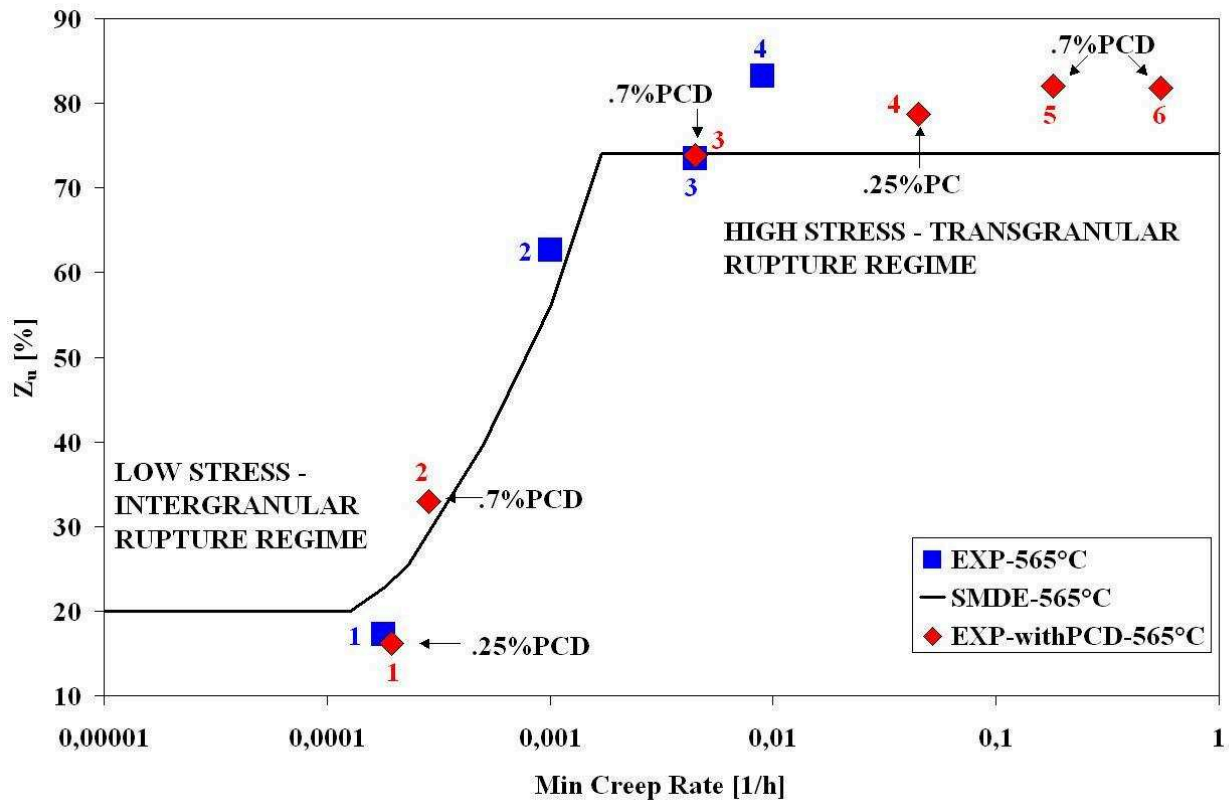


Fig.5.14: Bi-linear creep-fatigue summation diagram with (D_C, D_F) co-ordinates of service-cycle TMF tests based on modified $N_i(T, \varepsilon_a)$ and $t_u(T, \sigma_i)$ data

In order to assess the effectiveness of the introduced creep-fatigue reciprocal influences implementation, the creep-fatigue damage was assessed also on the basis of the ductility exhaustion rule. Hence the influence of PCD was not considered with respect to creep strength, rather on creep deformation and ductility.

5.5.4 Influence of PCD on creep ductility

The available experimental results suggest that the magnitudes of the upper and lower creep rupture ductility shelves do not change because of PCD and that the creep rupture ductility changes with creep strain rate in line with the characteristic $Z_u(\dot{\epsilon}_{\min})$ relationship for the given as-received material and temperature (Fig.5.15).



ID	σ [MPa]	$\dot{\epsilon}_{\min}$ [1/h]	Z_u [%]
1	243	0,00018	17,23
2	270	0,001	62,68
3	308	0,0045	73,44
4	308	0,009	83,22

ID	PCD	σ [MPa]	$\dot{\epsilon}_{\min}$ [1/h]	Z_u [%]
1	LCF1-bis	243	0,000195	16,18
2	LCF3-bis	243	0,000285	32,96
3	LCF3-bis	270	0,0045	73,83
4	LCF1-bis	308	0,045	78,75
5	LCF3-bis	308	0,18	82
6	LCF3-bis	308	0,55	81,76

Fig.5.15: Influence of PCD on $Z_u(\dot{\epsilon}_{\min})$. The creep data obtained after PCD are highlighted in red, to differentiate them from the standard creep test results, in red.

In Fig.5.15, $Z_u(\dot{\epsilon}_{\min})$ data points associated with PCD creep tests fall on the same creep rupture ductility line but towards higher creep strain rate values and, within the limits of the as-received material lower and upper ductility shelves, towards higher creep rupture ductility. The magnitude of this displacement along the $Z_u(\dot{\epsilon}_{\min})$ data line depends, as for the case of creep strength considered above, on the amount of cyclic softening accumulated during PCD and on the loading conditions responsible for creep.

The amount by which PCD affects creep strength (Fig.5.12), minimum creep rate (Fig.5.13) and rupture ductility (Fig.5.15) depends, for a given temperature, on the stress applied in the creep test. Prior cyclic deformation in 1CrMoV steel is responsible for a change in the dislocation condition due to similar climb and glide processes to those active during power law creep (see chapter 2.1.1). At stresses responsible for power law creep, PCD enhances the process of creep rupture to a greater extent when the mechanism is one of void formation due to particle/matrix decohesion leading to ductile transgranular fracture. At stresses responsible for diffusion creep, when rupture is a consequence of the formation of cavities at grain boundaries, the influence of PCD is much lower.

In higher stress creep tests, PCD has a significant influence on creep strength (Fig.5.12) and minimum creep rate (Fig.5.13), but little effect on the magnitude of the upper-shelf rupture ductility (Fig.5.15) and the rupture mechanism (in all cases being ductile transgranular rupture). In lower stress creep tests, the effect of PCD on creep strength (Fig.5.12) and minimum creep rate (Fig.5.13) is reduced, but the effect on rupture ductility (Fig.5.15) and the rupture mechanism (Fig.5.9) can be greater, if the creep loading conditions and the amount of accumulated cyclic softening lead to a change in the creep damage mechanism and the $Z_u(\dot{\epsilon}_{\min})$ ductility points moving up the transition line in Fig.5.15.

5.5.4.1 Ductility exhaustion approach

Considering the creep-fatigue reciprocal influences leads to a new creep-fatigue damage summation diagram with important differences in terms of both creep damage fraction and fatigue damage fraction, as shown in Fig.5.16.

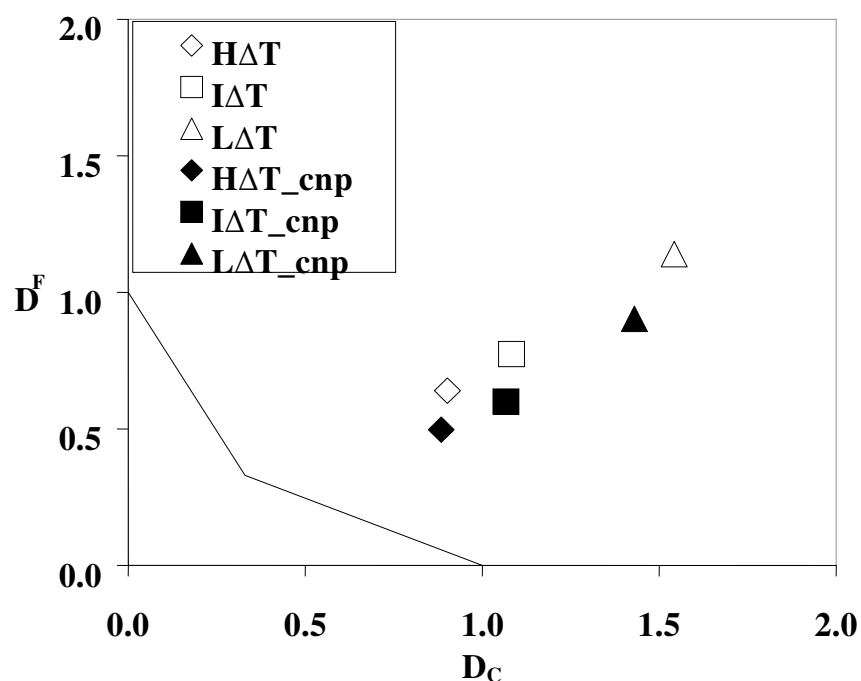


Fig.5.16: Effect of considering effective creep-fatigue reciprocal influences (through corrected normalizing parameters - cnp) in a damage assessment based on the ductility exhaustion rule. Empty points refer to standard ductility exhaustion rule based damage assessment (see Fig.5.6)

Table5.6: Damage coordinates, with implemented effective creep-fatigue reciprocal influences

TMF test	D_F	D_C
HΔT	0.50	0.88
IΔT	0.60	1.07
LΔT	0.90	1.43

5.5.4.2 Effective accumulation of creep strain in compression

Calculating the creep deformation for the determination of creep damage fraction requires the consideration of creep strain increments during compression stress states as sources of damage recovery. The creep damage fraction changes considerably when relevant time periods are characterised by damaging creep loading conditions with compression stress states. Fig.5.17 shows the importance of considering effective creep strain increments in compression when calculating the creep damage fraction. The $L\Delta T$ TMF test is particularly affected by this approach, since, the out-of-phase condition between mechanical strain and temperature produces compression stress states at typical creep temperatures.

This new idea of accounting for creep strain increments during compression stress states was implemented in a way to define tension and compression stress states on the basis of the hydrostatic tensor sign, and to account for positive the creep strain increments accumulated in tension stress states and for negative the creep strain increments accumulated during compression stress states.

As for all creep strain increments accumulation, the calculation was performed accounting for the effective (instantaneous) temperature and the corresponding material creep properties.

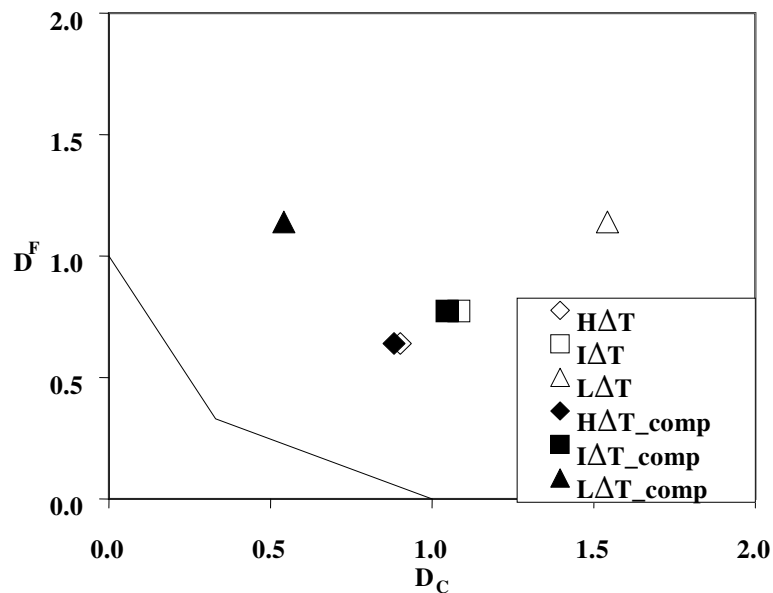


Fig.5.17: Effect of considering negative creep strain increments effective in a damage assessment based on the ductility exhaustion rule.

The results change in view of the fact that only the $L\Delta T$ test observes temperatures interesting for creep during plastic strain accumulation in compression. $I\Delta T$ and $H\Delta T$ were characterised by such low temperatures when strain was accumulated in compression, that creep phenomena were neglected.

Table5.7: Damage coordinates, with effective compression creep strain increments

TMF test	D_F	D_C
$H\Delta T$	0.64	0.88
$I\Delta T$	0.77	1.05
$L\Delta T$	1.14	0.54

5.6 Evolutionary creep-fatigue damage assessment

By combining the creep-fatigue reciprocal influences with effective creep strain increments during compression stress states, the creep-fatigue damage assessed through the ductility exhaustion rule gives the results shown in Fig.5.18.

The damage assessment model was implemented in a way to be fully evolutionary, i.e. at each time increment the creep damage increment was calculated on the basis of the accumulated fatigue damage fraction, and the fatigue damage increment calculated on the basis of the accumulated creep damage fraction.

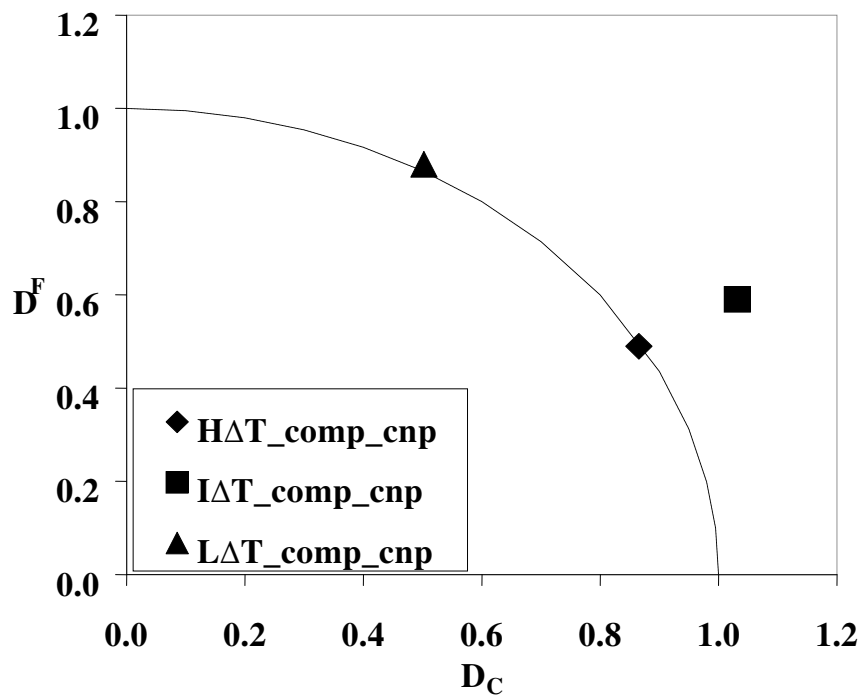


Fig.5.18: Effect of considering effective creep-fatigue reciprocal influences (through corrected normalizing parameters - cnp) and effective negative creep strain increments in a damage assessment based on the ductility exhaustion rule.

Table5.8: Damage coordinates, with implemented effective creep-fatigue reciprocal influences and effective negative creep strain increments.

TMF test	D_F	D_C
HΔT	0.49	0.87
IΔT	0.59	1.03
LΔT	0.88	0.50

5.7 Discussion

The creep-fatigue damage assessment performed on TMF tests in accordance with standard time fraction rule and ductility exhaustion rule was found in contradiction with the results of post test inspections executed on the same TMF testpieces.

A new way to assess the creep-fatigue damage implies to consider the creep-fatigue reciprocal influences and the accumulation of creep strain also during compression stress states.

The accounting for creep-fatigue reciprocal influences implies to modify the creep-fatigue normalizing parameters in a way that takes into account the effect of prior loading.

The normalizing parameters change depending on the level of stress responsible for creep, the amount of accumulated softening (or hardening, for cyclic hardening materials) and the amount of accumulated deformation during prior loading.

The accounting for creep strain accumulation during compression stress states is of fundamental importance for those TMF loading conditions in which compression stress states occur at high temperature. So it was for the TMF experiments analysed during this research activity, for which a new approach for the calculation of the creep strain accumulation was required.

This new approach may lead to a better consistency between analytically predicted and physically post test observed damage.

5.8 Type 316 Stainless Steel

The influence of prior cyclic deformation on subsequent creep properties was investigated for the Type 316 stainless steel also. The purpose of this investigation was to enable comparison to the results related to 1CrMoV for a material with a different microstructural constitution and different mechanical properties. Indeed prior cyclic deformation leads under particular circumstances to important cyclic hardening of 316SS, the effect due to the microstructure evolution. Hence the creep properties are expected to considerably change with respect to those of as-received material.

5.8.1 Creep tests of PCD material

Creep tests have been performed on a 316SS at 550°C: *i*) in the as received condition and following prior strain-controlled low cycle fatigue cycling at 550°C to 10% fatigue life fraction (i.e. $N/N_{2\%} = 0.1$) at strain amplitudes of *ii*) $\pm 0.3\%$ and *iii*) $\pm 0.8\%$. Details of the investigated 316SS are given in appendix II. The machining procedure to perform cyclic deformation first and then creep tests was the same adopted for the 1CrMoV and described in paragraph 5.5.1, as well as the testpieces geometry.

The pre-conditioning was performed according to fatigue testing standards [36] and with loading conditions indicated in paragraph 4.4.1 with labels LCFA-BIS and LCFB-BIS (hence until $N = 0.1 \cdot N_{2\%}$). The variation in stress range with cycle number for the two strain amplitude conditions is shown in Fig.4.7. The 316SS showed a cyclic hardening response and the magnitude of the peak stress at the same fatigue life fraction (10%) was nearly the same for the two strain amplitudes used for the pre-conditioning (hence the cyclic hardening was much higher after the LCFA pre-conditioning, as already observed in chapter 4.4). As it was done for the 1CrMoV steel, the tests were performed in order to assess the influence of prior cyclic deformation on subsequent creep properties.

Creep tests were performed on PCD 316SS according to standards [21] and the results are shown in Table5.9.

Table5.9: Creep properties of 316SS subjected to PCD (550°C).

PCD details	σ [MPa]	t_u [hrs]	$\dot{\epsilon}_{\min}$ [%/hr]	A_u [%]	Z_u [%]	ϵ_f [%]
LCFA- BIS	250	8300(*)	0.00069	-	-	-
LCFA- BIS	300	1757	0.0035	36.75	37.4	46.8
LCFB- BIS	250	9630	0.000531	37.7	52.2	73.8
LCFB- BIS	300	1435	0.0033	27.7	42.6	55.5

(*) not failed creep test.

5.8.2 Post Test Inspections

As it was done for the 1CrMoV steel, the post test inspection was performed on 316SS in order to assess the microstructural changes related to and/or responsible for cyclic hardening.

5.8.2.1 Vickers Hardness measurements

Vickers hardness was measured according to standard procedure [4] for as-received material, cyclic deformed material, crept material and crept material after cyclic deformation (see Table5.10). The given hardness values are averages of measurements taken along testpiece axes and, for creep test-pieces, starting from 4mm remote from the fracture surface (since plastic deformation affects local hardness).

Table5.10: Hardness values for As-received, Cyclic Deformed and PCD/Crept 316SS

As - received	$\pm 0.3\%$ PCD	$\pm 0.3\%$ PCD 300MPa Creep
143.7	189.6	235.4

Hardness is related to the amount of accumulated cyclic hardening and to the accumulated creep deformation.

5.8.2.2 Grain size measurements

The grain size was measured for crept Type 316 SS (at 550°C, 300MPa) after PCD according to LCFA-BIS and such measure was compared to that of as received material and pre-conditioned material (subjected to LCFA-BIS). Cyclic deformation and creep produced no grain size change, since the accumulated plastic strain was very small.

Table5. 11: Grain Sizes of As-received, Cyclic Deformed, Crept and PCD/Crept 316SS

As-received	550°C $\pm 0.30\%$ PCD (LCFA-BIS)	550°C $\pm 0.30\%$ PCD 300MPa Crept
120.4 μm	125.1 μm	124.3 μm

5.8.3 Influence of PCD on creep strength

The Type 316SS subjected to cyclic deformation exhibits cyclic hardening (see Fig.4.7), as a consequence of dislocation density increase. The hardening resulting from cyclic loading can be responsible for important changes in subsequent creep strength and creep deformation (and the occurring creep damage mechanisms).

The effect of prior 10% fatigue life fraction cyclic deformation on the creep strength of the Type 316 stainless steel at 550°C is shown in Table5.12. The effect of prior strain cycling is the same for both creep loading conditions (whereas for 1 CrMoV the effect was much more important for high creep stress).

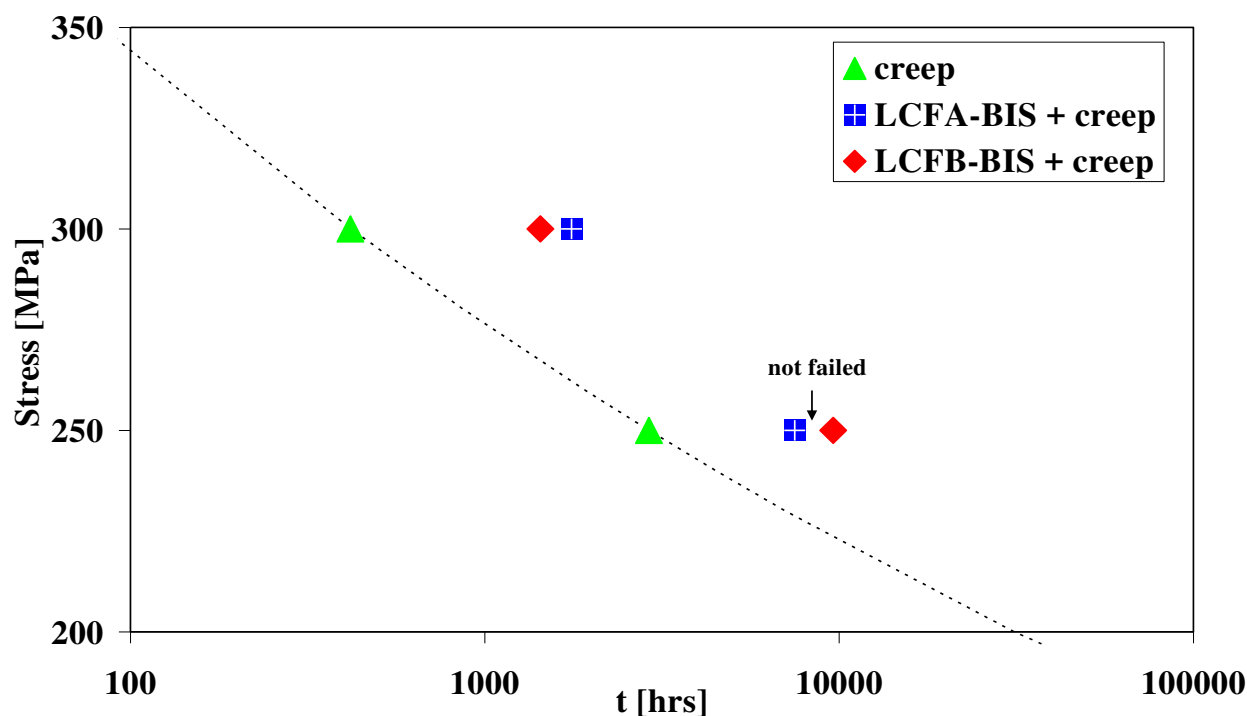


Table5.12: Influence of prior 10% fatigue life fraction on time to creep-rupture of 316SS at 550°C

The influence of the two different pre-conditioning (i.e. LCFA-BIS and LCFB-BIS, which were different for the cyclic deformation strain amplitude) treatments is the same (or LCFA-BIS tends to extend a bit more the rupture times).

The results of experimental tests on 316SS at 550°C have shown that cyclic hardening can lead to a reduction of minimum creep rates and to an increase of the times to creep-rupture. This underlines the importance of developing a damage assessment model based on a representation of creep and fatigue life fraction normalizing parameters, which is comprehensive of the fatigue and creep reciprocal influences.

5.8.3.1 The Monkman-Grant PCD independency

Fig.5.19 shows that the MG relationship for as-received 316SS is also applicable for the steel in the PCD condition. The PCD is responsible for a displacement along the $\dot{\epsilon}(t_u)$ line towards higher rupture times and lower creep rates (hence the accumulated cyclic hardening drives the 316SS towards the opposite direction with respect to that observed before for 1CrMoV, due to the effect of cyclic softening).

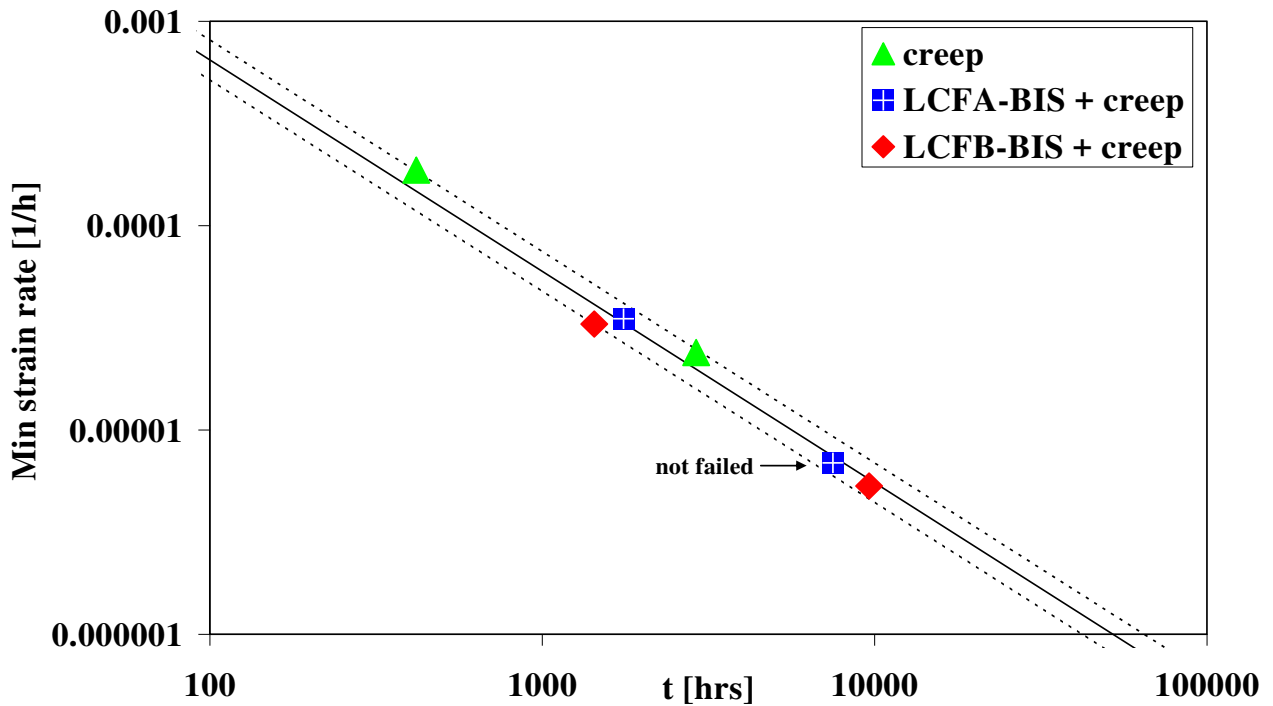


Fig.5.19: Influence of PCD on MG parameter at 550°C. Scatterbands are setted at $\pm 20\%$

In other words, the accumulated cyclic hardening leads to enhanced creep strength, given by higher rupture times and lower creep strain rates.

The magnitude of the displacement is directly related to the amount of accumulated cyclic hardening and remains constant at both 250 and 300MPa creep stress levels. The fact that the influence of the PCD on the 316SS is constant for both creep loading conditions of 250MPa and 300MPa suggests that the occurring creep damage mechanism is always the same for all the performed tests.

As for the 1CrMoV steel, this evidence was found according to results available for only one temperature value. In this case it was at 550°C.

5.8.4 Influence of PCD on creep ductility

The creep rupture ductility of the Type 316SS is also affected by prior cyclic deformation, as it can be seen in Fig.5.20.

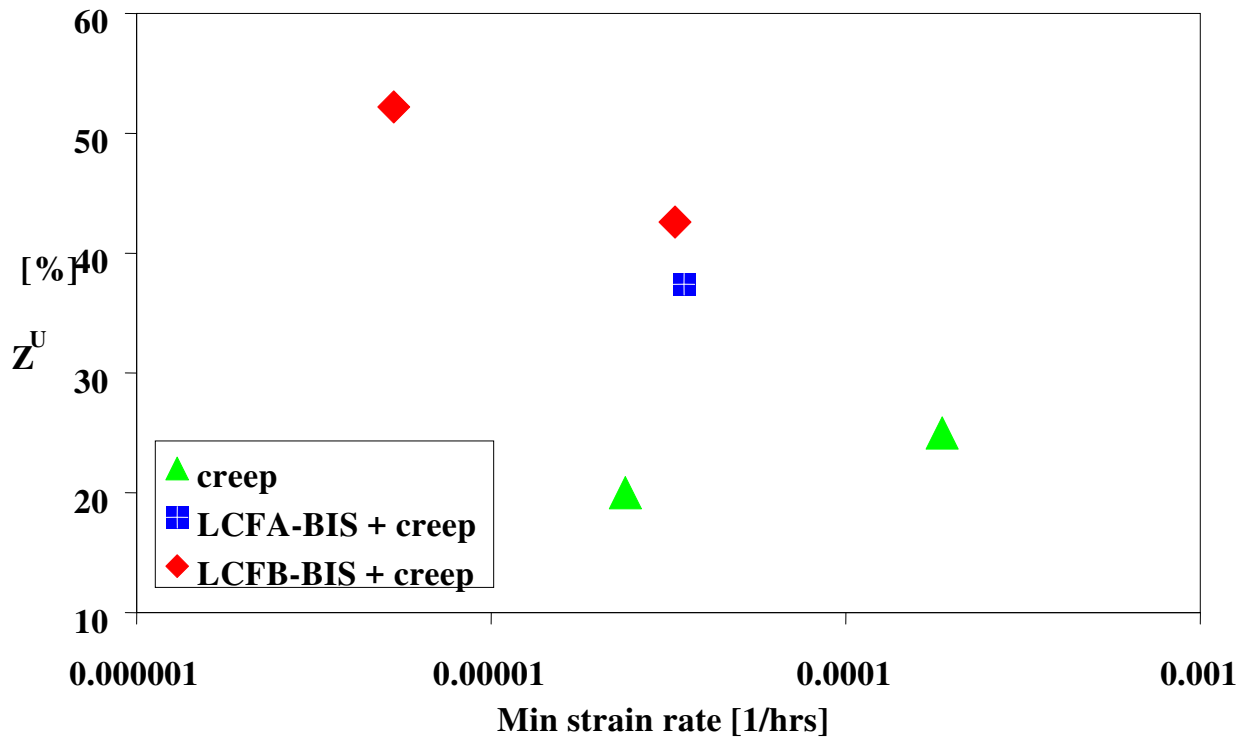


Fig.5.20: Influence of PCD on $Z_u(\dot{\epsilon}_{min})$

In particular the creep rupture ductility considerably increases in terms of area reduction (Z_u) and in terms of elongation at failure (A_u).

Such result is contradictory with that observed for the 1CrMoV steel, where cyclic softening led to higher creep rupture ductility, and more specifically addresses the importance of investigating the influence of high temperature prior cyclic deformation on subsequent creep properties (creep strength and ductility), particularly for the Type 316 stainless steel, but more generally for cyclic hardening materials, for which the prior cyclic deformation may be used as a technique aimed to enhance both creep strength and ductility.

5.8.5 Creep-fatigue damage characterisation

The prior cyclic deformation was observed to considerably affect the creep properties of Type 316 Stainless Steel: in particular the creep strength (in terms of rupture times and creep rates) and the creep rupture ductility are heavily affected by prior cyclic deformation. The accumulated cyclic hardening was the same for LCFA and LCFB pre-conditioning, hence it is at now impossible to assess the influence of different levels of accumulated cyclic hardening on creep properties.

For different creep loading conditions (250MPa and 300MPa) the effect of the PCD on the creep strength was the same, the result suggesting that the same creep damage mechanism occurred for such loading conditions.

The creep-fatigue damage assessment requires hence to be reviewed as it was done for the 1CrMoV steel.

5.9 Concluding Remarks

This chapter emphasized the difficulties in assessing the combined creep-fatigue damage in engineering components subject to static or cyclic loading conditions at high temperature. Results of creep-fatigue damage assessment from finite element analyses were compared to experimental results and observations from post test inspections and such comparison pointed out the inconsistency between results from standard finite element modelling and post test inspections, which form anyway important part of creep-damage assessment procedures.

Fundamental improvements can be achieved by considering the influence of prior cyclic deformation on creep properties and the influence of prior creep damage on fatigue crack initiation resistance, enhancing the accuracy of creep-fatigue damage assessment procedures.

The creep-fatigue damage assessment procedure based on the ductility exhaustion approach can be improved by accounting for both positive and negative creep strain accumulation.

Such new approaches offer better consistency between analytically predicted creep-fatigue damage and that observed in post test inspections.

The influence of prior cyclic deformation on subsequent creep properties were assessed for the Type 316 stainless steel also: the creep response of prior cyclic deformed Type 316 stainless steel are characterised by far higher creep strength as a consequence of accumulated cyclic hardening. Such influence can not be neglected when assessing the creep-fatigue damage assessment of Type 316 stainless steel subject to cyclic loading conditions at high temperature.

Enhancements in creep strength are accompanied by increases of creep ductility and this highlights the opportunity of performing cyclic deformation with the main objective of considerably improve such fundamental creep properties, both at the same time, in cyclic hardening materials.

6 CONCLUSIONS

The mission of this research was to develop a fundamental understanding of creep damage and deformation occurring in various engineering materials subject to steady and cyclic loading conditions at high temperature and to provide new concepts for the more effective creep-fatigue damage and deformation evaluation.

This research was hence addressed to identify the main features characterising the creep and fatigue responses of the 1CrMoV low alloy bainitic steam turbine rotor steel and the Type 316 stainless steel. Such materials were specifically chosen in order to perform the widest investigation, comprehensive of a softening response (1CrMoV) and a hardening response (Type 316 SS) to cyclic loading conditions.

The creep properties of 1CrMoV and Type 316 SS subject to static loading conditions at high temperature were also assessed. The investigated creep data sets emphasized the importance of the Monkman-Grant relationship as a time/creep strain rate tool for predicting rupture times across creep damage and deformation regimes and hence interesting for long term operating lives prediction.

The investigation highlighted also the Monkman-Grant relationship independency from temperature, as it was assessed on 1CrMoV heats in the range 450-675°C. This should be of great interest for engineers who work with this type of material over a wide temperature range.

A creep deformation predicting tool was implemented, namely the creep rupture ductility model. The model laid the foundations to further enhance the existing creep rupture ductility models, which are fundamental for creep life assessment on the basis of the ductility exhaustion approach. The implemented model represents a development of the stress-modified ductility exhaustion approach in a way which takes into account the creep properties variability given by different material microstructures. Such influence was accounted by equations representative of the effect of single material parameters obtained by fitting creep rupture data available in literature mostly produced during the 1970s and 1980s and aimed to quantify the effect of a single parameter on the creep rupture properties.

The model was hence tested on the 1CrMoV steam turbine rotor steel investigated in the EMPA High Temperature laboratory and on the NRIM – 1CrMoV creep data sheet heats and was able to considerably enhance the accuracy of creep rupture ductility predictions by reducing the variance by 54% with respect to the standard stress-modified ductility exhaustion formulation.

Standard low cycle fatigue testing was also performed on 1CrMoV and on the Type 316 SS in order to assess the response to cyclic deformation and characterize the mechanical properties. The research strategy that led to perform cyclic deformation tests on these material was aimed to assess their creep properties after prior cyclic loading (hence after prior deformation). In addition post test investigation including transmission electron microscopy was conducted in order to characterize the material microstructural evolution.

The 1CrMoV exhibited a response to cyclic deformation characterised by softening and the post test inspections revealed the dislocation density decrease and the dislocation structure rearrangement (from a uniform density-forest of dislocation condition to a non-uniform density-subgrain structure with dislocation walls condition) to be responsible for the observed cyclic softening.

The Type 316SS exhibits an opposite response to deformation, characterized by cyclic hardening due to dislocation density increasing.

The cyclic deformation tests on 1CrMoV and Type 316 SS were primarily performed in order to produce a desired pre-conditioning (characterized by cyclic softening for 1CrMoV and hardening for Type 316 SS) which would influence the material properties during following creep tests.

The prior cumulated cyclic softening (hardening) and loading conditions responsible for creep is of great interest and, in particular, the possibility to excite different damage mechanisms by introducing prior deformation as it was observed for the 1CrMoV, which exhibits different creep damage mechanisms for different loading conditions responsible for creep.

In practice fatigue standard testpieces were further machined after cyclic deformation at high temperature to standard creep testpieces in order to assess by creep testing at the same high temperature, what the influence of prior cyclic deformation on subsequent creep damage and deformation is.

After cyclic deformation the 1CrMoV steel faces the subsequent creep tests with the as described modified microstructure and exhibits creep properties characterized by lower rupture times, higher creep strain rates and higher creep rupture ductility. The magnitude of the effect depends on the amount of cyclic softening accumulated during prior cyclic deformation and the loading conditions responsible for creep. In fact, the pre-conditioned 1CrMoV differs from the as-received 1CrMoV for the softer grain structure which accumulates easily plastic deformation and hence presents weaknesses in terms of grain strength more than in terms of grain boundary strength for those creep loading conditions for which the as-received 1CrMoV steel exhibits a mixed transgranular/intergranular creep damage mechanism. This was well defined when the effect of prior cyclic deformation on subsequent creep properties of 1CrMoV was shown on a creep rupture ductility diagram as reference of creep rate. In fact the prior conditioning weakens the grain strength in a way that it ultimately leads to an increase of the transgranular creep damage mechanism proportion for those creep testing conditions which characterize the as-received 1CrMoV for a creep damage mechanism which is either partially transgranular or intergranular close to the upper limit for creep diffusion.

The influence of prior cyclic deformation on subsequent creep, as well as the considerations made about the influence of prior creep deformation on subsequent cyclic deformation, were modelled in a way to provide new normalizing parameters for the creep and fatigue damage assessment.

A detailed comparison between the time fraction approach and the ductility exhaustion approach was hence offered and represented through aid of creep-fatigue damage summation diagrams. In particular it highlighted the importance of accounting for the reciprocal influences of prior creep deformation on fatigue crack initiation resistance and the influence of prior cyclic deformation on subsequent creep strength (for the time fraction rule) and ductility (for the ductility exhaustion approach).

Furthermore, the TMF tests analysis emphasized the importance of accounting for increments of creep strain during compression stress states when calculating the creep damage fraction on a ductility exhaustion base. This approach led to better consistency between predicted damage and observed physical damage and the author assumes this to be valid for TMF loading conditions characterised by non negligible portions of lifetime spent at high temperature under compression stress states, as it was for the low temperature transient TMF test considered in this research.

The 1CrMoV creep rupture ductility model (mentioned before) was also good in predicting creep deformation properties of prior cyclic deformed 1CrMoV. The model predicted creep rupture ductility values of prior cyclic deformed 1CrMoV which were observed to be consistent with the creep

damage condition observed through post test inspections (i.e.: with the intergranular/transgranular creep damage proportion).

Furthermore, analyses of creep data for prior cyclic deformed 1CrMoV led to the evidence that the Monkman-Grant relationship representing as-received 1CrMoV still remains valid for prior cyclic deformed 1CrMoV. This sets the basis to use the Monkman-Grant relationship as a life prediction tool for materials subject to creep after prior cyclic deformation. Such results emphasized again the magnitude of such effect as a reference of the amount of accumulated cyclic softening and the loading conditions responsible for creep.

Similar results were obtained for the Type 316 stainless steel, as it was observed that the cyclic hardening accumulated during prior cyclic deformation leads to important changes in terms of creep properties. In particular the increased strength leads to higher rupture times and lower creep rates. What is even more interesting is that the creep rupture ductility of prior cyclic deformed Type 316 stainless steel considerably increased in terms of Z_u and in terms of A_u .

Such a result further underlines the importance of prior loading influence on subsequent creep properties. The possibility to perform prior cyclic deformation on Type 316 stainless steel, and more generally on cyclic hardening materials, in order to enhance both the creep strength (t_u) and rupture ductility is a fundamental result which requires further research for industrial application, aimed at developing materials of more and more advanced creep properties (strength and ductility).

The research activity performed and discussed in this dissertation offered hence the basis for the development of new concepts for the more effective creep-fatigue damage and deformation assessment. It has in fact emphasized both the importance of considering the effect of major influencing parameters (the material pedigree on the creep rupture ductility and the creep-fatigue reciprocal influences and the accumulation of creep strain during compression stress states on the creep-fatigue damage assessment) on the damage and deformation assessment of engineering materials, and the quantitative and qualitative improvement given by the presented new methods.

- [1] Abe F., Kern T.U., Viswanathan R. Creep Resistant steels, 2008. Woodhead Publishing in Materials.
- [2] ASME III Division 1 – Subsection NH, class 1 components in elevated temperature service – Rules for construction of nuclear facility components. ASME Boiler & Pressure Vessel Code, 2004.
- [3] ASTM E2368, 2004. Standard practice for strain controlled thermomechanical fatigue testing, ASTM Standards, Section 3, vol.03.01.
- [4] ASTM – E92-82 (2003). Standard test methods for Vickers hardness of metallic materials.
- [5] ASTM – E112-96. Standard test methods for determining average grain size.
- [6] Bailey J.E., Hirsch P.B.: The dislocation distribution, flow stress, and stored energy in cold-worked polycrystalline silver. *Phil. Mag.* Vol.1 (1960) 485-497.
- [7] Batte A.D. et al. The effects of residual elements and deoxidation practice on the mechanical properties and stress relief cracking susceptibility of ½%CrMoV turbine castings- *Phil. Trans. R. Soc. Lond. A* 1980;295:253-264.
- [8] Benes F. and Skvor P. Vliv medi a cinu na zarupevnost oceli CrMoV. *Hutnické listy* 1972;197-200.
- [9] Berns H. Zur Zähigkeit von Vergütungsstählen. *Zeitschrift für Werkstofftechnik* 1978;9(6):189-224.
- [10] Bhadeshia H.K.D.K., Bainite in steels, 2nd Edition, Cambridge University
- [11] Bhonghibhat S., Dehnungswechselkurven. “Technologietransfer”. Vorhaben Nr.224. Forschungsbericht, Heft 275, MPA Stuttgart, 1980.
- [12] Binda L., Holdsworth S.R. and Mazza E. Creep-fatigue damage characterisation, In: *Proc. 6th Intern. Conf. on Low Cycle Fatigue*, Berlin, 333-338, 2008.
- [13] Binda L., Holdsworth S.R., Mazza E.: Influence of prior cyclic deformation on Creep Properties of 1CrMoV, 2nd Int. ECCC Conference, Dübendorf, 467-476, 2009.
- [14] Binda L., Holdsworth S.R., Mazza E.: The exhaustion of creep ductility in 1CrMoV steel, 2nd Int. ECCC Conference, Dübendorf, 599-611, 2009.
- [15] Cane B.J. and Middleton C.J. Intergranular creep-cavity formation in low-alloy bainitic steels. *Metal Science* 1981:223-249.
- [16] Chen S.H. et al. The effects of trace impurities on the ductility of a CrMoV steel at elevated temperatures. *Metallurgical Transactions A* 1983;14A:571-580.
- [17] Colombo F., Service-like thermo-mechanical fatigue characteristics of 1CrMoV rotor steel. Diss. ETH No. 17070.
- [18] Colombo F., Masserey B., Mazza E., Holdsworth S.R., 2003. Simple modelling of the constitutive behaviour of a 1%CrMoV rotor steel in service-like thermo-mechanical fatigue tests. *Mater. High Temp.* 19 (4) 225-234.
- [19] Douglas J., Spindler M., Dennis R., Development of an advanced creep model for type 316 stainless steel. 8th Int. Conf. on creep and fatigue at elevated temperatures, San Antonio, 2007.
- [20] Edmunds H.G., White D.J., Observations of the effect of creep relaxation on high-strain fatigue. *Journal Mechanical Engineering Science*, Vol.8 No3, 1966. 310-321.
- [21] EN – 10291:2000. Metallic materials – Uniaxial creep testing in tension – Methods of test.
- [22] Fattorini F. Effect of impurity content on creep crack growth resistance in 1CrMo¼V ferritic steels. *Metallurgical Transactions A* 1990;21A:1941-1949.
- [23] Frost H.J., Ashby M.F., Deformation-mechanism maps: the plasticity and creep of metals and ceramics, Pergamon press. 1982.
- [24] George E.P. et al. Creep cavitation in iron-II. Oxides as nucleation sites. *Acta Metall.* 1987;35(10):2487-2495.

- [25] George E.P. et al., Creep ductility of CrMoV steels: Impurity and microstructural effects. *Scripta Metallurgica* 1987;20(12):1775-1779.
- [26] George E.P. et al., Creep cavitation in Iron-I. Sulfides and carbides as nucleation sites. *Acta Metall.* 1987;35(10):2471-2486.
- [27] Hall E.O., The deformation and ageing of mild steel: III discussion of results. *Proc. Phys. Soc.* 1951. 64. 747-753.
- [28] Holdsworth S.R. The ECCC approach to creep data assessment. *ASME J. Pressure Vessel Technology* 2008;130(May):024001-1-6.
- [29] Holdsworth S.R. Advances in the assessment of creep data during the past 100 years. In: *Proc 5th Intern. Conf. on Creep, Fatigue and Creep-Fatigue Interaction*, IGCAR, Kalpakkam, 2008.
- [30] Holdsworth S.R. Prediction of creep-fatigue behaviour at stress concentrations in 1CrMoV rotor steel. In: *Proc. Conf. on Life Assessment and Life Extension of Engineering Plant, Structures and Components*, Churchill College, Cambridge, September, 1996.
- [31] Holdsworth S.R. Developments in the assessment of creep strain and ductility data. *Materials at High Temperatures* 2004;21(1):125-132.
- [32] Holdsworth S.R., Mazza E., Jung A.: The response of 1CrMoV rotor steel to service-cycle thermo-mechanical fatigue testing. *ASTM J.Test Eval.*, 2004, 255-261.
- [33] Holdsworth S.R., Mazza E., Binda L. and Ripamonti L. Development of thermal fatigue damage in 1CrMoV rotor steel. *Nuclear Engineering & Design* 2007;237(4):2292-2301.
- [34] Holdsworth, S.R. and Mazza, E. Exploring the applicability of the LICON methodology for a 1%CrMoV steel, *Materials at High Temperatures* 2008;25(4):267-276.
- [35] Hollomon J.H. and Jaffe L.D. Time-temperature relations in tempering steels. *Metals Technology* 1945:223-249.
- [36] ISO 12106:2003 (E) Metallic materials – Fatigue testing – Axial strain controlled method
- [37] Kadoya Y. et al. Effects of Cr, Mo, W, Mn and Ni on creep properties of 2¼CrMoV steel. *J. Iron & Steel Inst. Of Japan (Japanese Edition)* 1993;79(8):92-99.
- [38] Lemaitre J., Chaboche J.L.. *Mechanics of Solid Materials*. Cambridge University Press.
- [39] Manson S.S., Brown W.F.. Time-temperature-stress relaxations for the correlation and extrapolation of stress-rupture data. *Proc.ASTM*, 1953;53:693-791.
- [40] Mazza E., Hollenstein M., Holdsworth S.R., Skelton R.P., 2004. Notched specimen thermo-mechanical fatigue of a 1CrMoV rotor steel. *Nucl.Eng.Des.* 234, 11-24.
- [41] Myers M.R. et al., Cavity nucleation and growth in a 1%Cr0.5%Mo steel. *Materials Science & Engineering* 1987;95:81-91.
- [42] Middleton C.J. Reheat cavity nucleation and nucleation control in bainitic creep-resisting low-alloy steels: Roles of manganese, sulphide, residual, and sulphur-stabilizing elements. *Metal Science* 1981;April:154-167.
- [43] Needham N.G. and Orr J. The effect of residuals on the elevated temperature properties of some creep resistant steels. *Phil. Trans R. Soc. Lond. A* 1980;295:279-288.
- [44] Norton J.F. and Strang A. Improvement of Creep and Rupture. Properties of Large 1%Cr-Mo-V Steam Turbine Rotor Forgings. *JISI* 1969;207:193.203.
- [45] *NRIM Creep Data Sheet No. 9B*. National Research Institute for Metals. Tokyo, Japan, 1990.
- [46] Orr R.L., Sherby O.D., Dorn J.E.. Correlations of rupture data for metals at elevated temperatures. *Trans. ASM* 1954;46:113-128.
- [47] Petch N.J., The cleavage strength of polycrystals. *Journal of the Iron and Steel Institute*. May 1953. 25-28.
- [48] Plumbridge W.J. & Ryder D.A.: The metallography of fatigue. *Metallurgical reviews* 136 (1969) 119-142
- [49] Plumbridge W.J. & Miller K.J., Influence of prior fatigue deformation on creep behaviour. *Proc. Conf. on Creep Strength in Steel and High Temperature Alloys*, Iron & Steel Institute, 1972. pp.50-53.

- [50] Priest R.H. & Ellison E.G.: A combined deformation map-ductility exhaustion approach to creep fatigue analysis. *Materials Science & Engineering* 49 (1981) 7-17.
- [51] R5. Assessment Procedure for the High Temperature Response of Structures. Procedure R5 Issue 3, British Energy, Gloucester, UK, 2003.
- [52] Ramberg, W., & Osgood, W. R. (1943). Description of stress-strain curves by three parameters. *Technical Note No. 902*, National Advisory Committee For Aeronautics, Washington DC.
- [53] Ratliff J.L. and Brown R.M. The deleterious effect of small quantities of Al on the stress-rupture properties of a CrMoV steel *Trans. Am. Soc. Metals* 1967;60:176-186.
- [54] RCC-MR, Design and construction rules for mechanical components of FBR nuclear islands. AFCEN, Paris, 1985.
- [55] Roan D.F. and Seth B.B. A metallographic and fractographic study of the creep cavitation and fracture behaviour of 1Cr1Mo¹/₄V rotor steels with controlled residual impurities, Ductility and Toughness considerations in elevated temperature service, 79-97, ASME, New York, 1979.
- [56] Seah M.P. Impurities, segregation and creep embrittlement. *Philos. Trans. R. Soc. London*, 1980;295A:265-279.
- [57] Shinya N., Kyono J., Kushima H. & Yokoi S.: Effect of creep damage on fatigue life of Cr-Mo-V steel. *Trans. National Research Institute for Metals* 29(2) (1987) 115-123.
- [58] Skelton R.P., Creep-Fatigue damage accumulation and interaction diagram based on metallographic interpretation of mechanisms, EPRI Review, 2007.
- [59] Spindler M.W. The multiaxial and uniaxial creep ductility of type 304 steel as a function of stress and strain rate. *Materials at High Temperatures* 2004;21(1):47-52.
- [60] Stone P.G. and Murray J.D. Creep ductility of CrMoV steels. *J. Iron Steel Inst.* 1965;203:1094-1107.
- [61] Thompson, N.; Wadsworth, N.; Louat, N. The origin of fatigue fracture in copper. *Phil. Mag.* [8] (1956), 1, 113-26.
- [62] Trunin I.I., Golobova N.G., Loginov E.A.. New methods of the extrapolation of creep test and long time strength results. *Proc. 4th Int. Symp. on Heat-Resistant Metallic Materials*, Mala Fatra, CSSR 1971 168-176.
- [63] Viswanathan R. Effects of residual elements on creep properties of ferritic steels. *Metals Engineering Quarterly* 1975;November:50-56.
- [64] Viswanathan R. Effect of Ti and Ti+B additions on the creep properties of 1.25Cr0.5Mo steels. *Metallurgical Transactions A* 1977;8A:57-61.
- [65] Viswanathan R. and Beck C.G. Effect of Al on the stress rupture properties of CrMoV steels. *Metall.Trans. A* 1975;6:1997-2003.
- [66] Wilkinson D.S. et al. Compositional effects on the creep ductility of a low alloy steel. *Metallurgical Transactions A* 1980;11A:1827-1836.

8 ACKNOWLEDGEMENTS

Now at the end of my PhD I wish to express my gratitude to Prof. Edoardo Mazza and Dr. Stuart Holdsworth for the opportunity they offered me for engaging such a professional and educational experience, and to Prof. Kamran Nikbin, who co-reviewed and recommended this dissertation.

Special thanks go to Mr. Mike Spindler for sharing important research outcomes and materials for new research.

I thank all my students, who delivered outstanding results at EMPA in Dübendorf, making me really proud of them. I wish you great success and satisfaction.

I thank all the people who shared with me part of their life during the past few years, and in particular the abteilung 119 at EMPA (Mechanics for Modelling and Simulation) and the High Temperature Integrity group. I am specially in debt with Freddy Bürki, who helped me so much in sorting out the High Temperature Integrity testing laboratory and in preparing and running so many critical experiments.

I also thank the TEM group at ETH-Hönggerberg and the D-MAVT at the ETH Zentrum in Zürich.

Last, I express my appreciation to the ETH facilities (Fluntern Sportanlage) because it has been my only chance to survive during the coldest swiss times and to come back home.

Luca

I. APPENDIX : 1CrMoV ROTOR STEEL

The 1CrMoV low alloy bainitic steel is widely used in the power generation industry for the manufacture of high temperature turbine components, in particular rotors operating up to 565°C at the inlet stages of high and intermediate pressure (HP/IP) steam turbines.

The bainitic microstructure is obtained after austenitising at temperatures from 950°C to 1000°C for 1 to 24 hours by oil quenching. Tempering is performed at temperatures between 650°C and 720°C for up to 48 hours in order to precipitate V_4C_3 .

This hardening treatment produces a fine dispersion of V_4C_3 particles into the ferrite and other carbide particles like $Cr_{23}C_6$, Cr_7C_3 , Mo_2C , Mo_6C and most of all cementite Fe_3C . These latter particles are coarser than the V_4C_3 and form depending on the amount of C available into solution: if vanadium and carbon are stoichiometrically balanced, the maximum concentration of V_4C_3 can be obtained and the Fe_3C completely eliminated [60]. If the stoichiometric balance is not respected Fe_3C tend to form at prior austenite grain boundaries reducing the local concentration of V_4C_3 (hence the so-called denuded areas at grain boundaries) and ultimately affecting the creep properties.

The heat treatment and the chemical composition control the distribution of V_4C_3 particles but also their size: with higher hardening temperatures such V_4C_3 particles become finer and leave a larger concentration of vanadium into solution (being its solubility enhanced for higher interfaces curvatures). According to hypothesis advanced by Bhadeshia [10], if the dissolved vanadium interacts with dislocations to control creep deformation then it is legitimate to think that a finer, uniform and intense V_4C_3 distribution is responsible for higher creep strength.

Fig.I.1 shows the microstructure appearance of the as-received 1CrMoV steel as observed at the optical microscope.

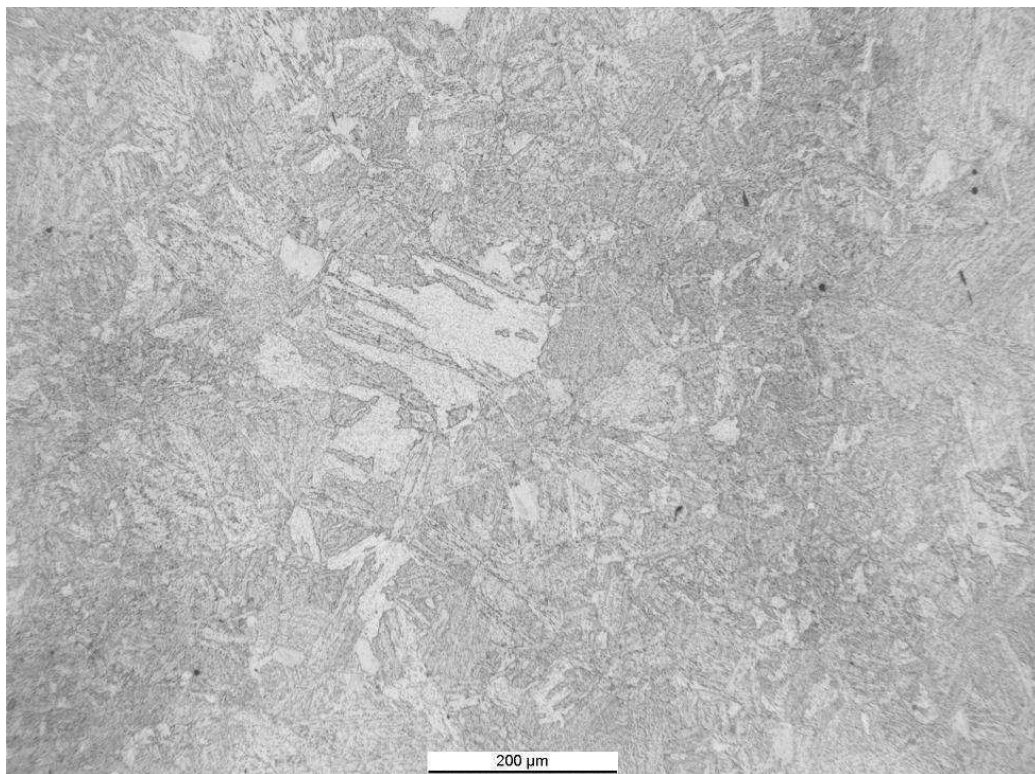


Fig.I.1: Bainite lath microstructure within prior austenite grains observed at the optical microscope

A first analyses of the 1CrMoV through the transmission electron microscope at low magnification (X1500) or even at an optical microscope allows to observe the microstructure in the form of bainite, a product obtained by diffusion and precipitation of carbon from supersaturated ferrite to retained austenite leading to an aggregate of small laths of ferrite divided by cementite. Depending on the cooling rate and the temperature during transformation, upper or lower bainite may form. Upper bainite (higher temperature) has bainitic ferrite laths free of carbide precipitates whereas lower bainite (lower temperature) is characterised by precipitation of carbides also within the bainitic ferrite laths due to the slower carbon diffusion from supersaturated ferrite to retained austenite and precipitation of carbon within the bainitic ferrite laths.

Fig.I.2 shows the microstructure of 1CrMoV observed with a transmission electron microscope.

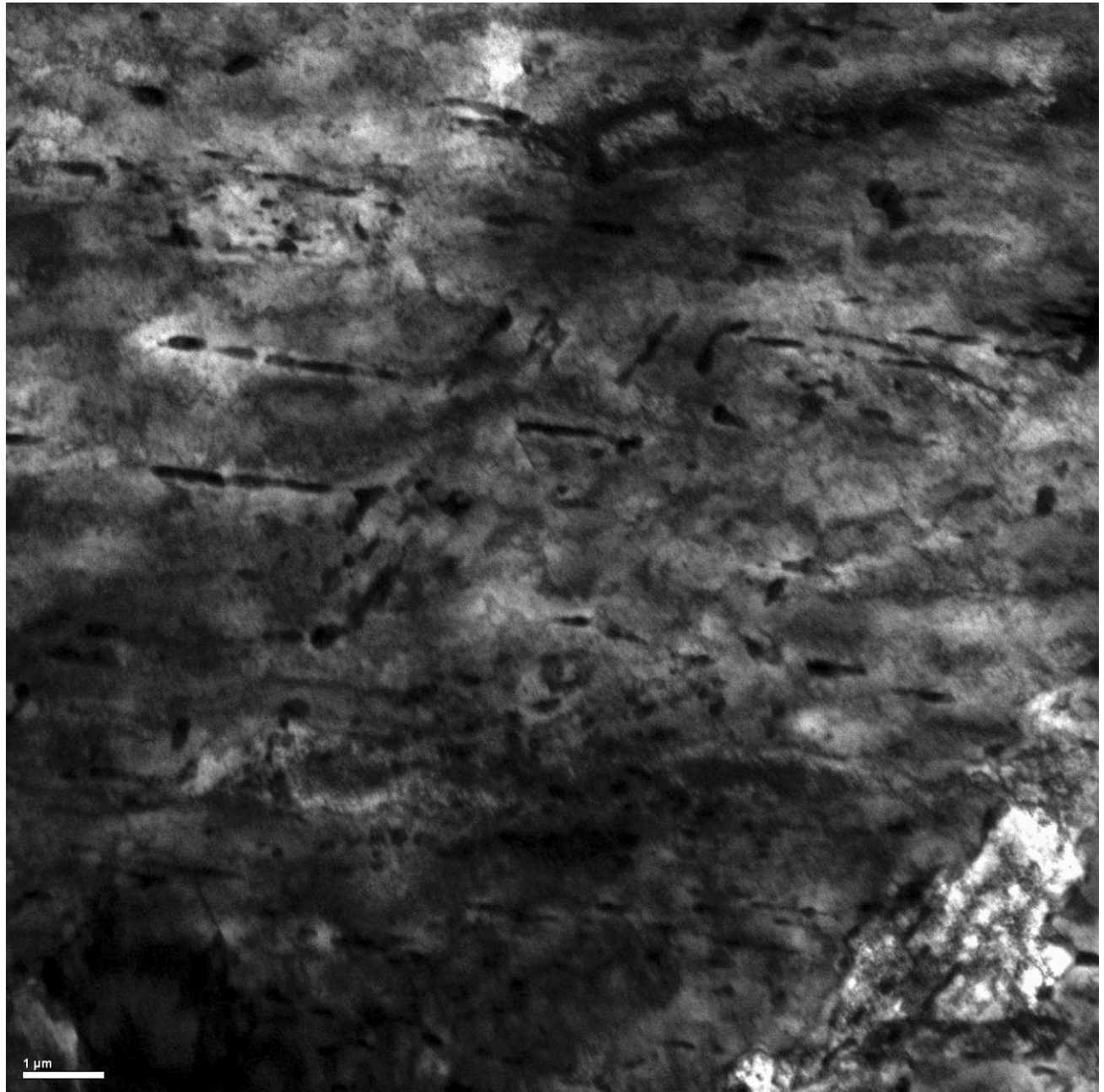


Fig.I.2: Bainitic ferrite laths within retained austenite grains observed at transmission electron microscope -100-

A more focused observation of the bainitic ferrite laths through the electron microscope reveals the intense presence of vanadium carbides (V_4C_3 , with size of 20nm), which are responsible for controlling the plastic flow by dislocations motion. Chromium carbides (size in the order of 100nm) form usually at prior austenite grain boundaries, but also within the bainitic ferrite laths, as shown in Fig.I.3.

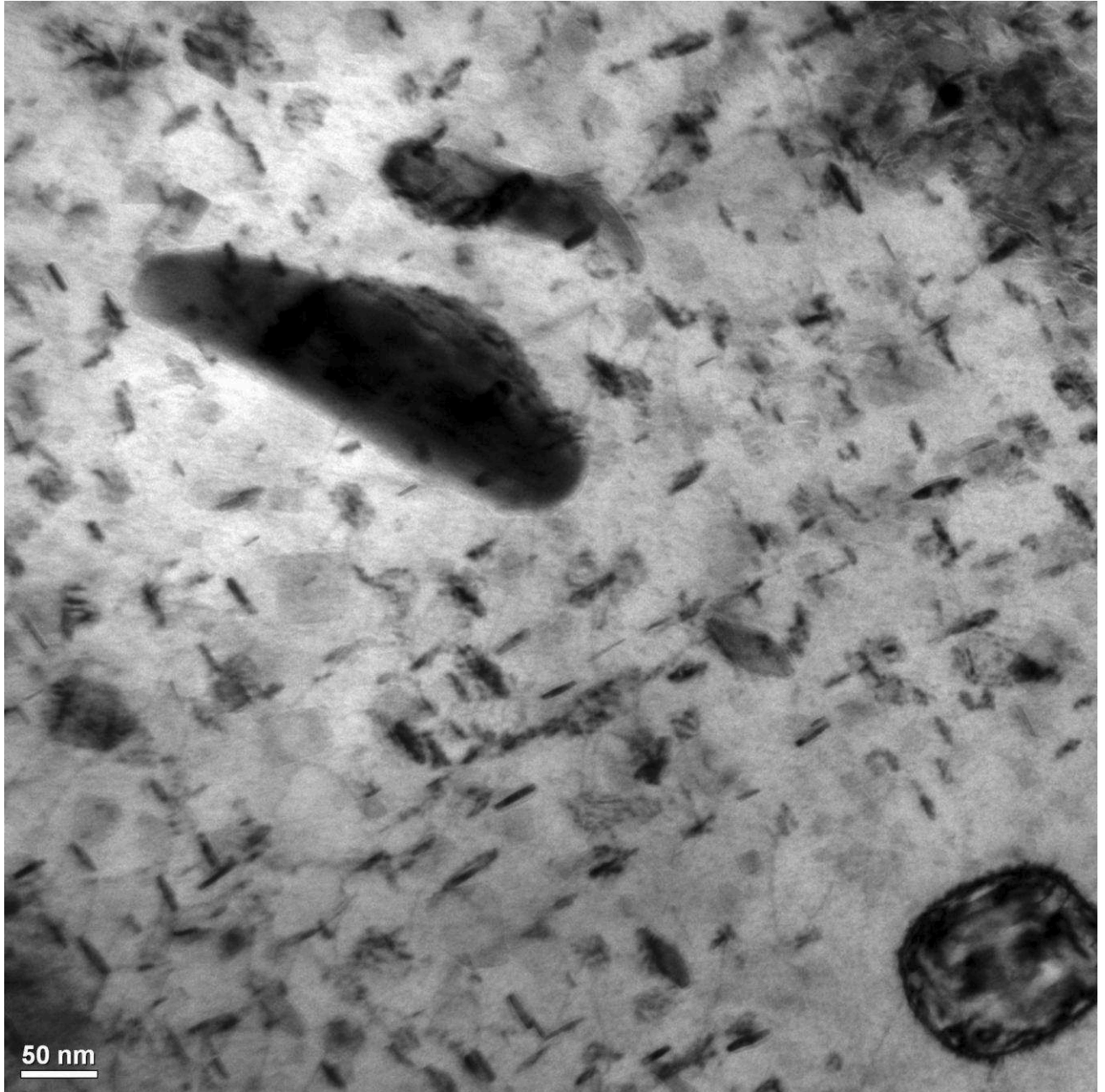


Fig.I.3: V_4C_3 and Cr_7C_3 within the bainite lath of 1CrMoV -100-

a. Material pedigree

The 1CrMoV steel analysed in the present research originated from a high temperature HP steam turbine rotor forging. Much information about this steel can be found in [17]. The chemical composition of the production forging investigated in the present study are summarised in TableI.1.

TableI.1: 1CrMoV Chemical composition, in weight percentage

C	Si	Mn	S	P	Cr	Mo	Ni	V	Fe	Al	Cu	Sn	As	Sb
0.25	0.10	0.68	0.006	0.005	0.88	0.76	0.69	0.33	bal	0.001	0.08	0.006	0.005	0.003

The steel was heat treated as reported in TableI.2. Testpieces were taken from locations close to the periphery of the forging with a longitudinal orientation with respect to the axis.

Hardening	Tempering
970°C, OQ	695°C, AC
TableI.2: 1CrMoV heat treatment	

i. Hardness

Hardness of as-received material was measured through Vickers hardness tests according to standard practice [4]: the hardness observed was 245HV/16.

ii. Grain size

The prior austenite grain size of as-received 1CrMoV was measured according to standard practice [5]. The average grain size obtained was 34.5µm. TableI.3 shows the results of grain size measurements.

field	magnification	n°grains	grain size [µm]
1	X166	144	35.0
2	X335	72	33.6
3	X335	69	34.6
AVG		285	34.5
TableI.3: 1CrMoV Grain size measurements			

b. Mechanical properties

i. Tensile properties

The tensile properties of the 1CrMoV steel investigated in the present research are shown in TableI.4. The tensile tests were performed at a controlled strain rate of 0.4%/min. The results shown in TableI.4 emphasize the change of mechanical response with increasing temperature. In particular the plastic hardening effect (important at room temperature) tends to disappear at higher temperatures, transforming the stress-strain monotonic curves to perfect elastic-perfect plastic responses.

T	E [MPa]	R _{p0.2} [MPa]	R _m [MPa]	Z _u [%]	A _u [%]
22	218.9	639.3	779	59.3	18.5
150	200.1	596.8	714	54.6	15.5
350	197.6	552.5	678	56.2	15.5
525	162.6	465.6	501	76.4	16.5
550	160.8	444.6	487	43.5	18.5
575	159.4	421.1	460	82.5	21.5

TableI.4: 1CrMoV Tensile properties

ii. LCF properties

TableI.4 shows the low cycle fatigue properties of the 1CrMoV steel. The experimental results obtained by [17] at 550°C are compared to those of [11] at temperatures from 500 to 600°C. The 1CrMoV object of this research exhibits higher fatigue endurance at low strain amplitudes, but performs progressively worst at larger cyclic strain amplitudes.

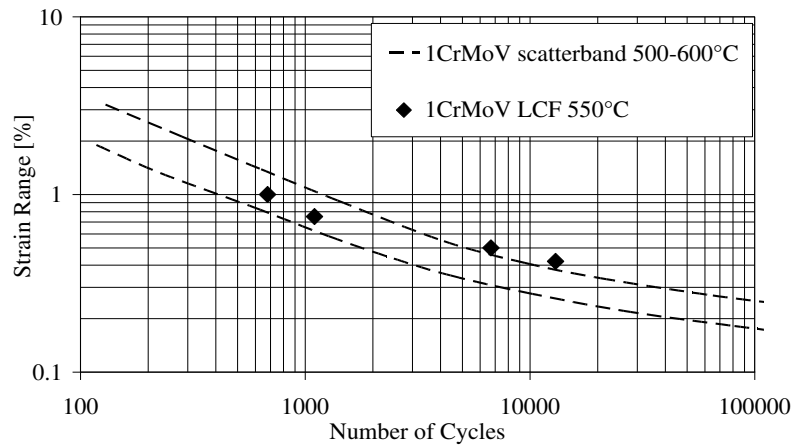


Fig.I.4: 1CrMoV LCF properties at 550°C [17] and between 500 and 600°C [11].

iii. Creep properties

The 1CrMoV steel creep data sheet provided by NIRM [45] is widely used throughout the present research for different purposes. It offers creep data of 9 heats, over a temperature range from 450°C to 675°C and loading conditions leading to rupture times from 4 days to 20 years. Fig.I.5 shows the NIRM creep data collected at 550°C and compares them to the creep data obtained by [34] with the 1CrMoV (object of the present research) at 550°C.

The plot exhibits the higher creep strength of the EMPA tested 1CrMoV for medium-low rupture times, which vanishes to the upper creep strength band of the NIRM data sheet for medium-high rupture times.

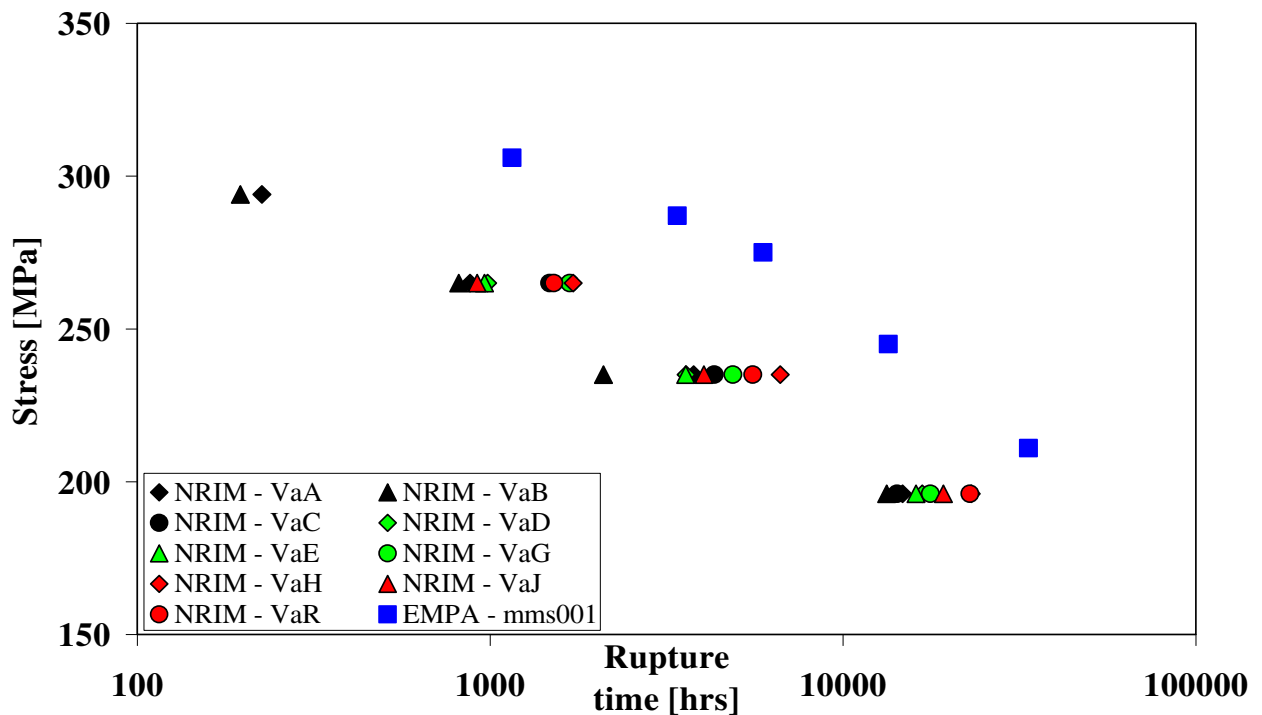


Fig.I.5: 1CrMoV Creep properties at 550°C according to [45] and [34].

II. APPENDIX : TYPE 316 STAINLESS STEEL

a. Material pedigree

The chemical composition of the Type 316 stainless steel is summarised in TableII.1.

TableII.1: Type 316 SS, chemical composition in weight percentage

C	Si	Mn	S	P	Cr	Mo	Ni
.07	.42	1	.016	.021	17.1	2.3	11.4

Co	B	V	Fe	Al	Cu	Sn	W
.09	.002	.036	Rem.	.005	.15	.012	.06

The steel was heat treated according to the procedure reported in TableII.2.

TableII.2: Type 316 SS, heat treatment

Solution treatment [°C]	Quenching
1050	water

i. Hardness

Hardness of as-received material was measured through Vickers hardness tests according to standard practice [4]: the hardness observed was 143.7 HV / 16.

ii. Grain size

The prior austenite grain size of as-received 316SS was measured according to standard practice [5]. The average grain size was 120.4 μ m.

TableII.3 shows the results of grain size measurements.

TableII.3: Type 316 SS, grain size measurements

Field	Magnification	number of grains	grain size
1	X63	66	119.4
2	X63	62	127
3	X63	67	117.6
4	X63	70	112.6
5	X63	63	125
6	X63	66	119.4
7	X63	68	115.9
8	X63	69	114.2
9	X63	59	133.6
10	X63	66	119.4
		avg grain size	120.4
		std dev	6.4
		RA	4.37%

b. Mechanical properties

i. Tensile properties

The tensile properties of the Type 316 SS at 538°C were provided by [19] and are shown in TableII.4.

TableII.4: Type 316 SS, tensile properties [19]

T [°C]	R _{p0.2} [MPa]	R _m [MPa]
538	201	434

ii. Fatigue properties

Fig.II.1 shows that the Type 316 SS subject to cyclic deformation exhibits cyclic hardening up to a peak hardening (after about 10% to 20% of the fatigue endurance) followed by slow cyclic softening.

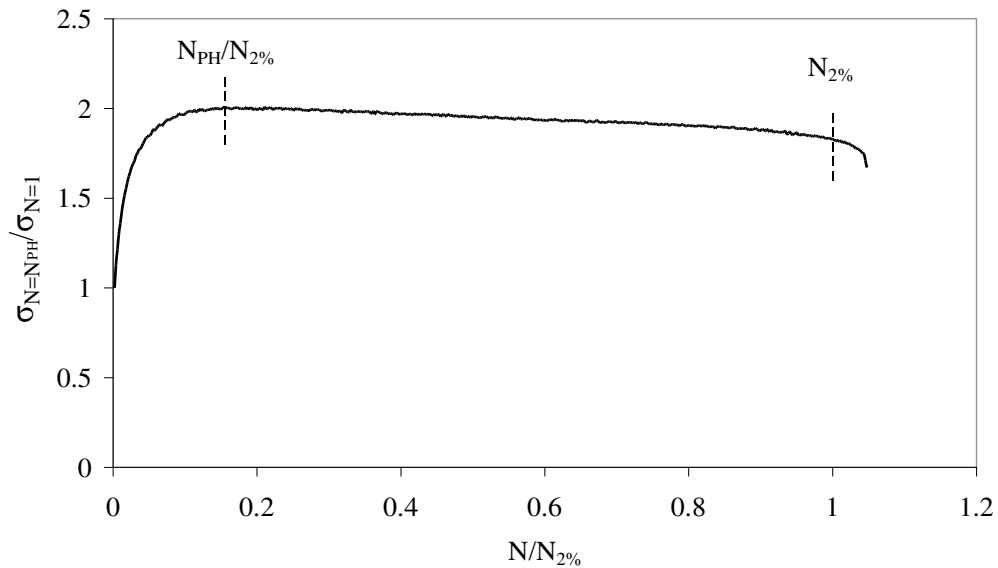


Fig.II.1: Type 316 SS, stress-cycle response at 550°C with $\pm 0.8\%$ strain range.

Fig.II.2 shows the endurance of the Type 316 SS and the number of cycles to the peak hardening for strain ranges from $\pm 0.3\%$ to $\pm 0.8\%$.

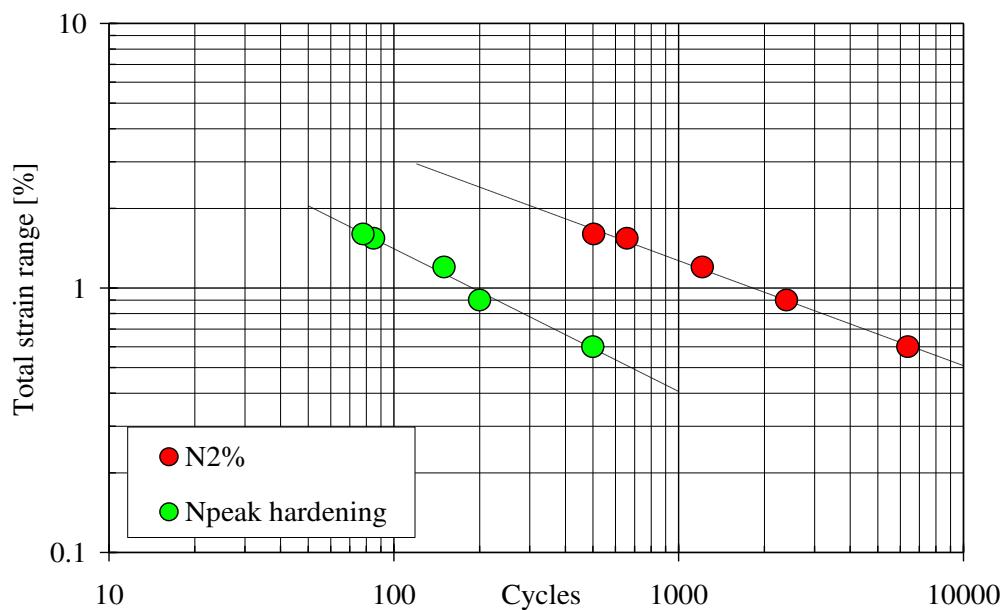


Fig.II.2: Type 316 SS, fatigue properties at 550°C [19]

iii. Creep properties

Fig.II.3 shows the assessed creep strength data of the Type 316 SS originated from Douglas [19].

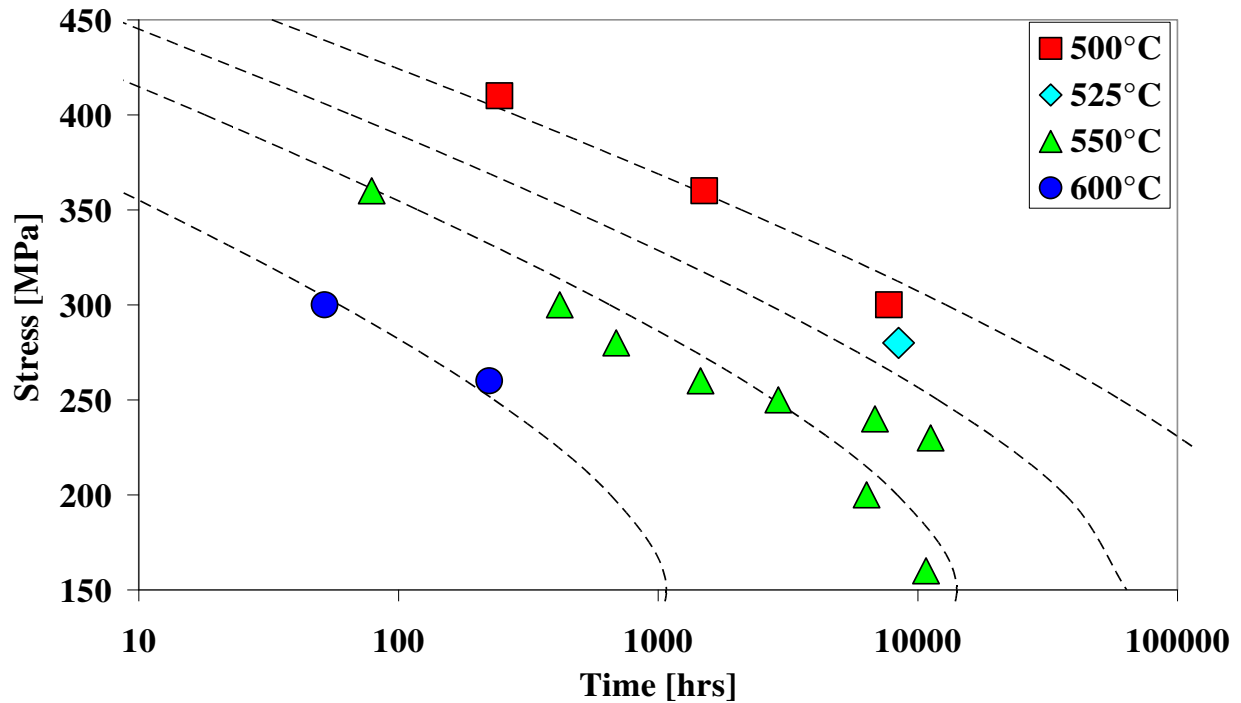


Fig.II.3: Type 316 SS, creep strength [19]

Creep data were interpolated with the Soviet Model II [62], which was found to be the best representative model for such database, with the equation

$$\log(t_u) = \beta_0 + \beta_1 \cdot \log(T) + \beta_2 \cdot \frac{\log(\sigma)}{T} + \frac{\beta_3}{T} + \beta_4 \cdot \frac{\sigma}{T}$$

with the coefficients reported in TableII.5

β_0	β_1	β_2	β_3	β_4
-249.608	69.6582	7252.308	29211.8	-21.892
TableII.5: Type 316 SS, coefficients representative of Soviet Model II [62]				

BINDA LUCA

Mobile phone: +39.380.2566838

Birth: Monza – MB – Italy, 14th November 1980

Address: Via Mascagni 9, 20035 Lissone - MB - Italy

EDUCATION

2009-2010 MBA, Master of Business Administration at SDA Bocconi, Milan, Italy.

2006-2009 PhD, Industrial Engineering at ETH, Zürich, Switzerland.

1999-2004 MSc, Mechanical Engineering at Politecnico di Milano, Milan, Italy.

1994-2004 Diploma di Maturità Scientifica at Istituto Salesiani, Sesto S.G., Milan, Italy.

PROFESSIONAL EXPERIENCES

2006-2009 EMPA Dübendorf , Switzerland.

Research assistant.

2005-2006 WEIR GROUP p.l.c., Sesto S.G., Italy.

Products Development Manager and Service Manager. Rotating machinery department.

2004-2005 FIAT AUTO s.p.a., Arese, Italy.

Product Development Engineer. Engine department.